12-2021

Microwave Spectroscopy of Cyclohexanecarboxylic Acid, Chlorosulfonic Acid, and Its Interaction with Water

Diego Erik Rodriguez
The University of Texas Rio Grande Valley

MICROWAVE SPECTROSCOPY OF CYCLOHEXANECARBOXYLIC ACID,

CHLOROSULFONIC ACID, AND ITS INTERACTION WITH WATER

A Thesis

by

DIEGO ERIK RODRIGUEZ

Submitted in Partial Fulfillment of the

Requirements for the Degree of

MASTER OF SCIENCE

Major Subject: Chemistry

The University of Texas Rio Grande Valley

December 2021

MICROWAVE SPECTROSCOPY OF CYCLOHEXANECARBOXYLIC ACID,

CHLOROSULFONIC ACID, AND ITS INTERACTION WITH WATER

A Thesis
by
DIEGO ERIK RODRIGUEZ

COMMITTEE MEMBERS

Dr. Wei Lin
Chair of Committee

Dr. Shervin Fatehi
Committee Member

Dr. Evangelia Kotsikorou
Committee Member

Dr. Erik Plata
Committee Member

Dr. Javier Macossay
Committee Member

December 2021

ABSTRACT

Rodriguez, Diego E., <u>Microwave Spectroscopy of Cyclohexanecarboxylic Acid, Chlorosulfonic Acid, and its Interaction with Water</u>. Master of Science (MS), December 2021, 128 pages, 16 tables, 69 figures, references, 77 titles.

This study combines computational chemistry and microwave spectroscopy to simulate the behavior of two molecules: cyclohexanecarboxylic acid and chlorosulfonic acid. In this thesis, the conformational analysis of the cyclohexanecarboxylic acid monomer will be presented. For chlorosulfonic acid, its interaction with one, two, and three water molecules will be discussed as well. "*Chapter I: Introduction*" provides insight into the motivation of the study and the published literature related to cyclohexanecarboxylic acid, chlorosulfonic acid, and perfluoroalkyl substances. "*Chapter II: Computational Chemistry*" introduces computational chemistry methods used in this study. "*Chapter III: Microwave Spectroscopy*" explains the function of the instrumentation used to measure the molecules undergoing rotational transitions. Additionally, this chapter explains the relationship between computational chemistry and the experimental measurements of microwave spectroscopy. "*Chapter IV: Results of Cyclohexanecarboxylic Acid*" and "*Chapter V: Results of Chlorosulfonic Acid and its Hydrates*" both report results for the respective molecules.

DEDICATION

This work is dedicated to all those who supported me during my time as a graduate student. Also, to any students who may be reading during a stressful time: you got this. Keep your head up and you will get through anything. To my future self: what you did here is a big accomplishment. Don't take it for granted.

ACKNOWLEDGMENTS

TABLE OF CONTENTS

LIST OF TABLES

LIST OF FIGURES

Page

CHAPTER I

INTRODUCTION

Section 1.1 – Perfluoroalkyl Substances

Perfluorooctanoic acid (PFOA) and perfluorooctanesulfonic acid (PFOS) are

perfluorinated compounds that have been found in environments worldwide, in both the Eastern

and Western hemispheres[1,2]. The primary characteristic that makes these two compounds

difficult to remove from the environment is the affinity for water that these compounds exhibit

due to their polar end groups. In particular, the sulfonic acid group in PFOS and the carboxylic

acid group in PFOA are implicated in the respective molecules' high affinity for water. These

groups can form hydrogen bonds with several water molecules at a time making it difficult to

remove PFOA and PFOS from the environment. Additionally, the stability of these

perfluorinated groups is increased when they are hydrogen bonded to water. For this reason,

there is an increasing concern over this molecule; the molecule does not decompose and can

bioaccumulate in living organisms and the environment[3]. Bioaccumulation of poly- and

perfluoroalkyl substances (PFAS) has been linked to adverse health effects including

immunotoxicity in mice[4]. These health effects may or may not extend to humans, but studies for

the detection of these perfluorinated groups, such as PFOS and PFOA, have already been

conducted worldwide in countries including the United States, South Korea, Japan, Italy,

Germany, China, Brazil, and Australia[5].

Production of perfluorinated organic molecules began in the 1940s. The 3M company started commercial development of fluorochemistry by licensing a technique known as Simons Electro-Chemical Fluorination (ECF), which replaces the hydrogen atoms of organic compounds with fluorines[6]. With this process, PFAS could be easily produced, and they were produced for many years in the United States. It was not until the 2000s that the production of PFOS and PFOA began its decline in the United States, motivated by studies that found high levels of PFOA and PFOS in the blood of 3M and DuPont workers[7]. Despite increasing awareness of the potential danger associated with PFAS, these compounds continue to be synthesized in some parts of the world. In light of this continued production, there are still ongoing efforts by organizations worldwide to keep track of PFAS and other Persistent Organic Pollutants (POPs) defined under the Stockholm Convention. It is important to note that PFOS and PFOA are both listed as "POPs" meaning that the participating countries are to cease production of said compounds[8]. Even with the decline in production of PFAS, there remains the problem of removing these harmful contaminants from the environment which have bioaccumulated within living organisms on land and in the sea.

To advance the process of removing these contaminants from the environment, we have taken the approach of studying precursor molecules of PFAS. This is part of a systematic study to observe molecules bearing similar characteristics to PFOS and PFOA. To do this, we begin looking at the superacid, chlorosulfonic acid, which has the sulfonic acid group exactly like PFOS. Chlorosulfonic acid is a very strong oxidizing agent that can be used for the synthesis of PFAS through the reaction of a perfluoroalkyl iodide and chlorosulfonic acid yielding perfluoroalkanoic acids[9,10].

Section 1.2 – Health Complications Linked to PFAS

The stability of PFOS is one of the main reasons that the molecule has bioaccumulated over the years. The hydrophilic end of the molecule forms hydrogen bonds with water, while its fluorinated carbons are very stable, making the natural degradation of PFOS extremely slow. Combined with the increased production of PFAS over the latter half of the 20th century, it is no surprise that the molecules ended up in the environment. There is justified concern over the effects PFAS can potentially have on an organism's health, because studies have identified alarming concentrations of PFAS in water sources, agricultural plants, animals, and humans[11,12,13].

In 2019, an article was published in which the health risks of perfluorooctantesulfonic acid (PFOS) were studied through *in vivo* and *in vitro* systems. The data showed that exposure to PFOS can cause hepatoxicity, neurotoxicity, reproductive toxicity, immunotoxicity, thyroid disruption, cardiovascular toxicity, pulmonary toxicity, and renal toxicity in laboratory animals and *in vitro* human systems[14]. This is enough data to at least acknowledge that PFAS can be a potential danger to the health of the environment.

Section 1.3 – Sulfonic Acids Literature Review

There have been no previous studies on the rotational spectroscopy of chlorosulfonic acid, which is a derivative of PFOS. However, we will briefly discuss a study of the ionic dissociation of halosulfonic acids, as this thesis covers chlorosulfonic acid complexed with up to 3 water molecules. In the theoretical study by Shujin Li, Fu-Ming Tao, and Renao Gu, the monohydrates of the halosulfonic molecules were observed to form hydrogen bonds of about 1.65 Å, whereas water dimer hydrogen bonds are 1.96 Å as shown in Figure 1. Additionally, one of the hydrogen atoms in the water molecule seem to form a very weak hydrogen bond with one

of the oxygens of the sulfonic acid group, at a distance of 2.4 - 2.5 Å. These findings will be compared later with our own calculations.

As for trihydrates, it was observed in this theoretical study that the sulfonic acid group (HSO_3-X) would dissociate through protonation of H_2O when in a complex of at least 3 water molecules[15]. The positioning of the water molecules is an important determinant of whether the sulfonic acid group will be deprotonated.
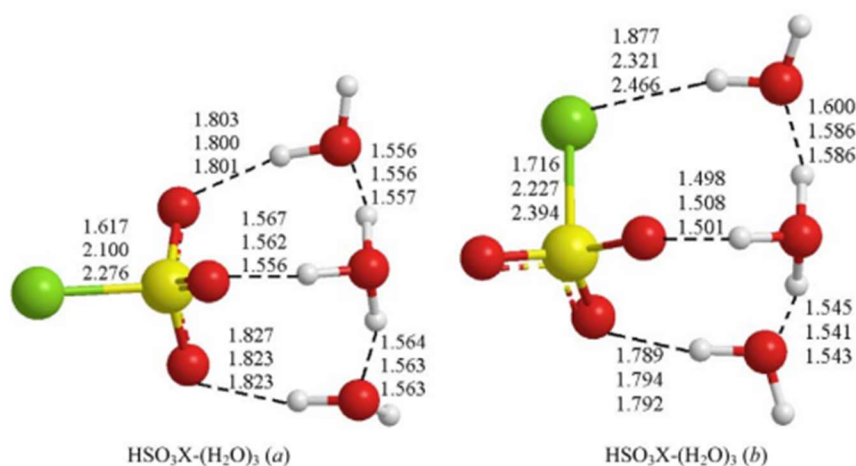
Fig. 1. Side views of the equilibrium geometries for the clusters HSO_3X–$(H_2O)_n$ (X = F, Cl, Br; n = 1–4) from B3LYP/6-311++G(d,p) calculations. Selected bond distances are shown for X = F (top value), Cl (middle), Br (bottom).

Figure 1 - The protonation of the water molecule on the right side of HSO_3-X when in a complex of 3 or more water molecules. Article published by Shujin Li and co-workers in 2006[15].

Section 1.4 – Cyclohexanecarboxaldehyde Literature Review

Thus far, cyclohexanecarboxylic acid remains an unobserved molecule in rotational spectroscopy. However, there are published studies describing the spectrum of cyclohexanecarboxaldehyde, a molecule very similar to cyclohexanecarboxylic acid. The difference between the molecules is in a single functional group; cyclohexanecarboxylic acid has a carboxyl group and cyclohexanecarboxaldehyde has an aldehyde. In terms of atoms, cyclohexanecarboxylic acid contains a single additional oxygen attached between the carbonyl

and the terminal hydrogen of the aldehyde. This change in molecular structure leads to a

significant difference in the rotational spectrum. Table 1 contains structural information and

rotational constants for cyclohexanecarboxaldehyde. They will be compared to our own findings

for cyclohexanecarboxylic acid in *Section 4.1*.

Table 1 - Rotational constants (MHz) and centrifugal distortion (kHz) of cyclohexanecarboxaldehyde. The paper was published in 1979 by Peter N. Kao and Paul H. Turner[16].

	Trans conformer		Gauche conformer	
	v = 0	*v = 0*	*v = 1*	*v = 2*
A	4,131.51	3,951.70	3,944.5	3,928.4
B	1,327.701	1,424.402	1,424.705	1,425.178
C	1,090.13	1,137.299	1,138.627	1,139.885
Δ_J	0.03			
Δ_{JK}	3.16			

Another paper, published in 1996, by Hassan M. Badawi used *ab initio* theory to simulate

the rotational spectra of cyclohexanecarboxaldehyde and cyclohexanecarboxylic acid fluoride

and chloride[17]. In this context, a*b initio*, meaning "from the beginning," indicates that the

theoretical work does not incorporate parameters derived from experiment. Consistent with the

observations of Kao and Turner, Badawi considered cis, trans, and gauche conformers (Figure 2)

of cyclohexanecarboxaldehyde.
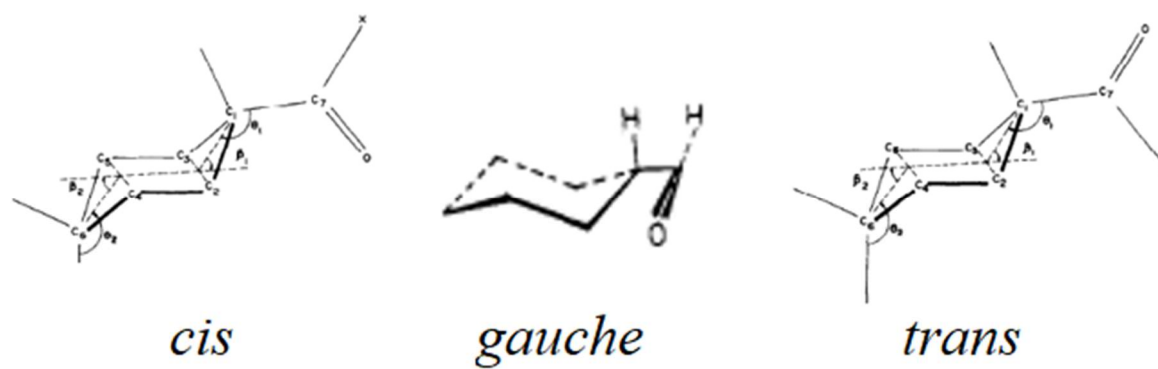
Figure 2 - Three most stable conformers of cyclohexanecarboxaldehyde observed by Badawi.

CHAPTER II

COMPUTATIONAL METHODS

Section 2.1 – Supercomputers

In the early days of computing, a computer constructed to carry out a single type of calculation could occupy a footprint of 160+ m^2 and weigh many tons. Such a computer is the Electronic Numerical Integrator and Computer (ENIAC), which was the first programmable and general-use digital computer, built in 1945. The inflation-adjusted cost of building ENIAC was $7,300,000[1]. 75 years later, humanity has developed computers that fit right in our pockets. Along with the development of technology comes the development of science. With the help of computers, there have been many breakthroughs in modern science. With the continuing development of artificial intelligence and new computing infrastructures such as quantum computing, there is still more room for humanity to advance as a species.

The Texas Advanced Computing Center (TACC) is home to Frontera, one of the most powerful supercomputers in the world. In addition to Frontera, the TACC maintains the following supercomputers: Wrangler, Maverick2, Stampede2, and Lonestar5. The main resource used in this thesis are the Lonestar5 and Stampede2 supercomputers.

Supercomputers are what provide the computing power for quantum chemical calculations to be carried out in the field of computational chemistry. This computing power, of course, extends to any other field that desires to construct a simulation using the supercomputer's capabilities. Examples of TACC's capabilities include simulations of the early universe[2] and of 800,000 years of earthquakes in California[3].

Section 2.2 – Gaussian

The Gaussian program was initially released in 1970 by John Pople and his research group. At the time, electronic structure theory was Professor Pople's focus, and this led him to continue the development of *ab initio* calculations for molecular structures. At the time, Gaussian was not the only program that could conduct molecular optimization. However, Gaussian 70 was the preferred program for general molecular observation because of its efficiency and ease of use[4]. It is not an understatement to say that John Pople was one of the leading scientists in computational chemistry laying down the foundation for the development of modern Hartree-Fock calculation, Self-Consistent Field (SCF), Perturbation Theory, and Couple Clustered methods.

Over the years, the Gaussian software has been updated and optimized to keep up with the modern development of computational chemistry. At the time of the writing of this thesis, the most current Gaussian software is Gaussian 16. This is one of the programs that is being run by the supercomputer at the TACC which is how the molecule is simulated and the structural optimization of our observed molecules is done; this is through quantum chemical calculations. With the combined power of the Gaussian software and the computing capabilities of the TACC supercomputers, molecules being observed theoretically can be structurally optimized to the modern day "gold standard," which is the Coupled-Cluster Singles and Doubles method with

Perturbative Triples, abbreviated as CCSD(T). This method is generally considered to yield highly accurate results for molecular optimizations at a manageable computational cost. Computational methods and basis sets will be discussed further in this chapter as these topics are the basics for understanding *ab initio* calculations.

Section 2.3 – Simulating a Microwave Spectrum with Pgopher

Pgopher is a convenient program that can be used to simulate electronic, vibrational, and rotational spectra of molecules[5]. After running *ab initio* calculations and obtaining an optimized molecular structure, Gaussian 16 prints values for the calculated rotational constants. The rotational constants of a molecule give us information on the molecule's characteristics and can be used to simulate its microwave spectrum. The values printed include the rotational constants (denoted A, B, and C), dipole moments along the corresponding principal axes of inertia (a, b, and c), and centrifugal distortion constants (D_J, D_{JK}, and D_K). These values are printed for every molecule even though some molecules may not have a permanent dipole along all three axes and may be entered in the Pgopher "Constants" window.
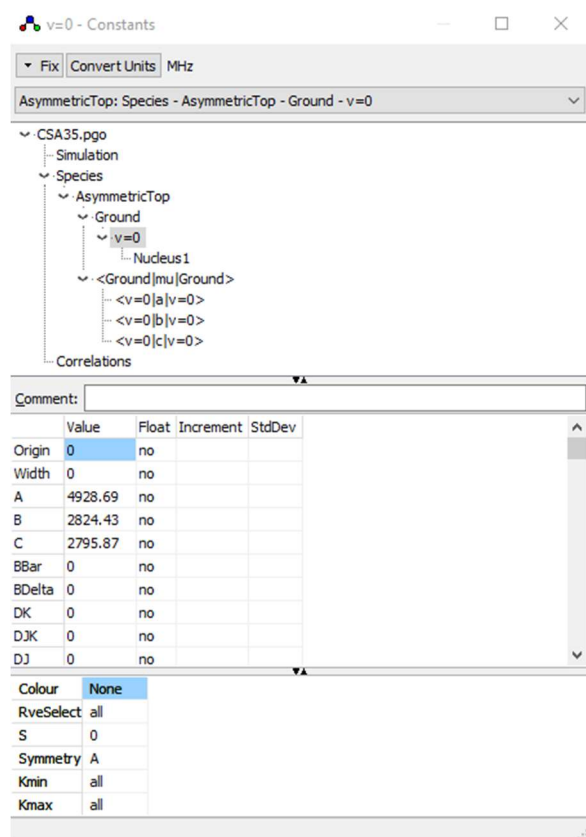
Figure 3 - Pgopher's "Constants" window to input theoretical rotational values for spectrum simulation.

Upon entering the values as shown in Figure 3, we get the following image from Pgopher.
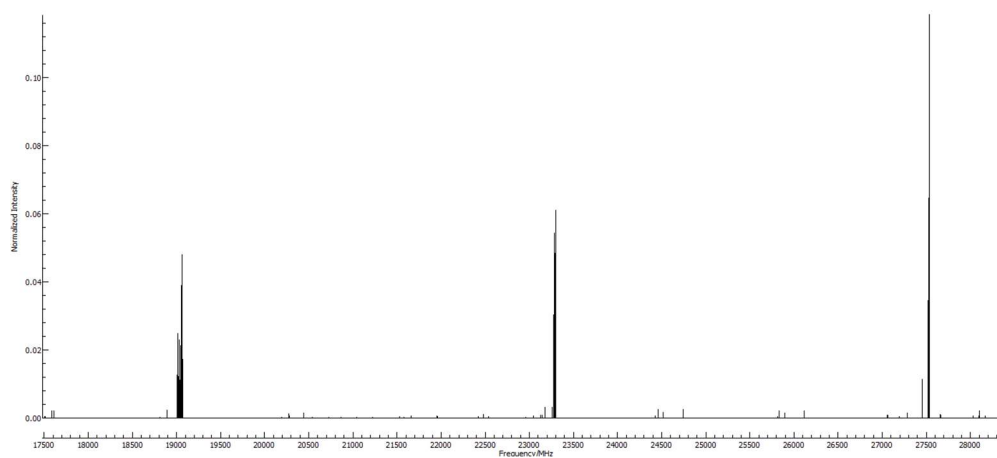
Figure 4 - Simulated spectrum showing rotational transitions using Pgopher.

The spectral range of UTRGV's *k* band Chirped-Pulse Fourier Transform Microwave spectrometer (CP-FTMW) is from 18 GHz to 26 GHz. That is why Figure 4 is limited to that range.

Section 2.4 – Schrödinger's Equation in Quantum Mechanics

Isaac Newton's laws of motion can be used to accurately represent classical motion. For example, classical mechanics can describe a bowling ball rolling and hitting another ball. However, the laws and models of classical physics, which describe nature at the macroscopic scale, do not adequately explain events that occur at the microscopic scale. Quantum mechanics was developed as an *ad hoc* theory when early 20th-century scientists tried to understand deviations from classical predictions in microscopic systems. These early proposals, now known as "old quantum theory," are the foundation that led to the full development of modern quantum mechanics.

Werner Heisenberg, Max Born, Niels Bohr, Max Planck, Albert Einstein, and Louis de Broglie are just a few of the scientists recognized for their major contributions to the development of quantum physics. However, one name comes to mind before all the others when discussing quantum mechanics: Erwin Schrödinger. The time-independent Schrödinger equation is as follow:

$$\hat{H}\psi = E\psi \tag{1}$$

This equation performs the same function that Newton's laws do classical mechanics; it predicts the behavior of a physical system. Let's look at the classical equation for the energy:

$$E = KE + PE \tag{2}$$

where *KE* is the kinetic energy of a system and *PE* is its potential energy. In the case of the classical harmonic oscillator, we have:

$$KE = \frac{1}{2}mv^2 \tag{3}$$

$$PE = \frac{1}{2}kx^2 \tag{4}$$

This same equation cannot be used to describe a quantum system such as a diatomic molecule. The classical equation must be redefined to accurately depict a quantum system. In a quantum system, instead of using equation 2 to define energy, we must quantize it by replacing the classical momentum $p = mv$ with the corresponding operator:

$$\frac{p^2}{2m} + \frac{1}{2}kx^2 = E \tag{5}$$

$$\hat{p} = \frac{\hbar}{i}\frac{\partial}{\partial x} \tag{6}$$

Combining equation 6 into equation 5, we get:

$$\hat{H} = -\frac{\hbar^2}{2m}\frac{\partial^2}{\partial x^2} + \frac{1}{2}kx^2 \tag{7}$$

In this way, the total energy corresponds to the Hamiltonian operator, $\hat{H}$. The Hamiltonian acts on the wavefunction, ψ, to generate the evolution of the wavefunction in time and space. When $\hat{H}\psi$ equals $E\psi$ the E value(s) give quantized energies of the system for the corresponding wavefunction(s), which describe the state of the system completely and in principle allow all other properties, such as dipole moments, to be calculated[6]. This is the basic approach used in computational methods to optimize molecular structures and obtain useful information about a molecule's behavior.

Section 2.5 – Methods

Several different methods can be used in computational chemistry. These methods are based on the principles of quantum mechanics just outlined. This is because the principles of classical mechanics cannot explain behaviors observed at the molecular and sub-molecular scales. When considering a quantum system, it is unpredictable what pathway certain factors will take. These factors include things such as electron density, magnetic field, and electron-electron interactions of a system. Thus, to quantify these factors to obtain usable results, assumptions for the molecular system must be made. It is also valid to view these assumptions as approximations or restrictions on the system. Each unique method involves a different set of approximations. The following methods will be discussed in more detail as they were used at some point in this study: Hartree-Fock (HF), Density Functional Theory (DFT), and Møller–Plesset perturbation theory (MP2).

The Hartree-Fock method is the mainstay of computational chemistry. The HF method underwent several revisions, however, before it became commonly accepted as an accurate approximation in quantum theory. In the 1920s, Douglas Hartree introduced the Hartree method, also known as the self-consistent field (SCF) method, to solve the many-body time-independent Schrödinger equation through quantum principles. However, this method did not consider electron indistinguishability. Hartree reformulated his method in 1935 into what is now known as the Hartree-Fock method, but it was not commonly used until the development of computers because of the tediousness of carrying out the calculations by hand. It is a good starting point for molecular optimization but imposes many restrictions on the molecular system in comparison to what occurs experimentally[7, 8]. The simplest antisymmetric wave function describing the ground state of an N-electron system is given by a Slater determinant, as follows:

13

$$| \psi_o > = | \chi1\chi2 \ldots \chi N > \tag{8}$$

where ψ_o is the antisymmetric wave function and the χ represents spin orbitals of the system. As the variational principle states, the best wave function is the one that gives the lowest possible energy, E_o. The variational flexibility of the wave function of equation 8 is dependent on the choice of spin orbitals. Let's consider:

$$E_o = \; < \psi_o | \hat{H} | \psi_o > \tag{9}$$

where $\hat{H}$ is the full electronic Hamiltonian. The equations which give the lowest possible E_o, with respect to first-order variations in the spin orbitals, is the Hartree-Fock equation:

$$f(i)\chi(x_i) = \mathcal{E}\chi(x_i) \tag{10}$$

where $f(i)$ is a one-electron operator called the Fock operator. The following equation denotes $f(i)$:

$$f(i) = -\frac{1}{2}\nabla_i^2 - \sum_{A=1}^{M}\frac{Z_A}{r_{iA}} + v^{HF}(i) \tag{11}$$

where $v^{HF}(i)$ is the Hartree-Fock potential which represents the average potential experienced by the ith electron due to the presence of other electrons. This approximation simplifies a many-electron problem into an effective one-electron problem. The Hartree-Fock equation is solved through the self-consistent field (SCF) method, in which the average field, v^{HF}, is calculated with an initial guess at the spin orbitals and is used to obtain information as to how the spin orbitals should change to reduce the energy. Once self-consistency is reached, the orbitals no longer change meaningfully, and the spin orbitals appearing in the Fock operator are the same as its eigenfunctions[9].

Density Functional Theory (DFT) methods incorporate much of the same information as the Hartree-Fock while also including an approximation treatment of the correlated motions of individual interacting electrons[10, 11]. A significant difference is that the DFT method treats the electron density as the primary object of study rather than the wavefunction, hence the name. In particular, the Hohenberg-Kohn theorem implies that the total energy of a system can be determined from the electron density in the following manner. The energy can be written as:

$$E[n(r)] = n(r) \; v_{ext}(r) \; dr + F[n(r)] \tag{12}$$

where v_{ext} is the external potential and $F[n(r)]$ is an unknown (but universal) functional of $n(r)$. The energy functional can further be shown to correspond to the ground-state energy of the Hamiltonian, $\hat{H}$, for a fictitious, non-interacting wavefunction, ψ:

$$E[n(r)] = < \psi| \; \hat{H} \; |\psi > \tag{13}$$

The Hamiltonian is written as:

$$\hat{H} = F + v_{ext} \tag{14}$$

where F is the electronic Hamiltonian and equals:

$$F = KE + V_{ee} \tag{15}$$

KE is the kinetic energy operator and V_{ee} is the interaction operator. F stays the same in all N-electron systems. This means that the Hamiltonian, $\hat{H}$, is dependent on the number of electrons, N, and the external potential, v_{ext}[12, 13]. Thus, the ground-state energy can be determined from electron density.

Published in 1934 by Christian Møller and Milton Plesset, Møller–Plesset (MP) perturbation theory was developed as a post-Hartree-Fock method. MP perturbation theory

improves upon the HF method by adding electron correlation effects using Rayleigh-Schrödinger

perturbation theory (RS-PT), most commonly to second, third, or fourth order

(MP2/MP3/MP4)[14]. MP2 perturbation theory was the only MP method used in this study. In

RS-PT, we have an unperturbed Hamiltonian, $\hat{H}_o$, and a small perturbation, $\hat{V}$ is added as

follows:

$$\hat{H} = \hat{H}_o + \lambda\hat{V} \tag{16}$$

where λ is an arbitrary real parameter. The perturbed wavefunction and energy can be expressed

as a power series in $\hat{V}$ in terms of λ:

$$\psi = \psi^{(0)} + \lambda\psi^{(1)} + \lambda^2\psi^{(2)} + \lambda^3\psi^{(3)} + \dots \tag{17}$$

$$E = E^{(0)} + \lambda E^{(1)} + \lambda^2 E^{(2)} + \lambda^3 E^{(3)} + \dots \tag{18}$$

The perturbed parameters are then substituted back into the time-independent Schrödinger's

equation discussed in *Section 2.4*:

$$(\hat{H}_o + \lambda\hat{V})\,(\psi^{(0)} + \lambda\psi^{(1)} + \dots) = (E^{(0)} + \lambda E^{(1)} + \dots)\,(\psi^{(0)} + \lambda\psi^{(1)} + \dots) \tag{19}$$

After expanding the products through simple algebra and equating the coefficients on each side,

a series of relations are obtained for increasing orders of perturbation. The following equations

correspond to powers of *0, 1,* and *2* of λ:

$$(\hat{H}_o - E^{(0)})\,\psi^{(0)} = 0 \tag{20}$$

$$(\hat{H}_o - E^{(0)})\,\psi^{(1)} = (E^{(1)} - \hat{V})\,\psi^{(0)} \tag{21}$$

$$(\hat{H}_o - E^{(0)})\,\psi^{(2)} = (E^{(1)} - \hat{V})\,\psi^{(1)} + E^{(2)}\,\psi^{(0)} \tag{22}$$

With this, we have an understanding of how general perturbation theory works[15].

However, the methods we have discussed are not the only factors taken into consideration by the

computer when optimizing a molecular structure. HF, DFT, and MP2 methods are also

influenced by basis sets which are discussed in the following section (*Section 2.6*).

Section 2.6 – Basis Sets

The choice of basis set is an important component of most quantum chemical

calculations. Each basis set specifies approximate one-electron orbitals contributed to the

molecular system by its constituent atoms, allowing the molecular orbitals to be expressed as a

linear combination of these "basis functions." An individual molecular orbital, Φ_i, is described as

follows:

$$\Phi_i = \sum_{\mu=1}^{N} c_{\mu i} \chi_\mu \tag{23}$$

where $c_{\mu i}$ are the molecular orbital expansion coefficients. χ_μ represents and individual basis

functions[16]. The variational method is then used to solve for the best choice of the expansion

coefficients, and thus the optimal molecular orbitals. The "best" parameters are those yielding

the lowest ground state energy[17].

The main basis set used for the calculations in this thesis was aug-cc-pVTZ. Augmented

(aug) basis sets have a set of diffuse functions added for every angular momentum in the basis

set and are generally denoted as aug-cc-pV*n*Z where V indicates that it is a valence-only basis set

and *n*Z states whether the basis set is double, triple, quadruple (D,T,Q, etc.) zeta. The

correlation-consistent polarized (cc-p) basis sets are the current state-of-the-art basis sets used for

molecular optimization[18, 19].

Having discussed all the individual aspects that contribute to molecular simulation, we can piece together the theoretical process used for this study. Using the supercomputers located at the TACC, we run the Gaussian 16 program to conduct the quantum chemical calculations using DFT and MP2 methods and the aug-cc-pVTZ basis set. Gaussian simulates and optimizes molecular structure and computes the molecules' rotational constants. These constants are inputted into Pgopher which simulates the rotational spectra using a model Hamiltonian to yield our theoretical spectra.

CHAPTER III

MICROWAVE SPECTROSCOPY

Section 3.1 – History of Microwave Spectroscopy

Microwave spectroscopy is an analytical method used to detect rotational transitions of

molecules. These experiments are done in a chamber that is kept at high vacuum to minimize the

interference of impurity molecules. The target molecule is seeded in a carrier gas and enters the

chamber from a pressure background through a pulsed nozzle. The molecules undergo

supersonic expansion in this process. This sets up a suitable environment to begin observing how

molecules will react to being bombarded with microwave radiation. The molecules, which are in

their energy ground-state, absorb the radiation and become excited. After the microwave

radiation stops, however, the molecules will eventually relax to their ground state by emitting

radiation. This radiation is the focus of microwave spectroscopy. The signals are collected in the

time domain and Fourier-transformed into frequency domain. This allows time-dependent

signals collected by the spectrometer to be converted into a single spectrum for interpretation.

In 1934, Claud Edwin Cleeton and Neal Hooker Williams made a breakthrough measurement using microwave frequencies[1]. Cleeton and Williams observed the absorption of microwave radiation by ammonia (NH_3) with a low-resolution, semi-optical spectrometer that used a split-anode magnetron source with an echelette grating for the measurement of wave lengths. This was the first measurement in the microwave region set the groundwork for the development of microwave spectroscopy. With the development of a new spectroscopy came technological advances, such as the invention of the radar, and new branches of research, such as scanning the interstellar medium for molecules through microwave spectroscopy[1].

A few years after this first measurement in the microwave range, the National Bureau of Standards (NBS) and the National Institute of Standards and Technology (NIST) began their first projects to work on microwave spectroscopy led by Harold Lyons and NBS Director Edward U. Condon[2]. Interestingly, microwave spectroscopy rose to be a very popular subject before World War II (WWII) and during the war. It was in 1942 where the United States Armed Services recognized the importance of long-distance radio transmission. This led to establishing the Interservice Radio Propagation Laboratory (IRPL) within the NBS[2]. With the advancement of radar technology, a Microwave Standards Group was established in 1944 with Dr. Lyons as the head. The growth of the NBS was explosive going from a group of no more than 5 persons to a group of 80 within the next year. In the years following WWII, the IRPL became the Central Radio Propagation Laboratory (CRBL)[2, 3]. The funding for the project also increased greatly and with that also came much research of molecules in microwave spectroscopy. That is the importance of this history; it is to show the growth of microwave spectroscopy. As an illustration, Figure 5 charts the budget for the NBS as microwave spectroscopy began receiving more attention. Furthermore, more molecules began to be observed in microwave spectroscopy

as shown in Figure 6.
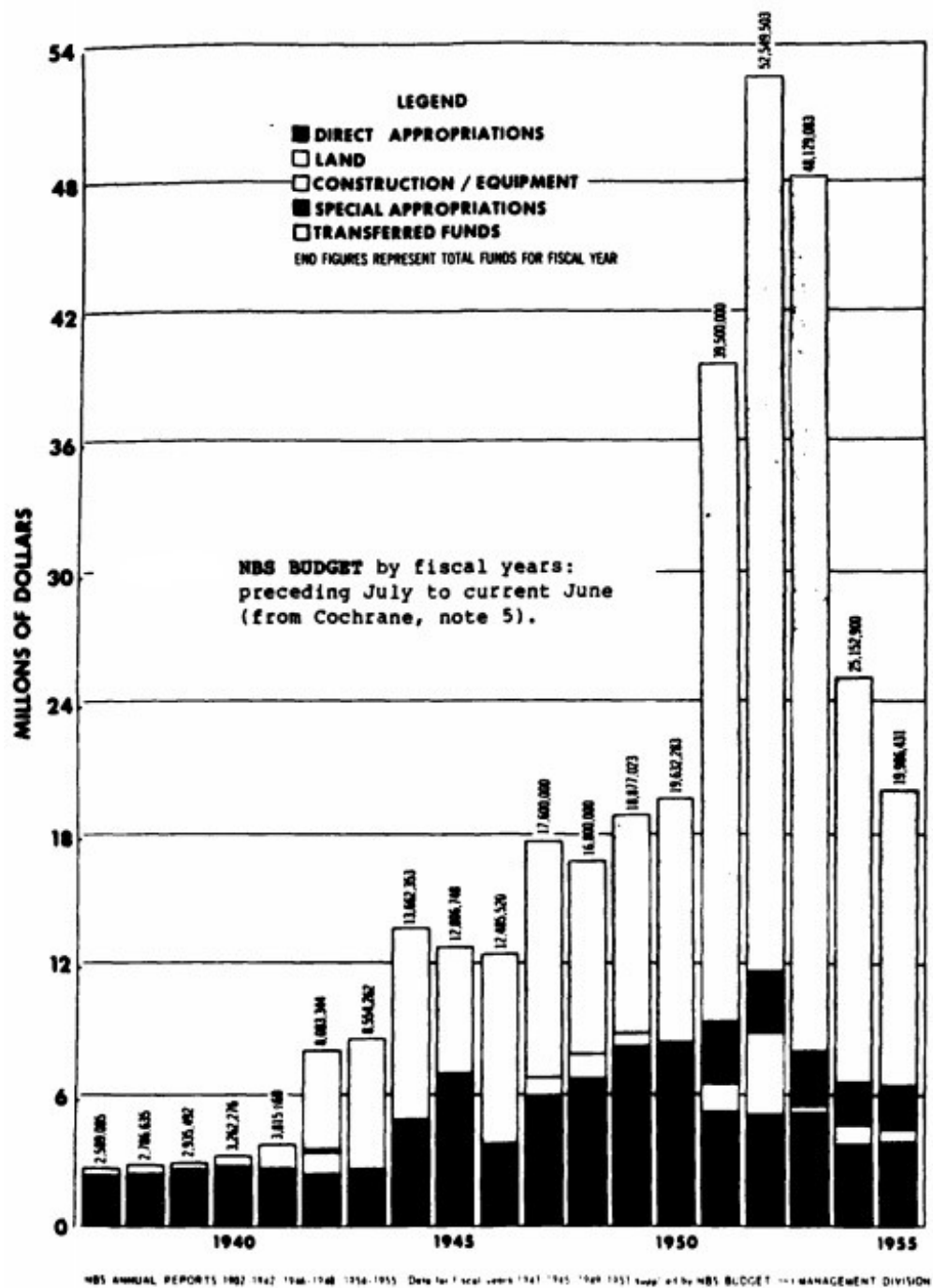
Figure 5 - NBS budget over the years as the attention for microwave spectroscopy grew. Chart not adjusted for inflation[2].

Total number of
molecules studied by
microwave spectroscopy
(from Townes, note 2).
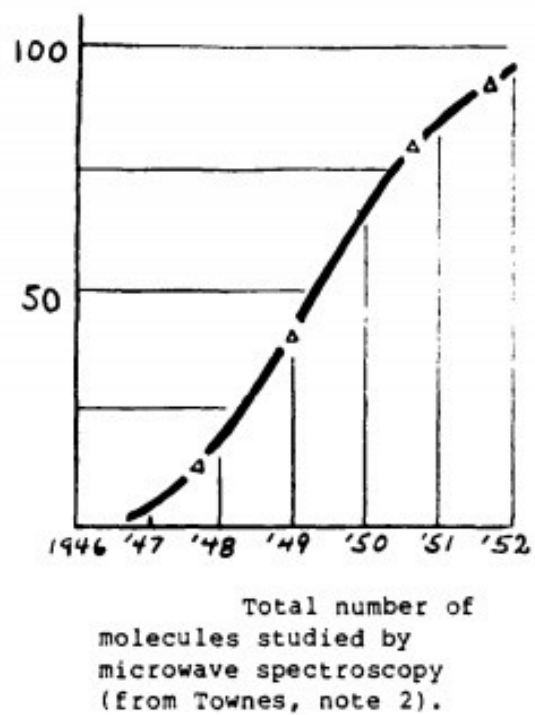
Figure 6 - Number of molecules the NBS studied with microwave spectroscopy between 1946 and 1952[2].
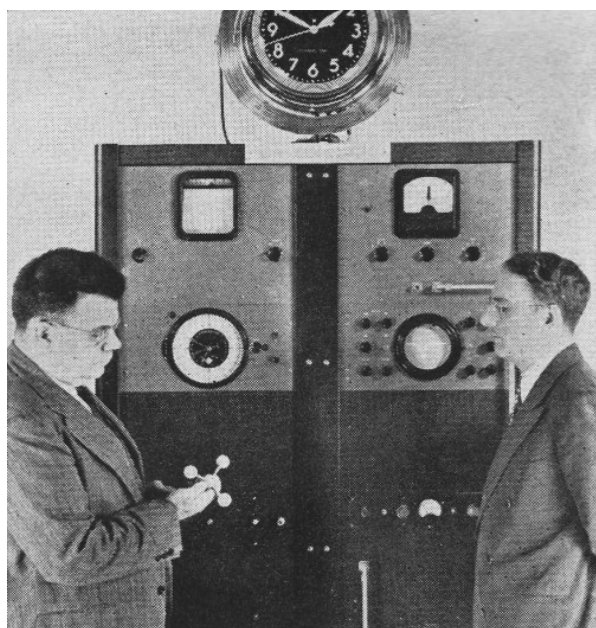
Figure 7 - Director Edward Condon (left) and Dr. Harold Lyons (right)[4].

In 1949, Dr. Harold Lyons successfully controlled a clock using an ammonia microwave line as show in Figure 7. This was significant because only a few years after microwave spectroscopy was invented, scientists were developing important practical applications of microwave spectroscopy.
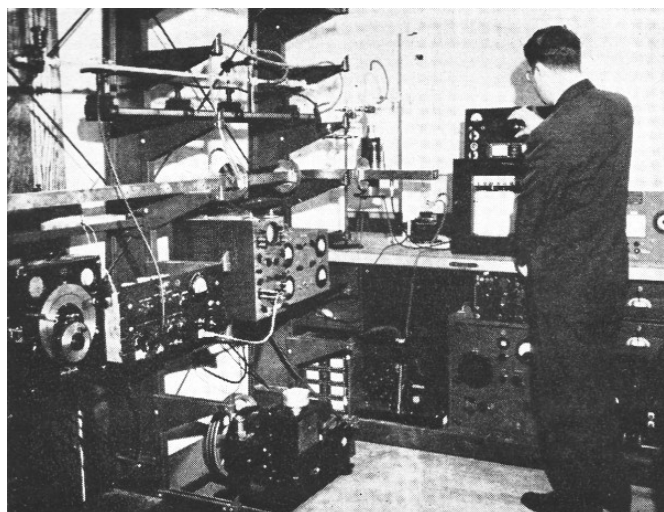
Figure 8 - NBS microwave spectrometer[4].

Figures 7 and 8 were captured around 1949, when Dr. Lyons' ammonia-clock experiment was successfully completed[5]. In 1954, the NBS began a sustained research program in microwave spectroscopy and proceeded to observe hundreds of molecules and reached out to several scientists. Microwave spectroscopy only grew as time went on and branched out into other topics of research such as in 1969, when the first organic interstellar molecule was detected by Lewis Snyder and other scientists through microwave spectroscopy[6].

With the technological advancement of computers, microwave spectroscopy became much more efficient and less tedious to conduct research. Fourier transform microwave spectroscopy allowed data collected in the time domain to be converted into the frequency domain for easier interpretation of data. Microwave spectroscopy and Fourier Transformation were revolutionized along with the development of computers. The time was an era where

everything was coming together for microwave spectroscopy. Years after the first organic interstellar molecule was observed, the microwave spectroscopy technique was revolutionized in 1981 by the Farby-Perot cavity microwave spectrometer[7]. In 2006, another breakthrough in microwave spectroscopy was achieved when the first chirped-pulse microwave spectrometer was built[8]. Like anything else, state-of-the-art technology is very expensive to obtain and maintain. However, over time, the price of microwave spectrometers has decreased and their availability for research has increased. The microwave spectrometer at UTRGV is a *k* band Chirped-Pulse Fourier Transform microwave spectrometer, which was purchased from a commercial company BrightSpec, is shown in Figure 9.
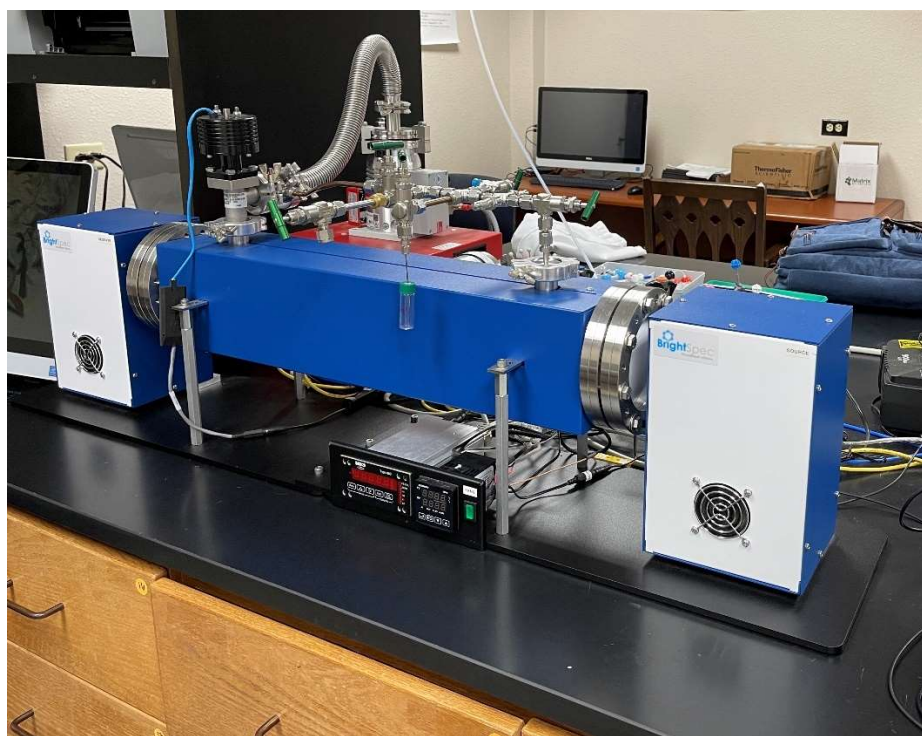
Figure 9 - UTRGV's k band Chirped-Pulse Fourier Transform microwave spectrometer purchased from commercial company BrightSpec[9].

Section 3.2 – Microwave Spectrometers: Cavity-Based and Chirped-Pulse

Nowadays, there are two main types of microwave spectrometers in common use: cavity-based and chirped-pulse microwave spectrometers. Because commercialization of microwave spectrometers is at its initial stages, the prices of these instruments lead some spectroscopists to build their own instruments for research. Cavity based microwave spectrometers, like the one in Figure 10, largely follow the set-up described by Balle and Flygare in 1981.
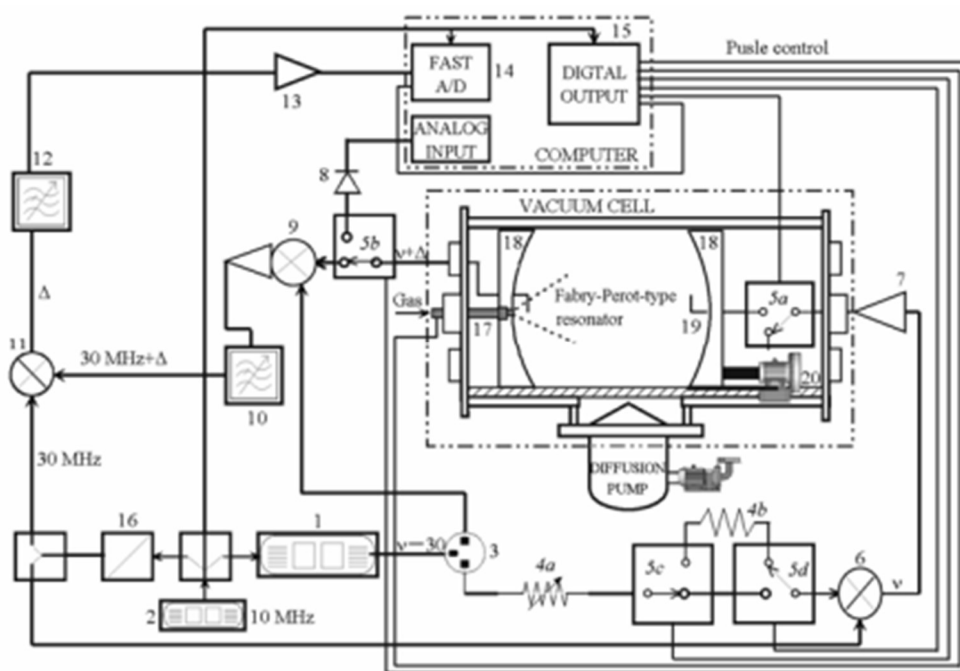
Figure 10 - Drawing of a Pulsed Nozzle FTMW[10]. This follows a similar setup to the one described by Balle and Flygare. The full description is in reference 10.

The advantage of the cavity-based FTMW spectrometer is that the instrument has greater precision. However, the chirped-pulse FTMW spectrometer adds waveform generators, widens the bandwidth by several 1000x, and decreases the amount of time need to conduct spectral searches[11]. The following figure depicts CP-FTMW spectrometers.
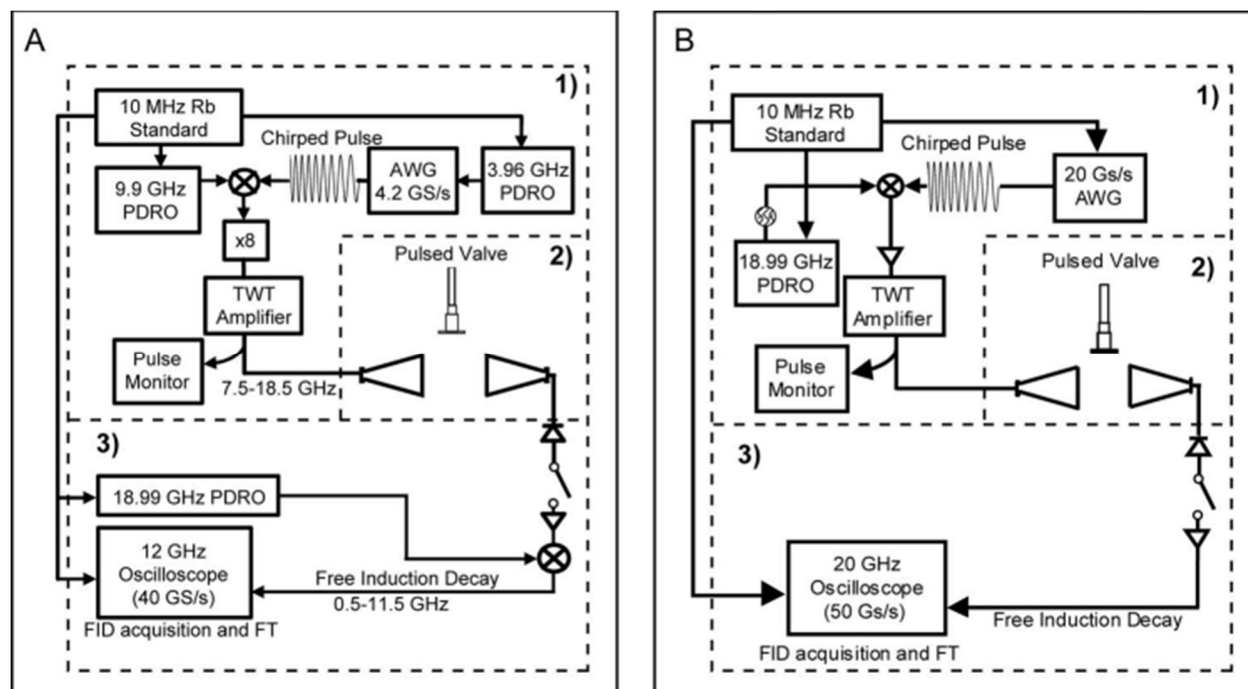
Figure 11 - Drawings of two Chirped Pulse FTMW spectrometer set ups[12]. The main difference between Panel A and B is how the chirped pulse is generated as well as how the Free Induction Decay signal is converted and digitized. More details in reference 12.

We have briefly discussed the two modern methods of microwave spectroscopy that are used and their specific advantages. Let's discuss the conditions at which microwave spectrometers are kept while observing molecules. The chamber in which the molecules are exposed to microwave radiation is kept at high vacuum pressure. This "high vacuum pressure" is defined to be between 1 millitorr and 1 nanotorr[13]. A typical vacuum pressure maintained in the chamber of a microwave spectrometer is about 1 microtorr. High vacuum pressures require multi-stage pumps, such as a diffusion pump, to remove air from a chamber. The internal pressure of the chamber can be monitored using an ion gauge. Having the molecules shift from atmospheric pressure to high vacuum pressure through a small nozzle causes them to undergo supersonic expansion. This adiabatic expansion cools the molecules to about 2 Kelvin, and it also

ensures that we have a system in which there are no intermolecular collisions. This is shown in Figure 12.
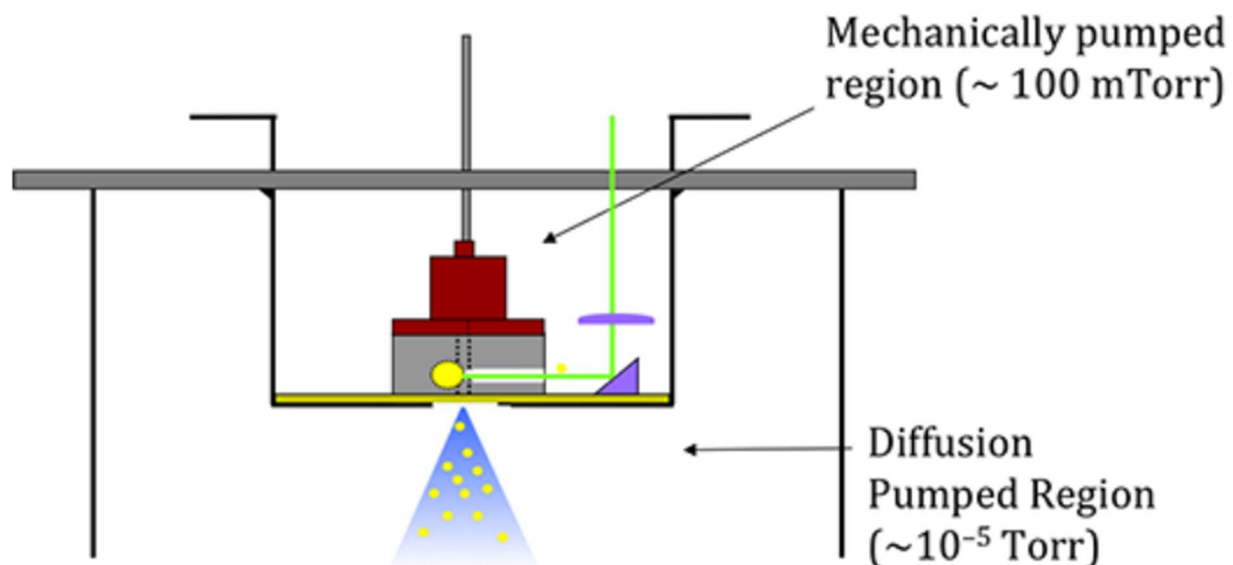
Figure 12 - Supersonic expansion shown by the Ken Leopold Research Group from the University of Minnesota[14]. The mechanically pumped region is considered high pressure in comparison to the pumped region. As the molecules expand into the vacuum pressure region at high velocity, their temperature drops because of no collisions.

This rarefied chamber is the environment in which the molecules of interest are excited with microwave radiation. As the molecules relax back to the ground state, they collectively undergo a time-dependent energy emission known as a Free Induction Decay (FID). The FID signal is amplified, upconverted or downconverted (depending on the spectrometer setup) and digitized with an oscilloscope. This digitized FID is Fourier-transformed into a spectrum that can be used for fitting.

Section 3.3 – Running an Experiment Using a CP-FTMW Spectrometer

Running a sample takes longer than one would think. There are several things to consider: the health of your electronics, pumping the air out of your chamber carefully, making sure your sample cell does not have air leaks, and in the case of using the CP-FTMW

spectrometer at Missouri Science and Technology University, whether the carrier gas was flowing at a good rate. Additionally, we had to be careful when using the software that controlled the chirped pulses as we did not want to relay a command when we did not need it. All the photos in this section were taken during our visit to Missouri S&T University in collaboration with Dr. G. Smitty-Grubbs and his research group. The CP-FTMW spectrometer used is shown in Figure 13.

Figure 13 - Chirped Pulse FTMW spectrometer at the Missouri University of Science and Technology. This was the instrument used to run cyclohexanecarboxylic acid.

In preparation to run our sample of cyclohexanecarboxylic acid, we first had to remove the sample that was in the sample cell. To do this, we first had to remove the lid (Figure 14),

which was on top of the spectrometer. To remove the lid, we closed off the diffusion pump from the chamber and vented the chamber. If air leaks into the diffusion pump, the silicone oil within the pump would harden and the diffusion pump would stop working. Once the diffusion pump was sealed off from the chamber, we would let air in by removing a copper rod that was used to create a seal. With air in the chamber, the top lid could be removed.
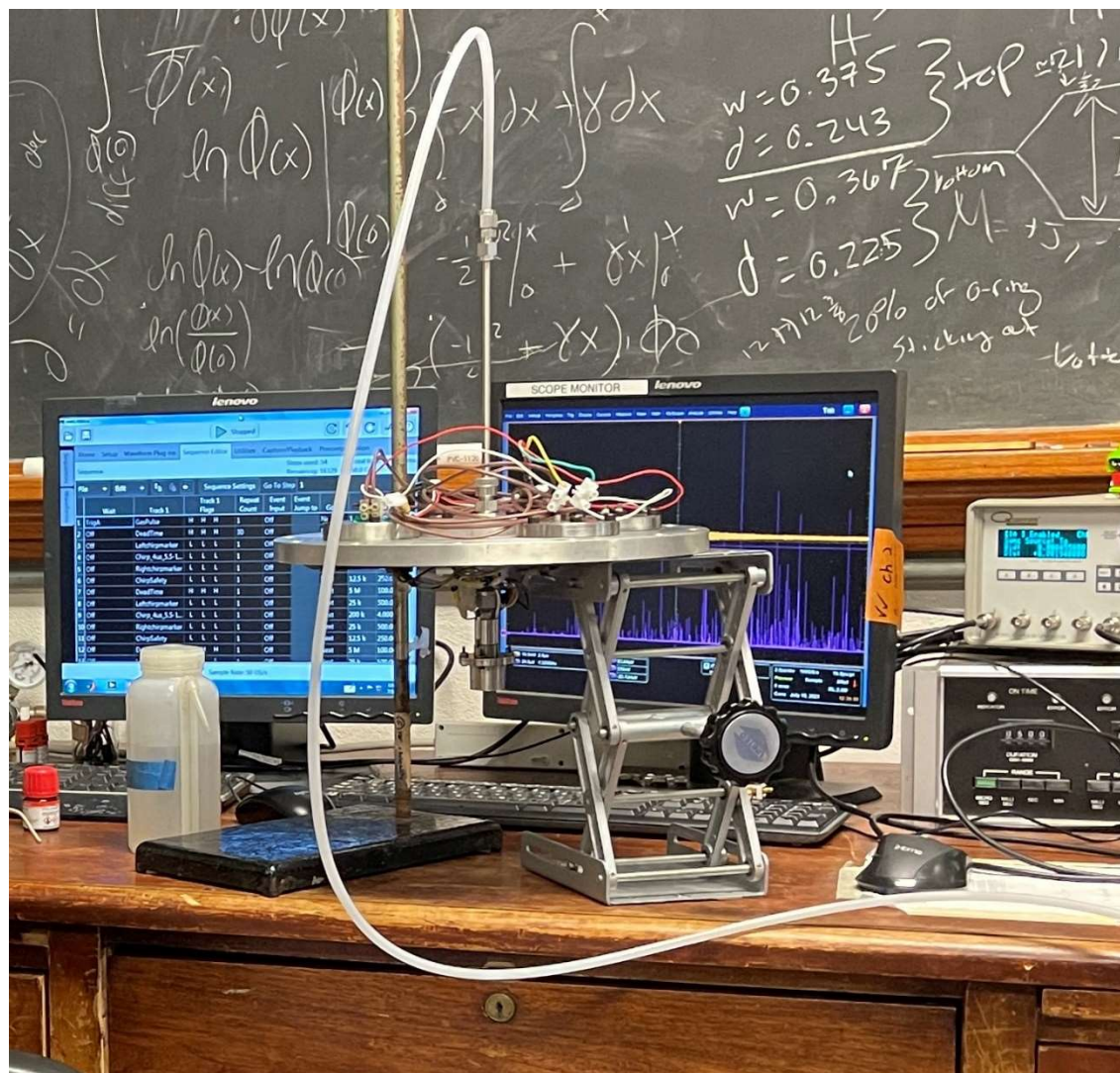
Figure 14 - Top lid of the CP-FTMW spectrometer which still has the sample cell attached. This sample cell must be tested before each run to make sure there are no air leaks.

Once removed, the sample cell was cleaned in preparation to add cyclohexanecarboxylic acid (CHCA). Once cleaned, we attached the empty sample cell again to find and mark the

29

optimal position at which the sample cell would release the sample along with the carrier gas.
The rate at which the sample and argon would be released into the chamber was controlled by a
valve driver. The empty sample cell was removed again after finding the optimal position.
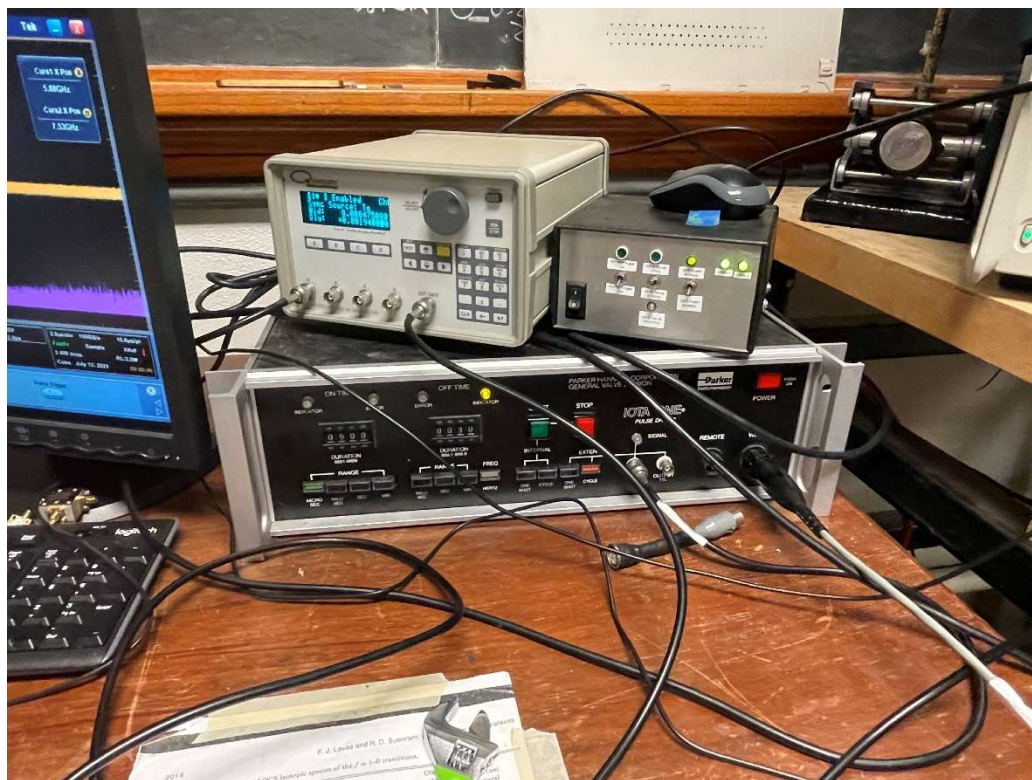
Figure 15 - Iota One valve driver used to control the rate of sample release into the vacuum chamber.

After adding CHCA to the sample cell, the sample cell was screwed on again. The cell
was then tested using the valve driver to make sure that there were no air leaks. We then attached
the heating device to the cell. Since the vapor pressure of CHCA is low, the vaporization of the
sample was aided by a heat-able nozzle. The temperature of the sample cell was monitored with
the device in Figure 16 and the temperature could be changed from the device in Figure 17.
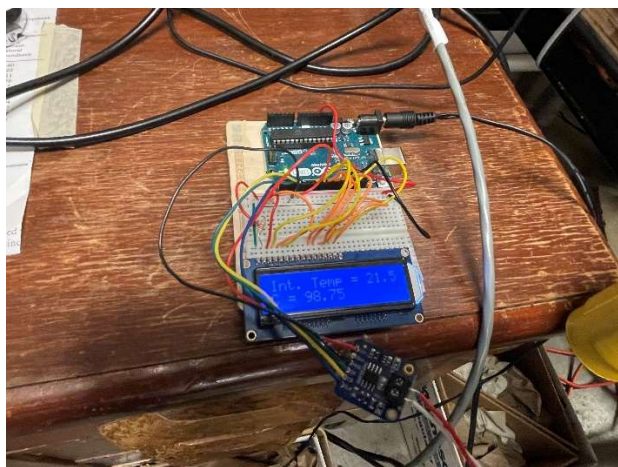
Figure 16 - Device used to monitor the temperature of the sample cell.

Figure 17 - Device used to control the temperature of the sample cell.

Once we had the sample ready and, on the lid, we reattached the lid to the chamber. We would then begin the process of getting the chamber to high vacuum pressure. This was mainly carried out by the diffusion pump, but the process takes several hours. For this reason, we would leave the chamber to pump overnight so that it would be at high vacuum pressure the following morning. The pressure of the vacuum chamber was monitored with an ion gauge shown in Figure 18.

Figure 18 - Ion gauge used to measure pressure in low-pressure environments.

Once the high vacuum pressure was reached, the spectrum acquisition began. Using a

computer program, we were able to send commands to the CP-FTMW including the frequency

range that we would observe and when to send microwave signals etc. The observation of CHCA

was split up into 3 different ranges: 5.5 – 10.25 GHz, 9.75 – 14.5 GHz, and 14 – 18.75 GHz.

Each range had a scan length of 100,000 acquisitions which took several hours for each scan.

The acquisitions were added and averaged to form a spectrum using the oscilloscope in Figure

19.
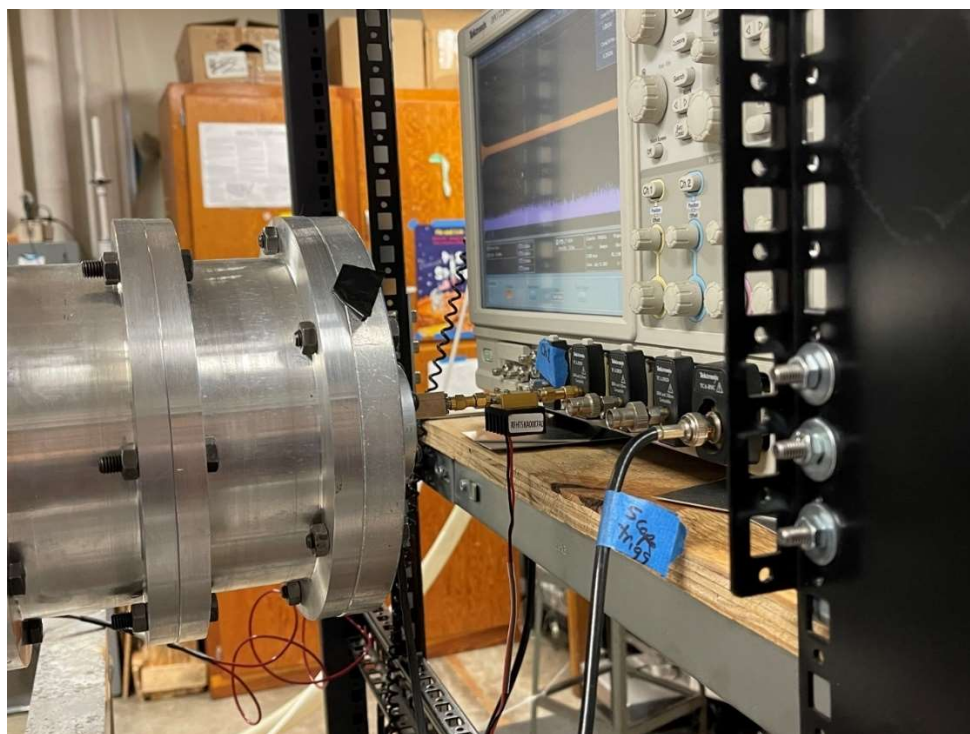
Figure 19 - Microwave chamber connecting to the Digital Phosphor Oscilloscope. Here, the signals of the molecules undergoing FID are collected, added, and averaged.
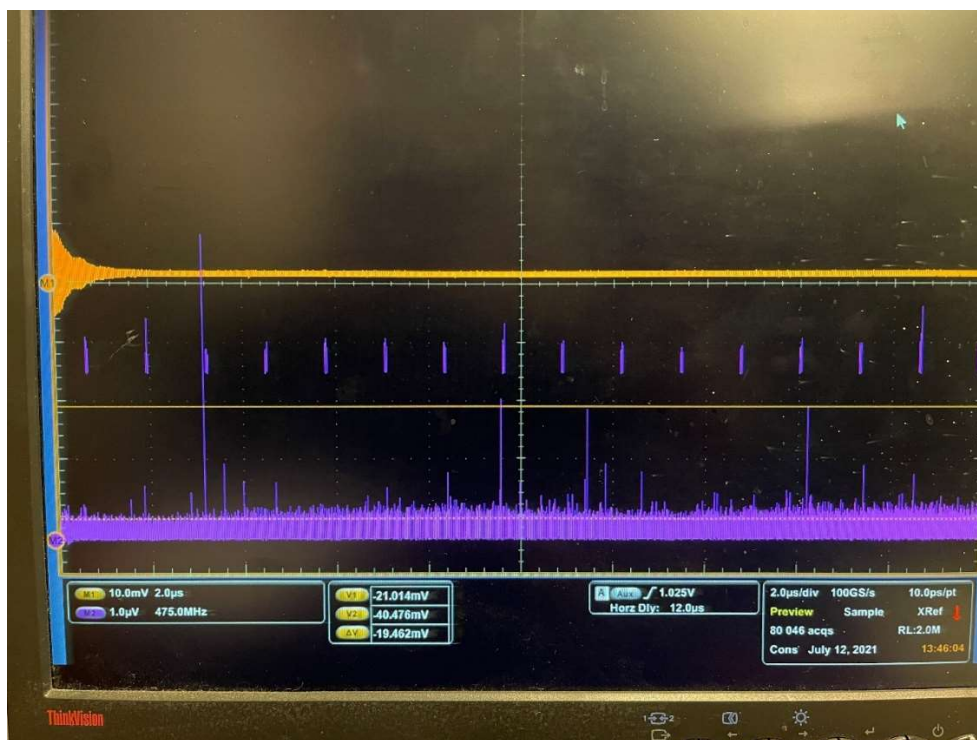
Figure 20 - CHCA spectrum at 80,000 acquisitions. The averaged FID signal is yellow, and the spectrum is purple.

33

Upon having the theoretical and experimental spectrum of a molecule, like the one in Figure 20, it is time to assign the spectrum. This will be done using the computer software called PGOPHER which we discussed in Chapter 2 (*see section 2.3*). The assignment of an experimental spectrum to a theoretical spectrum is important because it confirms the molecular characteristics of the observed molecule.

Section 3.4 – Rotational Spectroscopy: Explained by the Rigid Rotor

In rotational spectroscopy, microwave radiation is used to excite molecules from the ground state to an excited state. The energy input is not enough to make molecules undergo electronic or vibrational transitions but is enough to make them rotate. This is shown in Figure 21. The initial absorption and the subsequent emissions of the microwave energy are known as rotational transitions. Generally, these transitions are associated with weaker signals than electronic or vibrational transitions. To enable measurements of the rotational spectrum, amplifiers are used to make these signals stronger.
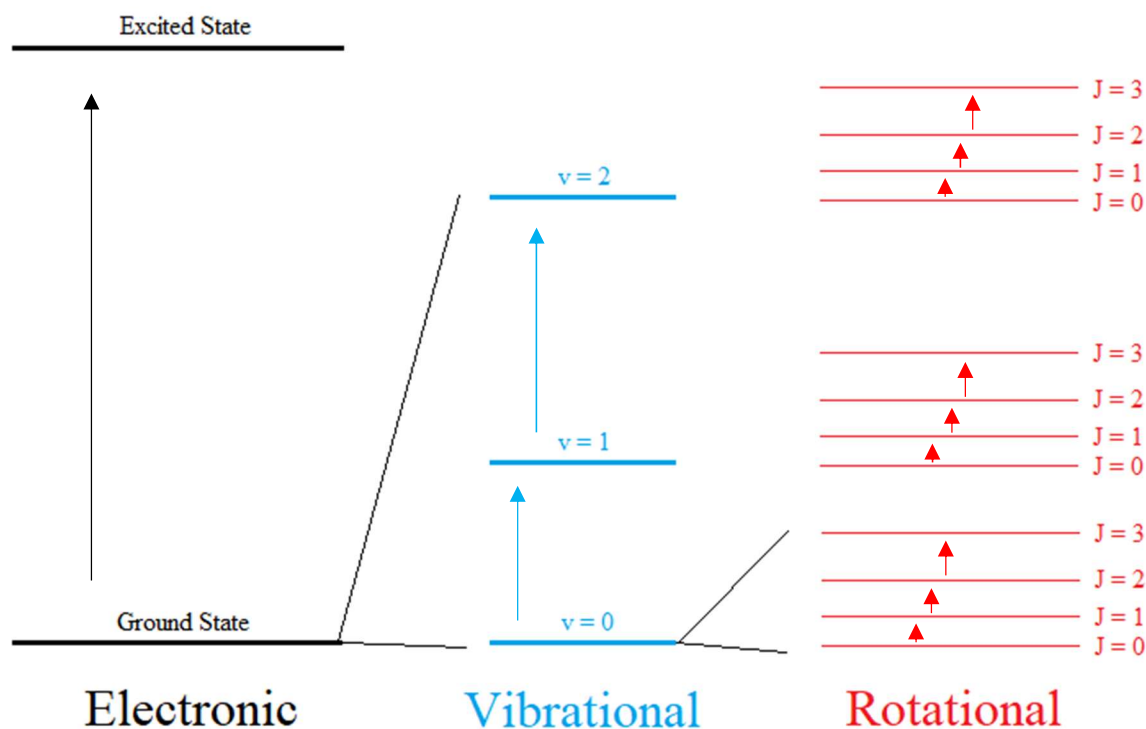
Figure 21 - Relative energies between electronic, vibrational, and rotational ($E_e > E_v > E_{rot}$) transitions. Not to scale.

Every rotation molecule belongs to one of four categories shown in Table 2. The categories are as follows: diatomic molecules, linear molecules, spherical tops, symmetrical tops, and asymmetrical tops[15]. The molecules within each category can have a variety of differing characteristics, such as different symmetries and dipole moments. Within each category, however, they all exhibit the same relationship among their principal moments of inertia.

Table 2 - The 4 categories of molecules in which molecules can be and their moment of inertia[16]. Each category will be discussed in this section.

Diatomic and Linear Molecules		$I_a = I_b$, $I_c = 0$
Spherical Tops		$I_a = I_b = I_c$
Asymmetrical Tops		$I_a \neq I_b \neq I_c$
Symmetrical Tops $I_a = I_b \neq I_c$	Oblate	$I_c > I_a = I_b$
	Prolate	$I_c < I_a = I_b$

Diatomic molecules, as the name suggests, consists of two atoms that are bonded together. However, it is not as simple as any two atoms; in rotational spectroscopy, the molecule MUST have a dipole moment. If it does not have a dipole moment, the molecule cannot be observed through rotational spectroscopy because it does not couple to the electric field. This is, in fact, the case in any of the categories. Just to give some examples, gas molecules such as H_2, O_2, and N_2, do not have a dipole moment and, therefore, are not observed in rotational spectroscopy. We can observe diatomic molecules with dipole moments such as CO, HBr, and HCl. There is a model, known as the rigid rotor, that represents the rotational motion of a molecule. This model does not account for the stretching of molecules as they rotate, hence the name rigid. The non-rigid rotor model does consider this stretching and labels the stretching as centrifugal distortion. The goal of the following example is to provide an explanation with one of the most basic scenarios in rotational spectroscopy. First, let's recall linear motion and compare it to circular motion. The equations in Table 3 are important to keep in mind when discussing the rigid rotor example as the motion we are focusing on is circular.

Table 3 - Linear motion equations shown in terms of circular motion.

Linear Motion	v	$p = mv$	$KE = \frac{1}{2} mv^2$	$KE = p^2 / 2m$
	Velocity	Momentum	Kinetic Energy	Kinetic Energy
Circular Motion	$\omega = v / r$	$L = I\omega$	$KE = L^2 / 2I$	$KE = I\omega^2 / 2$
	Angular Velocity	Angular Momentum	Kinetic Energy	Kinetic Energy

Let's consider a diatomic molecule that is composed of $m1$ and $m1$ to be the model for our rigid rotor.
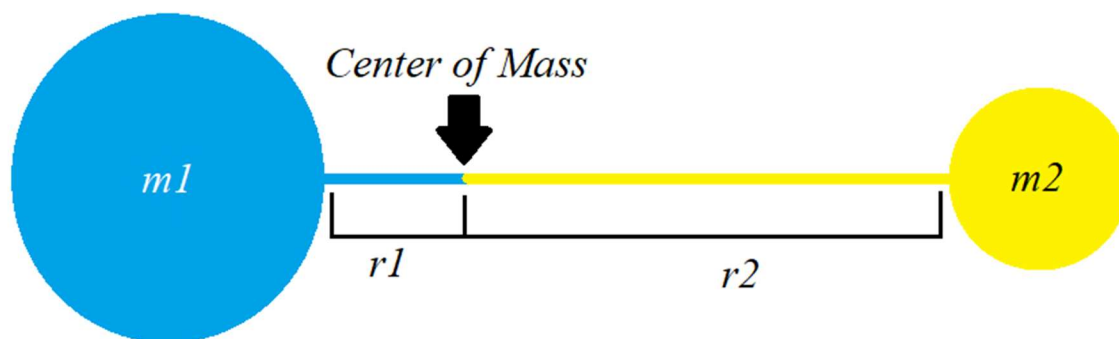
Figure 22 - Diatomic molecule with two masses $m1$ and $m2$ as well as two radii, $r1$ and $r2$.

The rigid rotor assumes that the distance between these two molecules is fixed and will not change while it is rotating. We can calculate the moment of inertia, which quantifies the resistance to the rotating motion, with the following equation:

$$I = \mu r^2 \tag{23}$$

$$\mu = \frac{m1 * m2}{m1 + m2} \tag{24}$$

μ being the reduced mass and r being *r1 + r2*. We will consider the center of mass to be the origin of the rotating particles and *m2* is the particle that moves around its origin. This can be interpreted as a single body of mass, μ, rotating around the origin at a fixed distance, *r*.
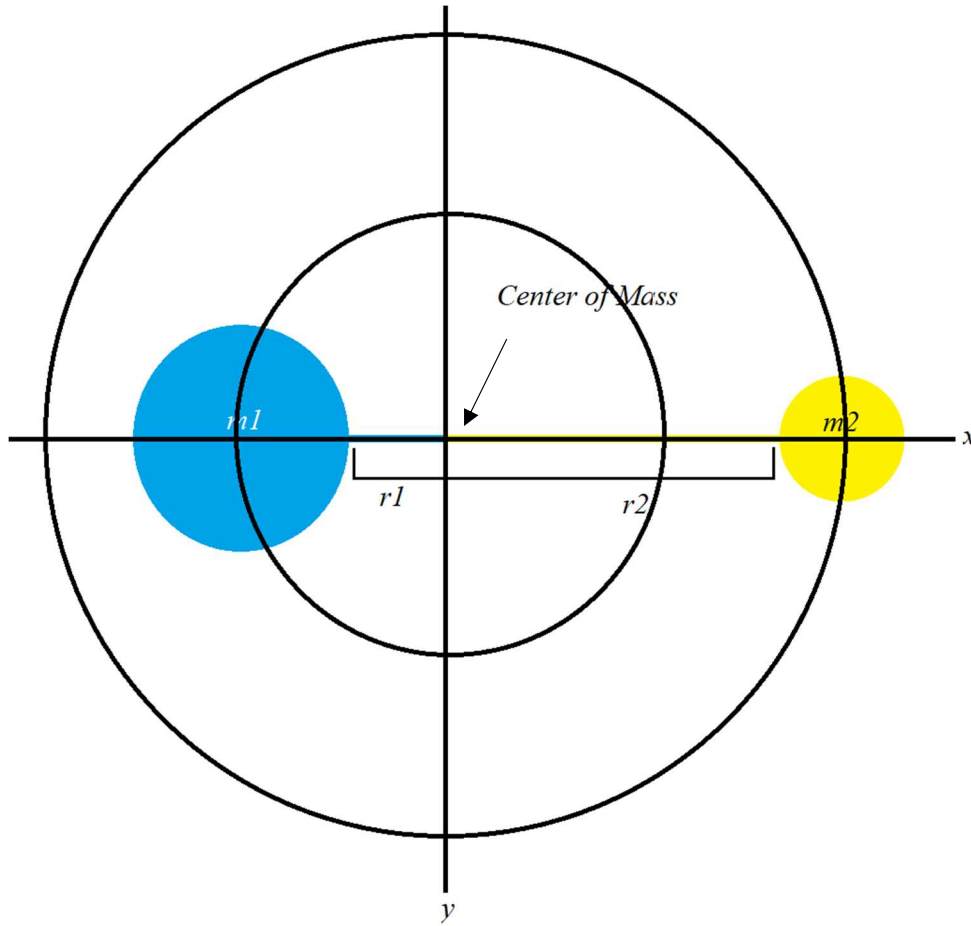
Figure 23 - The two-body problem now becomes a one-body problem.

The angular momentum, L, can be expressed as shown in Table 3 where $L = I\omega$. The kinetic energy will also be expressed in terms of circular motion as $KE = L^2 / 2I$. Angular momentum, *L*, is a vector defined as:

$$\vec{L} = \vec{r} \times \vec{p} = \begin{vmatrix} \hat{\imath} & \hat{\jmath} & \hat{k} \\ x & y & z \\ p_x & p_y & p_z \end{vmatrix} = (yp_z - zp_y)\,\hat{\imath} + (zp_x - xp_z)\,\hat{\jmath} + (xp_y \quad yp_x)\,\hat{k} \qquad (25)$$

and thus,

$$\vec{L} = L_x\hat{i} + L_y\hat{j} + L_z\hat{k} \text{ and } \hat{L}^2 = L_x{}^2 + L_y{}^2 + L_z{}^2 \tag{26}$$

It has been shown that the angular momentum operators $\hat{L}_x$, $\hat{L}_y$, and $\hat{L}_z$ do not commute with each other, but do commute with $\hat{L}^2$[17, 18]. This lets us know that the angular momentum component operators do not have a common set of eigenfunctions. Their commutation with $\hat{L}^2$ shows, however, that any one of the component operators can be chose to define a simultaneous eigenfunction for the rotating system.

Table 4 - The angular momentum operators do not commute with each other, but commute with $\hat{L}^2$.

	$[\hat{L}_x, \hat{L}_y] = i\,\hbar\,\hat{L}_z$
Do not commute	$[\hat{L}_y, \hat{L}_z] = i\,\hbar\,\hat{L}_x$
	$[\hat{L}_z, \hat{L}_x] = i\,\hbar\,\hat{L}_y$
Do commute	$[\hat{L}^2, \hat{L}_x] = [\hat{L}^2, \hat{L}_y] = [\hat{L}^2, \hat{L}_z] = 0$

Using the classical-mechanical observables in equation 25, we can list the corresponding quantum-mechanical operators[17, 18]:

$$L_x = yp_z - zp_y = -i\hbar \left(y\frac{\partial}{\partial z} - z\frac{\partial}{\partial y} \right) \tag{27}$$

$$L_y = zp_x - xp_z = -i\hbar \left(z\frac{\partial}{\partial x} - x\frac{\partial}{\partial z} \right) \tag{28}$$

$$L_z = xp_y - yp_x = -i\hbar \left(x\frac{\partial}{\partial y} - y\frac{\partial}{\partial x} \right) \tag{29}$$

The equations thus far define the rigid rotor in a Cartesian coordinate system. We now convert these equations into spherical polar coordinates as shown in Figure 24.
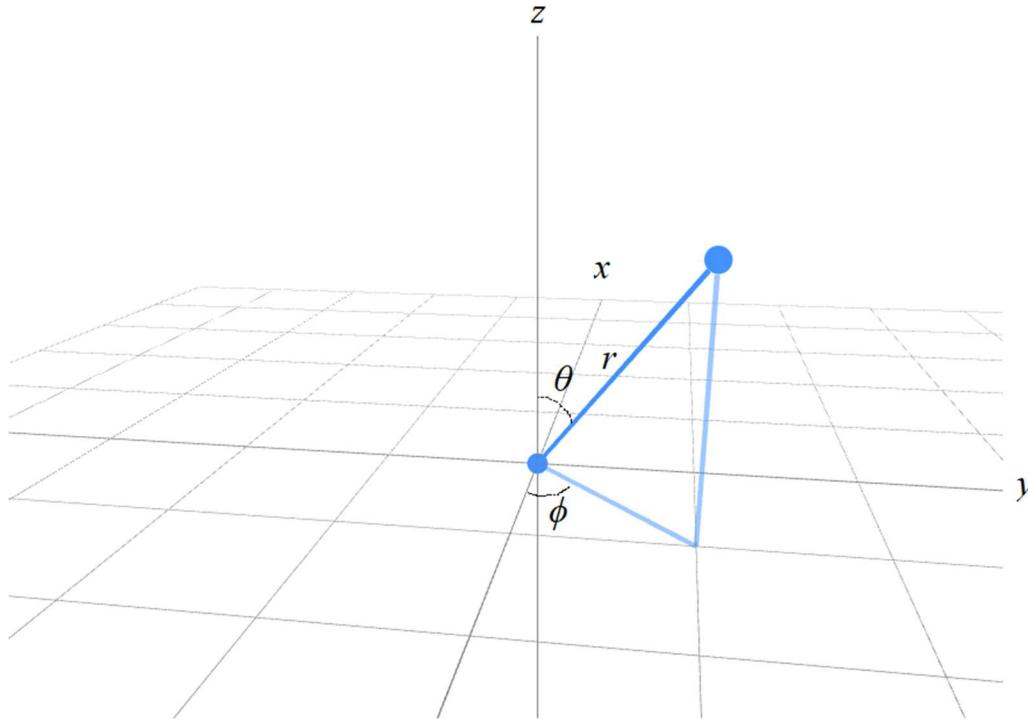
Figure 24 - Coordinate system with length, *r*, to visualize the conversion to spherical polar coordinates. This graph was made using the Math3D online website.

The reason we do this conversion is because that rotational motion is more conveniently studied in this form. The relations of Cartesian coordinates to spherical polar coordinates are as follows:

$$x = r \sin \theta \cos \phi \qquad (30)$$

$$y = r \sin \theta \sin \phi \qquad (31)$$

$$z = r \cos \theta \qquad (32)$$

we also need:

$$\cos \theta = \frac{z}{\sqrt{x^2 + y^2 + z^2}} \qquad (33)$$

$$\tan \phi = \frac{y}{x} \qquad (34)$$

40

Using these relations (Eq. 30, 31, 32, 33, 34), we can convert Cartesian coordinates into spherical polar coordinates. Note that the process of conversion is not a simple process of plugging in equations, but it is a long application of the chain rule and partial derivation.

$$L_x = -i\hbar \left(-\sin\phi \, \frac{\partial}{\partial\theta} - \cot\theta \cos\phi \, \frac{\partial}{\partial\phi}\right) \tag{35}$$

$$L_y = -i\hbar \left(\cos\phi \, \frac{\partial}{\partial\theta} - \cot\theta \sin\phi \, \frac{\partial}{\partial\phi}\right) \tag{36}$$

$$L_z = -i\hbar \, \frac{\partial}{\partial\phi} \tag{37}$$

And so, $\hat{L}^2 = L_x{}^2 + L_y{}^2 + L_z{}^2$ becomes:

$$\hat{L}^2 = -\hbar^2\left[\frac{1}{\sin\theta} \frac{\partial}{\partial\theta} \left(\sin\theta \, \frac{\partial}{\partial\theta}\right) + \frac{1}{\sin^2\theta} \frac{\partial^2}{\partial\phi^2}\right] \tag{38}$$

Now that we have our angular momentum operator, we can begin writing out Schrödinger's equation so we can see how everything begins to fall into place.

$$\hat{H}\psi = E\psi \tag{1}$$

Let's look the Hamiltonian operator for the rigid rotor:

$$\hat{H} = KE + \hat{V} \tag{39}$$

The Hamiltonian consists of kinetic energy, KE, and potential energy, $\hat{V}$. However, for the rigid rotor model, there is no potential energy because of the absence of any external forces. For this reason, the Hamiltonian operator for the rigid rotor model consists of only kinetic energy and is really written as:

$$\hat{H} = KE = \frac{L_x^2 + L_y^2 + L_z^2}{2\mu r^2} = \frac{\hat{L}^2}{2I} \tag{40}$$

Plugging in equation 38 to equation 40, we obtain our Hamiltonian operator, and it is expressed as:

$$\hat{H} = -\frac{\hbar^2}{2I}\left[\frac{1}{sin\theta}\frac{\partial}{\partial\theta}\left(sin\theta\,\frac{\partial}{\partial\theta}\right) + \frac{1}{sin^2\theta}\frac{\partial^2}{\partial\phi^2}\right] \tag{41}$$

The Schrödinger equation for the rigid rotor can be written out as:

$$-\frac{\hbar^2}{2I}\left[\frac{1}{sin\theta}\frac{\partial}{\partial\theta}\left(sin\theta\,\frac{\partial}{\partial\theta}\right) + \frac{1}{sin^2\theta}\frac{\partial^2}{\partial\phi^2}\right]\psi = E\psi \tag{42}$$

Before moving on to solving the equation, let's briefly discuss another way of getting the rigid rotor's Schrödinger's equation. Consider the 3D time-independent Schrödinger equation:

$$-\frac{\hbar^2}{2m}\left[\frac{\partial^2\psi}{\partial x^2} + \frac{\partial^2\psi}{\partial y^2} + \frac{\partial^2\psi}{\partial z^2}\right] + \hat{V}(x,y,z)\,\psi\,(x,y,z) = E\psi\,(x,y,z) \tag{43}$$

This can be simplified to a more compact form known as the Laplacian operator, ∇^2.

$$\nabla^2 = \left[\frac{\partial^2}{\partial x^2} + \frac{\partial^2}{\partial y^2} + \frac{\partial^2}{\partial z^2}\right] \tag{44}$$

The compact form can be written as:

$$-\frac{\hbar^2}{2m}\nabla^2\psi + \hat{V}(x,y,z)\,\psi\,(x,y,z) = E\psi\,(x,y,z) \tag{45}$$

Additionally, equation 45 has an adjustment for the rigid rotor model where the mass being observed is the reduced mass, μ.

$$-\frac{\hbar^2}{2\mu}\nabla^2\psi + \hat{V}(x,y,z)\,\psi\,(x,y,z) = E\psi\,(x,y,z) \tag{46}$$

Since we are still on the topic of the rigid rotor, we must convert the Laplacian operator from the Cartesian coordinate system into spherical polar coordinates just as we did for the angular momentum operators using equations 30, 31, 32, 33, and 34. This follows the same conditions as well. Figure 24 can be used as a reference. Through another long process, the resulting Laplacian operator in terms of spherical coordinates is:

$$\nabla^2 = \frac{1}{r^2}\frac{\partial}{\partial r}\left(r^2 \frac{\partial}{\partial r}\right) + \frac{1}{r^2 \sin\theta}\frac{\partial}{\partial \theta}\left(\sin\theta \frac{\partial}{\partial \theta}\right) + \frac{1}{r^2 \sin^2\theta}\frac{\partial^2}{\partial \phi^2} \tag{47}$$

Since the rigid rotor has a fixed distance, r, equation 46 simplifies to:

$$\nabla^2 = \frac{1}{r^2}\frac{\partial}{\partial r}\left(r^2 \frac{\partial}{\partial r}\right) + \frac{1}{r^2 \sin\theta}\frac{\partial}{\partial \theta}\left(\sin\theta \frac{\partial}{\partial \theta}\right) + \frac{1}{r^2 \sin^2\theta}\frac{\partial^2}{\partial \phi^2} \tag{48}$$

We can factor out $\frac{1}{r^2}$ from equation 48 and plug in the Laplacian operator to the adjusted compact Schrödinger equation, equation 46, that adjusted for the rigid rotor mass, μ. We must also remember that there is no potential energy affecting the rigid rotor, so that also can be canceled. Writing this out:

$$-\frac{\hbar^2}{2\mu}\frac{1}{r^2}\left[\frac{1}{\sin\theta}\frac{\partial}{\partial \theta}\left(\sin\theta \frac{\partial}{\partial \theta}\right) + \frac{1}{\sin^2\theta}\frac{\partial^2}{\partial \theta^2}\right]\psi + \widehat{V}(\theta,\phi)\,\psi\,(\theta,\phi) = E\psi\,(\theta,\phi) \tag{49}$$

We once again end up with equation 42 in terms of spherical polar coordinates:

$$-\frac{\hbar^2}{2I}\left[\frac{1}{\sin\theta}\frac{\partial}{\partial \theta}\left(\sin\theta \frac{\partial}{\partial \theta}\right) + \frac{1}{\sin^2\theta}\frac{\partial^2}{\partial \phi^2}\right]\psi = E\psi \tag{42}$$

We have established equation 42 to be the Schrödinger equation for the rigid rotor model. Now, the eigenfunction equations for ϕ and θ can be obtained. The solutions for this equation have been shown to be the spherical harmonics and are the simultaneous eigenfunctions of $\widehat{L}^2$ and L_z.

We will assign the z-component of angular momentum associated to L_z to be m. The total angular momentum associated with $\hat{L}^2$ will be referred to as l. Remember, this rigid rotor model is a 3D system that has been simplified to a 2D system because the motion of the rotor has been restricted to the surface of a sphere since distance r is fixed. For this reason, we can expect two quantum numbers m and l in our solutions. After some algebra and separation of variables to equation 42, we obtain two functions: one with only θ and another with only ϕ.

$$\frac{sin\theta}{\Theta(\theta)} \frac{\partial}{\partial\theta} \left(\sin\theta \frac{\partial\Theta}{\partial\theta}\right) + \beta \sin^2\theta = m^2 \tag{43}$$

$$\frac{1}{\Phi(\phi)} \frac{\partial^2\Phi}{\partial\phi^2} = -m^2 \tag{44}$$

Where beta, β,

$$\beta = \frac{2IE}{\hbar^2} \tag{45}$$

and m^2 is a constant. equation 44 only has constant coefficients so its relatively easy to solve. The solutions are:

$$\Phi(\phi) = A_m e^{im\phi} \text{ and } \Phi(\phi) = A_{-m} e^{-im\phi} \tag{46}$$

The value of A_m can be found by requiring $\Phi_m(\phi)$ to be normalized. After solving equation 43, it turns out that β must follow the following condition[17]:

$$\beta = l(l+1) \quad l = 0, 1, 2, \ldots$$

Substituting this condition back into equation 45, we get:

$$l(l+1) = \frac{2IE}{\hbar^2} \tag{47}$$

Rearranging for energy, E, and setting $\frac{\hbar^2}{2I} = B$, we get

$$E_l = \frac{\hbar^2}{2I} l (l + 1) = B l (l + 1) \quad l = 0, 1, 2, \dots \tag{48}$$

Where B is the rotational constant for our diatomic molecule. The energy is $2l + 1$-fold degenerate with fixed l and $m = -l, -l +1$, and l. For a state $Y_l^m (\theta,\phi)$, the magnitude of the angular momentum is:

$$|\vec{L}| = \sqrt{l(l + 1)}\ \hbar \tag{49}$$

and in Figure 25, the z-axis is projected as:

$$L_z = m\hbar \tag{50}$$
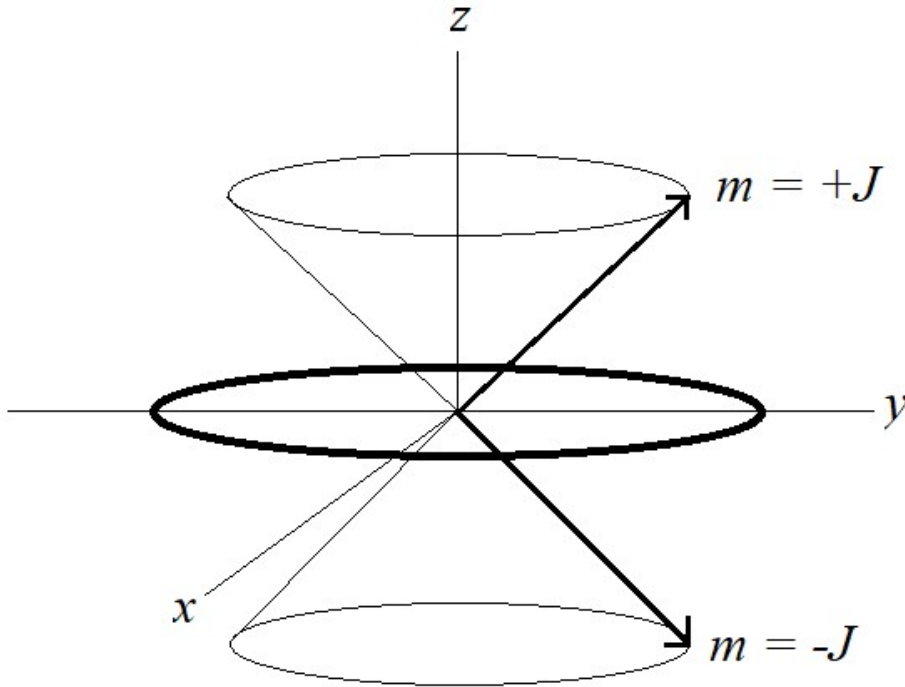
Figure 25 - Representation of degeneracy where m = +J, -J have the same energy. The circle on the x,y plane is also equivalent in energy.

The Schrödinger equation for our rigid rotor model shown in equation 42 gives the simultaneous eigenfunctions of $\hat{L}^2$ and L_z, denoted as $Y_l^m (\theta,\phi)$, through the following equation:

$$\hat{H} Y_l^m (\theta,\phi) = \frac{\hbar^2 l (l + 1)}{2I} Y_l^m (\theta,\phi) \qquad l = 0, 1, 2, \ldots \tag{51}$$

The specific normalized simultaneous eigenfunctions for $\hat{L}^2$ and L_z are as follows:

$$\hat{L}^2 Y_l^m = \frac{\hbar}{i} \frac{\partial Y_l^m}{\partial \phi} = m\hbar Y_l^m \tag{52}$$

$$L_z Y_l^m = l (l + 1) \hbar^2 Y_l^m \tag{53}$$

We now re-write equation 48 in terms of a quantum number J, as is customary in spectroscopy, instead of l.

$$E_J = \frac{\hbar^2}{2I} J (J + 1) = B J (J + 1) \quad J = 0, 1, 2, \ldots \tag{54}$$

Expanding the reduced Planck's constant, $\hbar$, in terms of Planck's constant, h, we get:

$$E_J = \frac{h^2}{(2\pi)^2 2I} J (J + 1) = \frac{h^2}{8\pi^2 I} J (J + 1) \tag{55}$$

The allowed energies of the rigid rotor are given by equation 54. The selection rule for the rigid rotor states that transitions are only allowed from adjacent states with the same amount of angular momentum along z. In other words, $\Delta J = \pm 1$ and $\Delta m = 0$. Using Bohr's frequency condition, $\Delta E = h \, \nu_{obs}$, and solving for frequency (ν_{obs}) we get:

$$\nu_{obs} = \frac{\Delta E}{h} \tag{56}$$

Where ΔE is written as:

$$\Delta E = E_{J+1} - E_J = \frac{h^2}{4\pi^2 I} \left(J + 1 \right) \quad J = 0,\ 1,\ 2,\ ... \tag{57}$$

Plugging into v_{obs} we get:

$$v_{obs} = \frac{h}{4\pi^2 I} \left(J + 1 \right) \quad J = 0,\ 1,\ 2,\ ... \tag{58}$$

With this, we begin to obtain frequencies at which the molecule is undergoing rotational

transitions. We can begin to visualize the rotational transitions of the rigid rotor and calculated

energy of the molecule as shown in Figure 26. In microwave spectroscopy, we write equation 54

as:

$$B = \frac{h}{8\pi^2 I} \tag{59}$$

Which is the rotational constant B in terms of frequency, Hertz (Hz).
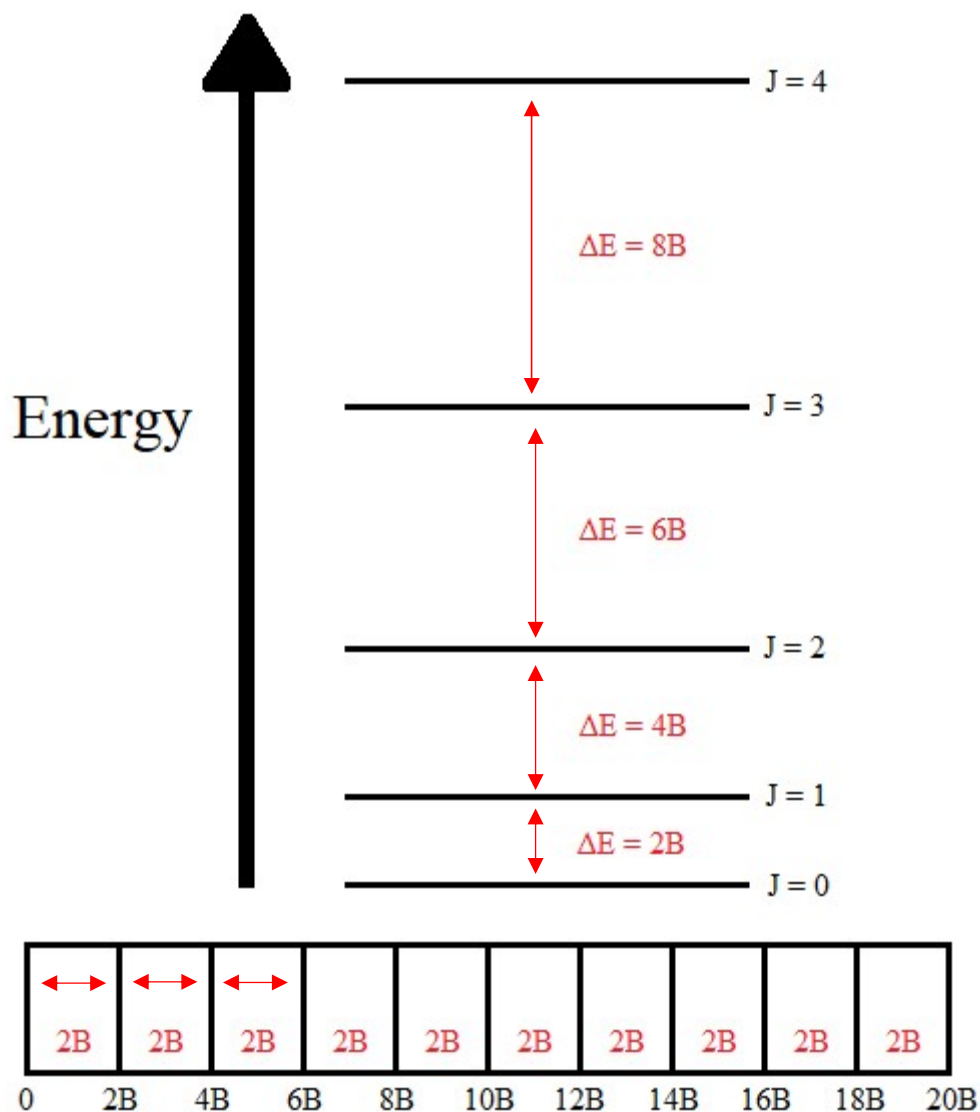
Figure 26 - The rotational energy levels and the allowed spectral lines of the rigid rotor model.

We can see in Figure 26 that the rotational energy between each transition has a difference of 2B for the rigid rotor model. The selection rules for the rigid rotor model state that $\Delta J = \pm 1$. This means the molecule cannot undergo a rotational transition from J = 0 directly to J = 2 or J = 3. A transition must go from J = 0 to J = 1, J = 1 to J = 0 or J = 2, etc.

The rigid rotor model can also be applied to linear molecules. The only difference to consider is that there are now multiple masses which affects the moment of inertia of the molecule.
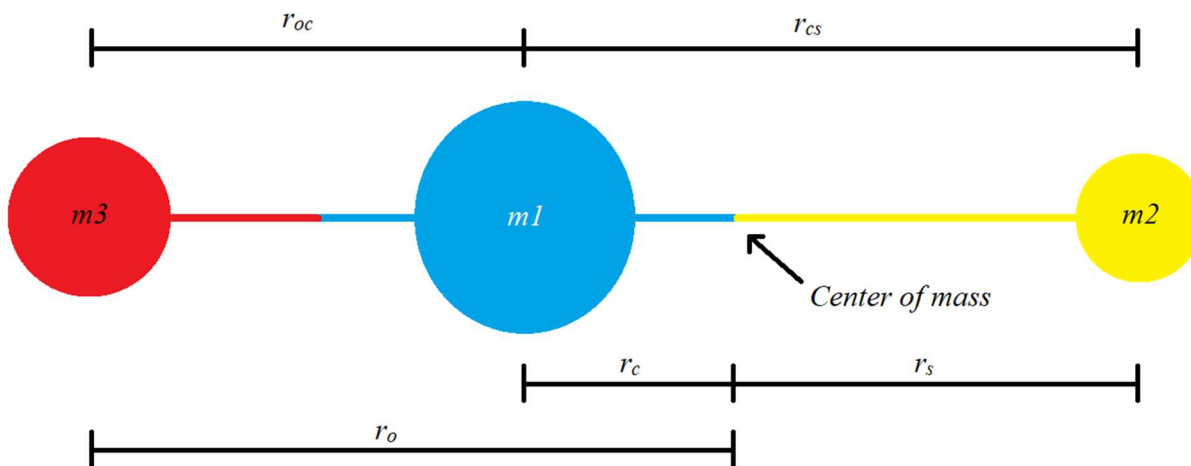
Figure 27 - Representation of carbonyl oxysulfide (OCS). There are 3 masses, m_1, m_2, and m_3. There are also 3 radii in respect to the center of mass r_o, r_c, and r_s.

The new moment of inertia for the linear molecule can be calculated as follows:

$$I_e = \sum_{j=1}^{n} m_j r_{ej}^2 \tag{60}$$

This expression can be explained as the sum of squared distances from a mass to an axis passing through the center of mass, r_{ej}. The rigid rotor model can be applied to linear molecules such as carbonyl oxysulfide (OCS), hydrogen cyanide (HCN), and thiocyanate (SCN⁻). Diatomic molecules and linear molecules can both be theoretically treated as a rigid rotor model for the sake of simplicity. Experimentally, as these molecules spin and undergo rotational transitions, they will also vibrate due to zero-point energy, such that the various interatomic distances will not be fixed. This motion is associated with a spectral effect called centrifugal distortion, which will be discussed in more detail in *Section 3.7*.

We can ease our minds for a moment as we discuss spherical top molecules. This category of molecules cannot absorb electromagnetic radiation because these molecules are too highly symmetric to have a permanent dipole moment[17]. For this reason, they cannot be observed in microwave spectroscopy. The moment of inertia for spherical tops is equal on every axis as listed on Table 2: $I_a = I_b = I_c$.

I_c

I_a

I_b
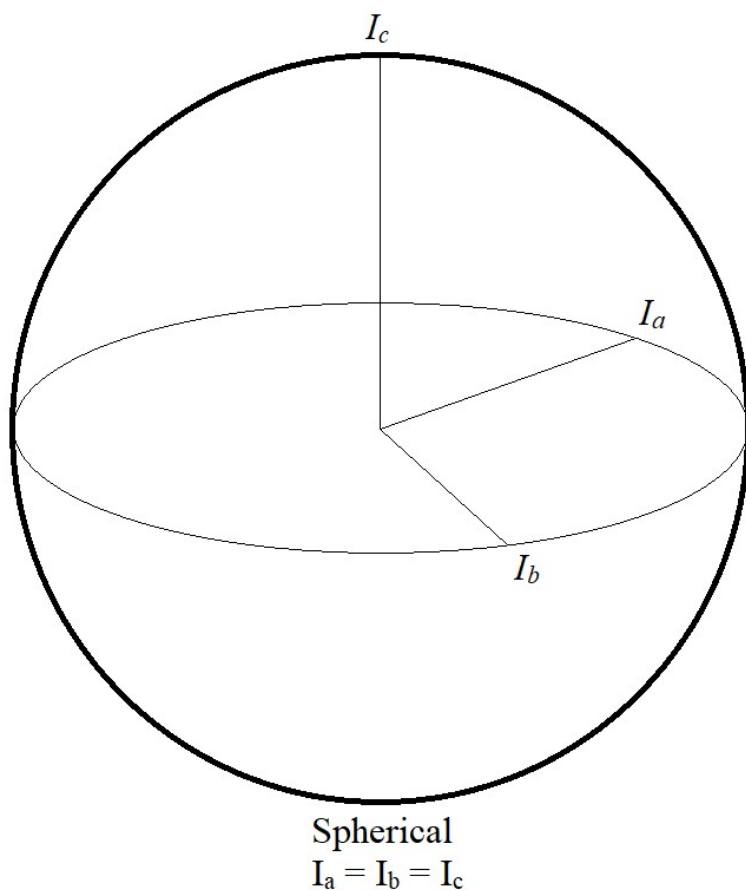
Spherical
$I_a = I_b = I_c$

Figure 28 - Spherical top model where all moments of inertia are equal, therefore, the molecule has no dipole moment and is not observed spectroscopically.

Examples of spherical top molecules are methane (CH_4), sulfur hexafluoride (SF_6), and borane (BH_3). The fact that these molecules are not able to be studied in microwave spectroscopy does not mean they cannot be studied at all; they can be observed using Raman spectroscopy.

However, their lack of a dipole moment prevents them from being studied in pure rotational spectroscopy.

Symmetric top molecules have two moment of inertia that are equal, and one shape-determining moment of inertia. In the following figure, Figure 29, the two types of tops are shown as oblate and prolate molecules.

Oblate
$I_c > I_a = I_b$
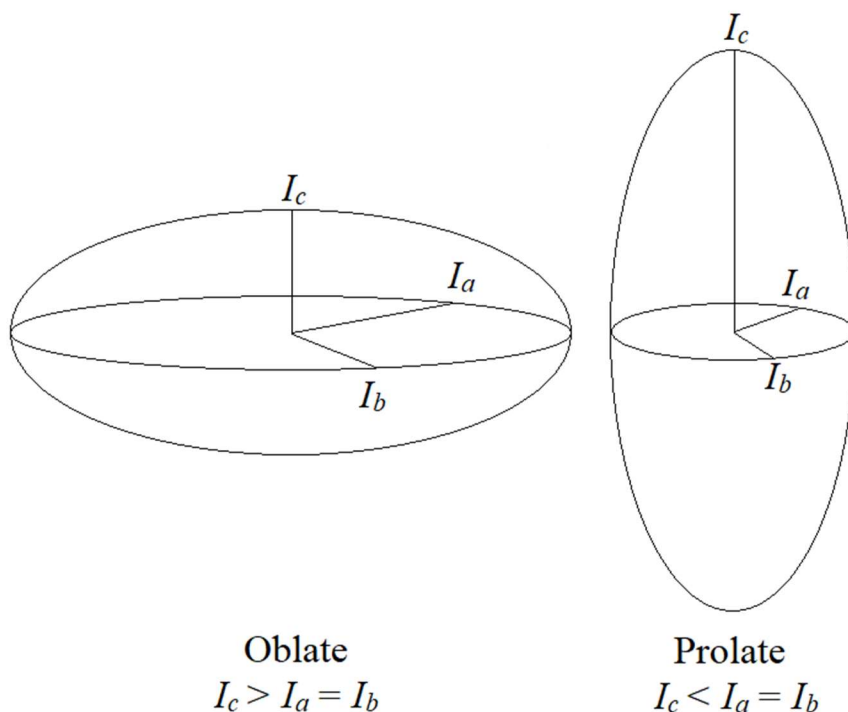
Prolate
$I_c < I_a = I_b$

Figure 29 - The two types of symmetric tops: oblate (Ex. NH_3) and prolate (Ex. CH_3Cl) models.

The shape of the top is implicit in the moment of inertia at the I_c axis. Because moment of inertia is defined as the resistance of a body to other forces, greater inertia means greater resistance to rotation around that corresponding axis and generally corresponds to a more extended system relative to that axis. For example, in the oblate top, the c axis is associated with

the largest moment of inertia. That is why the top appears to be in the shape of a football, whereas the prolate top has the least resistance to motion around c and looks like an egg.

To solve for the energies and rotational constants of a symmetric top, let's consider equation 54 from the rigid rotor model. Since we now have two moments of inertia that are different, the energy equation must be expanded to include them both. The solution to the Schrödinger for a symmetric top molecule gives the energy levels similarly to equation 54. However, now we must add another quantum number, K, that is the projection of the total angular momentum on the symmetric axis. The equation for the energy levels of a prolate symmetric top where $I_c < I_a = I_b$ is as follows[19, 20]:

$$E_{J,K} = \frac{h^2}{8\pi^2 I_B} J(J+1) + (\frac{h^2}{8\pi^2 A} - \frac{h^2}{8\pi^2 I_B}) K^2 \tag{61}$$

Which can be simplified to:

$$\frac{E_{J,K}}{hc} = B J(J+1) + (A - B) K^2 \tag{62}$$

This equation gives the rotational constants where $B = A$, and $A = B < C$. The rotational constants are equal to:

$$C = \frac{\hbar^2}{2hI_C} \tag{63}$$

$$A = B = \frac{\hbar^2}{2h_B} \tag{64}$$

For an oblate symmetric top where $I_c > I_a = I_b$:

$$\frac{E_{J,K}}{hc} = B J(J+1) + (C - B) K^2, K \leq J \tag{65}$$

The selection rules for the symmetric top state that K is always less than or equal to J since:

$\Delta J = 0, \pm1$ and $\Delta K = 0$ when $K \neq 0$

$\Delta J = \pm1$ and $\Delta K = 0$ when $K = 0$.

Lastly, there are $2J + 1$ possibilities of K for every J value. Like the diatomic and linear rotor models, the symmetric top category does not act as a rigid model experimentally. Therefore, we also have centrifugal distortion constants for the symmetric tops.

Asymmetric top molecules do not have any equivalent moments of inertia: $I_a \neq I_b \neq I_c$. They are the most common type of molecule and result in the most complex microwave spectra. The molecules studied in this thesis, chlorosulfonic acid and cyclohexanecarboxylic acid, are both asymmetric top molecules. There is no single set of equations which fully characterize all asymmetric molecules, but the selection rule $\Delta J = 0, \pm1$ still applies.

Section 3.5 – Rotational Constants

For the rigid rotor, we discussed the solution of the Schrödinger equation (Eq. 48) which showed that the energy of the diatomic molecule could be obtained from:

$$E_l = \frac{\hbar^2}{2I} J(J + J) = B J(J + 1) \quad J = 0, 1, 2, \ldots \tag{48}$$

Where B is the rotational constant of the rigid rotor. The value of the rotational constant is inversely proportional to the moment of inertia. If the moment of inertia $I_A > I_B > I_C$, then rotational constant $A < B < C$. We can relate rotational constants directly to the bond length of the diatomic molecule and solve for the distance[20]. We can do so by looking at equation 59:

$$B = \frac{h}{8\pi^2 I} \tag{59}$$

Substituting $I = \mu r^2$ into equation 59, we get:

$$B = \frac{h}{8\pi^2 \mu r^2} \tag{66}$$

Finally, we re-arrange the equation to solve for, r, which is the distance between the masses of our diatomic molecule[21]:

$$r = \sqrt{\frac{h}{8\pi^2 \mu B}} \tag{67}$$

Let's consider an example where the observed rotational constant B of carbon monoxide (CO) is 1.9313 cm^{-1}. Since the rotational constant is in wavenumbers, we must introduce c, the speed of light, into equation 67. The speed of light in cm/s is 2.998 x 10^{10}.

$$r = \sqrt{\frac{h}{8\pi^2 \mu B c}} \tag{68}$$

If our masses are given in atomic mass unites, the corresponding reduced mass in SI units is obtained by:

$$\mu = \frac{m1*m2}{m1+m2} \text{ X } \frac{10^{-3} kg \ mol^{-1}}{6.022 x 10^{23} mol^{-1}} \tag{69}$$

and is calculated to be 1.139 x 10^{-26} kg. Everything in equation 68 is known, and what's left is to plug in all numbers. Doing so we get:

$$r = 1.128 \text{ x } 10^{-10} \text{ m} = 112.8 \text{ pm}$$

which is the bond length of carbon monoxide[22]. It is important to remember that this bond length can be calculated from the observed rotational constant and the reduced mass of the molecule being observed. The concept is similarly applied to symmetric top molecules which have two distinct moments of inertia.

Section 3.6 – Dipole Moments

Another value used to characterize molecules is their dipole moment. An electric dipole occurs whenever charges are inhomogeneously distributed in space. The net electric dipole of a molecule cannot be zero if it is to be observed spectroscopically. The dipole moments of a molecular system are vectors and can also be represented in an axis system and can be written as:

$$\mu = \sum_i^n q_i r_i \tag{70}$$

where q is the charge and r is the vector representing its position.
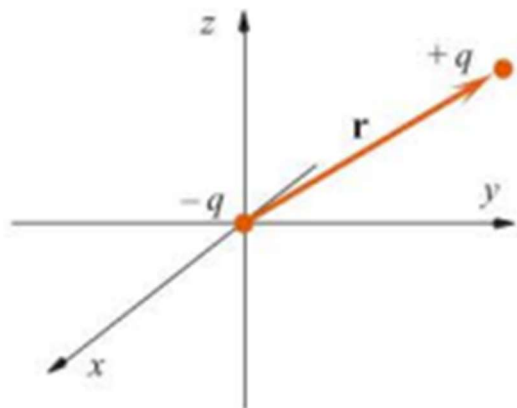
Figure 30 - A representation of a dipole moment with two-point charges, $-q$ and $+q$, separated by distance r[23].

To account for dipole moments along each principal axis, we have μ_a, μ_b, and μ_c. These constants are given in units of debyes defined as 1×10^{-18} statcoulomb-centimeter (statC·cm). In rotational spectroscopy, the type of transitions that a molecule will undergo are well represented by the dipole moments. For example, in the case of water, the following constants have been calculated[24, 25].

Table 5 - Rotational constants (A, B, C) and dipole moments (μ_a, μ_b, μ_c) of water.

H$_2$O (Water) Rotational Values	
A (GHz)	807.951
B (GHz)	436.212
C (GHz)	283.273
μ_a (debye)	0
μ_b (debye)	-1.859
μ_c (debye)	0

Figure 31 - Image of a water molecule.

This information can lead us to the conclusion that only *b*-type transitions will be present in the microwave spectrum of H$_2$O (water). The intensities of the peaks in a spectrum are stronger for which ever transitions have a stronger dipole moment.

Section 3.7 – Centrifugal Distortion

In *Section 3.4*, we discussed the rigid rotor which had a fixed distance during its rotation. The rigid rotor is a theoretical model in which we restrict the distance between molecules to a certain value as it's rotation. In reality, the distance is not fixed. As a molecule undergoes rotational transitions and the *J* values increase, the bond distance, *r*, fluctuates. The bond can stretch or compress slightly and in increased intensity as the energy of the transitions increase. This change in length is known as centrifugal distortion. Centrifugal distortion is part of the Hamiltonian operator for diatomic and linear molecules, symmetric, and asymmetric molecules. Adding the centrifugal distortion correction variable, $\hat{H}_{CD}$, to the overall Hamiltonian operator of the rigid rotor now gives us the non-rigid rotor model. The Hamiltonian is written as:

$$\hat{H} = \hat{H}_{KE} + \hat{H}_{PE} + \hat{H}_{CD} \qquad (71)$$

The number of centrifugal distortion constants increases as the molecule categories get more complex. Here we discuss the centrifugal distortion constants of the non-rigid rotor, i.e., diatomic and linear molecules. For the non-rigid rotor, the distance *r* is no longer fixed and can stretch as the molecule rotates more energetically. The stretching and compressing motions of a molecule is called centrifugal distortion and will be denoted as, $\bar{D}$ or $\bar{D}_J$ for the non-rigid rotor.
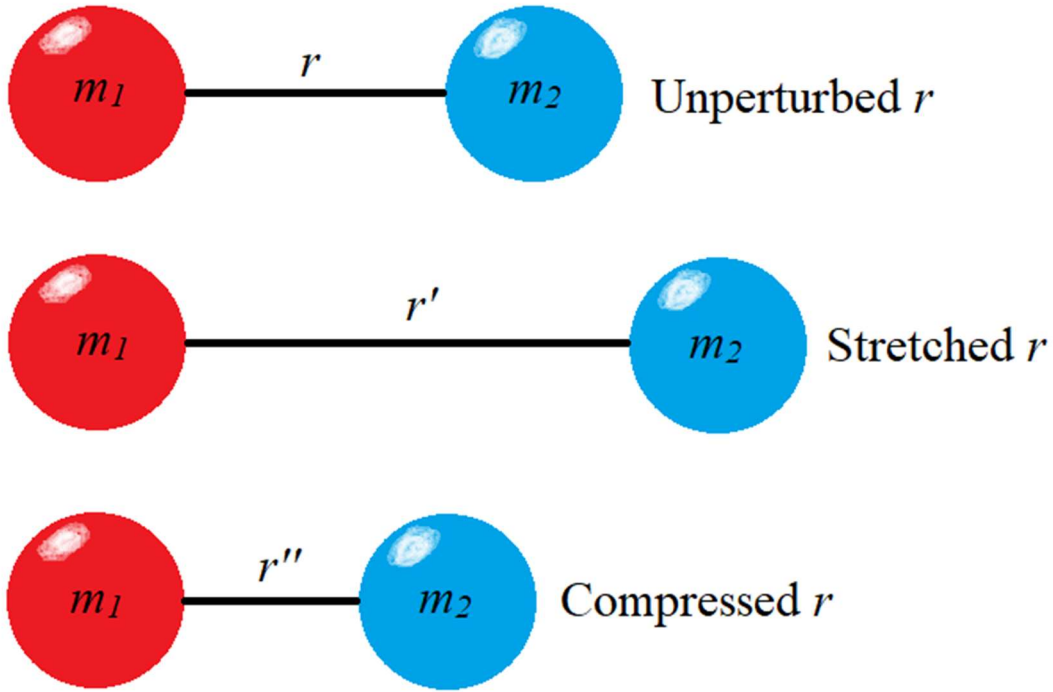
Figure 32 - Depiction of centrifugal distortion including compressing and stressing motions of *r*.

Through a similar process of derivation as for the rigid rotor, the wave equation is set up

for the non-rigid rotor and the energy values are shown by the following equation:

$$E_J = \frac{h^2}{8\pi^2 I} J(J+1) - \frac{h^4}{32\pi^4 I^2 r^2 k} J^2(J+1)^2 \tag{72}$$

Where the centrifugal distortion constant, $\bar{D}_J$, can be written as:

$$\bar{D}_J = \frac{h^4}{32\pi^4 I^2 r^2 k} \tag{73}$$

Where k is the force constant of the molecule. The centrifugal distortion constant is another

constant dependent on the angular momentum quantum number J. The centrifugal distortion

constant is directly proportional to the rotational constant B and can also be solved for with the

following equation[26]:

$$\bar{D}_J = \frac{4B^3}{\omega^2} \tag{74}$$

Where w is the harmonic vibrational frequency and is denoted as:

$$\omega = \frac{1}{2\pi} \sqrt{\frac{k}{\mu}} \tag{75}$$

The small correction of a molecule's centrifugal distortion affects the rotational spectrum by causing the spectral lines to be increasingly closer to each other. We can begin to make this observation just by looking at equation 72. The centrifugal distortion correction is subtracted from the rotational constant making the difference of the quantized energy levels smaller as the value of J increases.
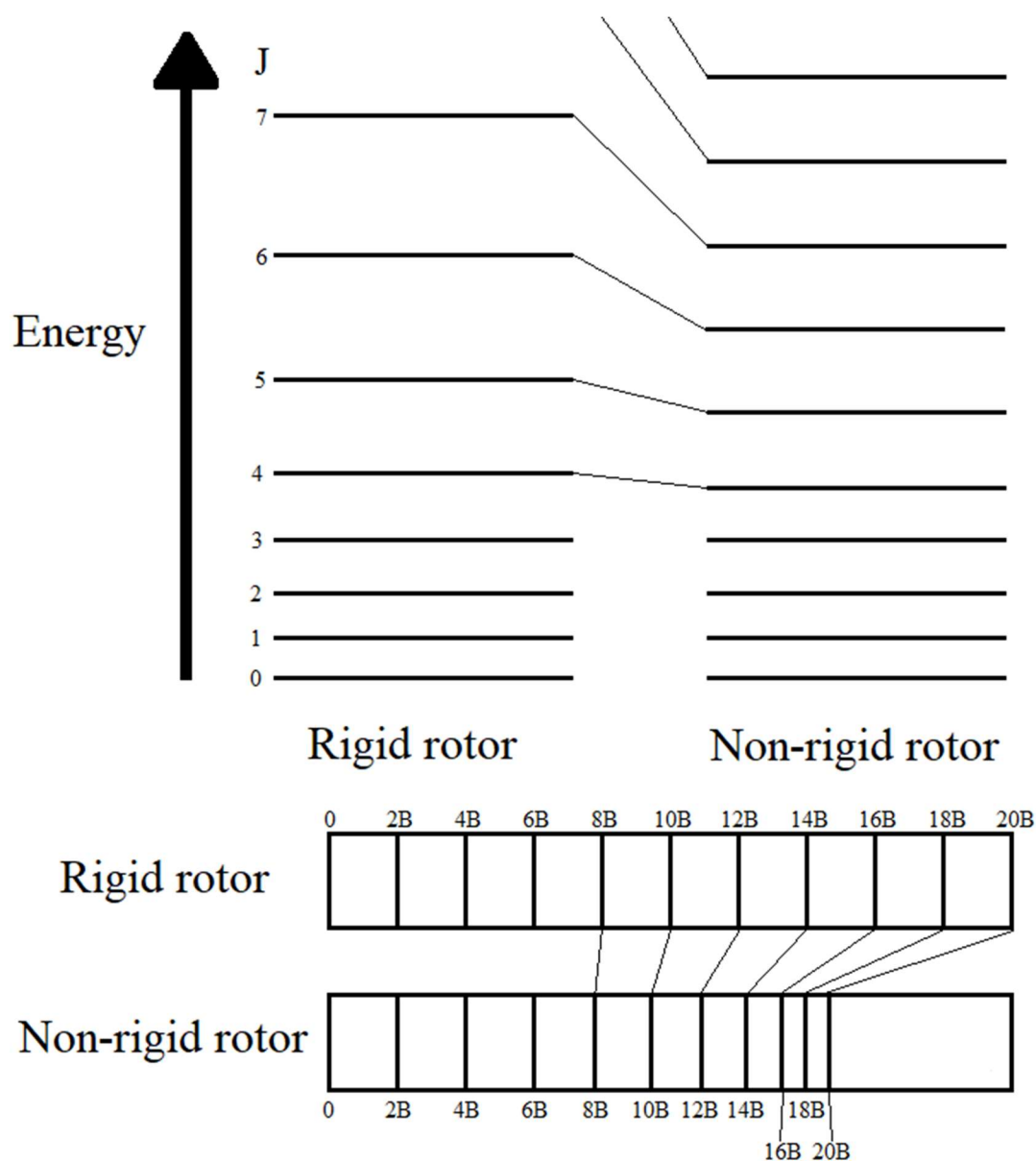
Figure 33 - Centrifugal distortion causes the increasing energy levels to get closer together, thus affecting the spectra in the same manner.

Looking at Figure 33, we compare the rotational energy levels of the rigid rotor model with the non-rigid rotor model which takes centrifugal distortion into consideration. In the non-rigid rotor model, the molecular bond stretches more as rotational energy increases. This leads to an increase in the moment of inertia, I, as we have seen that the moment of inertia is inversely proportional to the rotational constant B. This leads in turn to a decrease in rotational energy, as

well as a shift to a lower transition frequency relative to the rigid rotor model. Centrifugal distortion does not only affect diatomic and linear molecules, but symmetric and asymmetric molecules as well. As the degrees of freedom in a molecule increase, however, there are more variables to consider. For an asymmetric top, there are 3 centrifugal distortion constants denoted as $\bar{D}_J$, $\bar{D}_K$, and $\bar{D}_{JK}$. The equation is as follows:

$$E_{J,K} = B\,J\,(\,J + 1\,) + (\,A - B\,)\,K^2 - \bar{D}_J\,J^2\,(J + 1)^2 - \bar{D}_{JK}\,J\,(J + 1)^2\,K^2 - \bar{D}_K\,K^4 \qquad (76)$$

The selection rules are the same as previously mentioned where:

$\Delta J = 0, \pm 1$ and $\Delta K = 0$ when $K \neq 0$

$\Delta J = \pm 1$ and $\Delta K = 0$ when $K = 0$

The centrifugal distortion constants for asymmetric tops must be solved for each individual system as there are no specific patterns for solving the corrections.

Section 3.8 – Hyperfine Constants

There is an additional set of rotational constants to consider for chlorosulfonic acid. They are known as nuclear quadrupole coupling constants, or hyperfine constants, which numerically describe the electric field gradient induced by the chlorine nucleus. This effect is included in the Hamiltonian of a molecule that has an atom with a nuclear spin greater than or equal to 1, such as chlorine and iodine whose nuclear spins are $\frac{3}{2}$ and $\frac{5}{2}$, respectively[27]. It is important to include the effect of hyperfine interactions because they can cause peak splitting and shifting in the spacing of a spectrum[28]. The general Hamiltonian operator for chlorosulfonic acid can be written as:

$$\hat{H} = \hat{H}_{KE} + \hat{H}_{PE} + \hat{H}_{CD} + \hat{H}_Q \qquad (77)$$

where $\hat{H}_Q$ is the nuclear quadrupole moment, and it considers the interaction of electron spins with the nuclear spin also known as hyperfine interactions[29]. As an example, we can consider a non-rigid rotor model which can also be treated as a linear model. The nuclear quadrupole energy for a linear molecule with a single coupling nucleus is given by:

$$H_Q = -\chi\, Y\,(J, I, F) \tag{78}$$

Where chi (χ) is the nuclear quadrupole coupling constant.

$$\chi = eQq \tag{79}$$

e is the elementary charge of an electron; Q is a known variable that characterizes the coupling nucleus and $q = \dfrac{\partial^2 V}{\partial z^2}$ is the electric field gradient relative to the principal axis system where z is the molecular axis as mentioned in the rigid rotor model. $Y\,(J, I, F)$ is a function dependent on various quantum numbers, F and J, and the nuclear spin I. This function is written as:

$$Y\,(J, I, F) = \frac{\frac{3}{4}C(C+1) - I(I+1)J(J+1)}{2(2J-1)(2J+3)I(2I-1)} \tag{80}$$

and

$$C = F(F+1) - J(J+1) - I(I+1) \tag{81}$$

F is the new total angular moment defining the hyperfine states and includes the overall rotation, J, and the nuclear spin, I. Written as an equation:

$$F = J + I, J + I - 1,\ J + I - 2, J + I - 3\ldots \tag{82}$$

This concept is similarly applied to an asymmetric top molecule. The equation for the quadrupole energy of an asymmetric top is:

$$H_Q = \left(\frac{Y(J,I,F)}{J(J+1)} \right) \times \{ [\, 3\,(P_a^2) - J(J+1)\,]\, \chi_{aa} - \sigma\, [\, (P_a^2) - W(b_p)\,]\, \eta\, \chi_{aa} \} \tag{83}$$

Where (P_a^2) is the average P_z^2 in an asymmetric rotor basis. $\sigma = -\dfrac{1}{b_p}$ and $W(b_p)$ is Wang's

reduced energy. The asymmetry parameter:

$$\eta = \frac{\chi_{bb} - \chi_{cc}}{\chi_{aa}} \tag{84}$$

shows the departure of the electric field gradient[30,31]. χ_{aa}, χ_{bb}, and χ_{cc} are calculated relative to

the principal axis system, $q_{aa} = \dfrac{\partial^2 V}{\partial a^2}$, $q_{bb} = \dfrac{\partial^2 V}{\partial b^2}$, and $q_{cc} = \dfrac{\partial^2 V}{\partial c^2}$[32]. *Ab initio* calculations for

chlorosulfonic acid yields numerical representations of the electric field gradient interaction with

the electric quadrupole moment of the nucleus[33] as χ_{aa}, χ_{bb}, and χ_{cc}.

CHAPTER IV

CYCLOHEXANECARBOXYLIC ACID (CHCA)

Section 4.1 – Introduction to CHCA

In Chapter 1, previous studies on cyclohexanecarboxaldehyde were discussed where the main structural conformers were *cis*, *trans*, and *gauche* structures. Those types of structures are also present in this *ab initio* study of cyclohexanecarboxylic acid (CHCA) but will be referred to in a different manner. Before we talk about the structures observed in CHCA, we will discuss some of the basics for structure nomenclature used in organic chemistry. It is known that the molecule, cyclohexane, will be stable in two conformers: chair and boat-twisted structures[1].

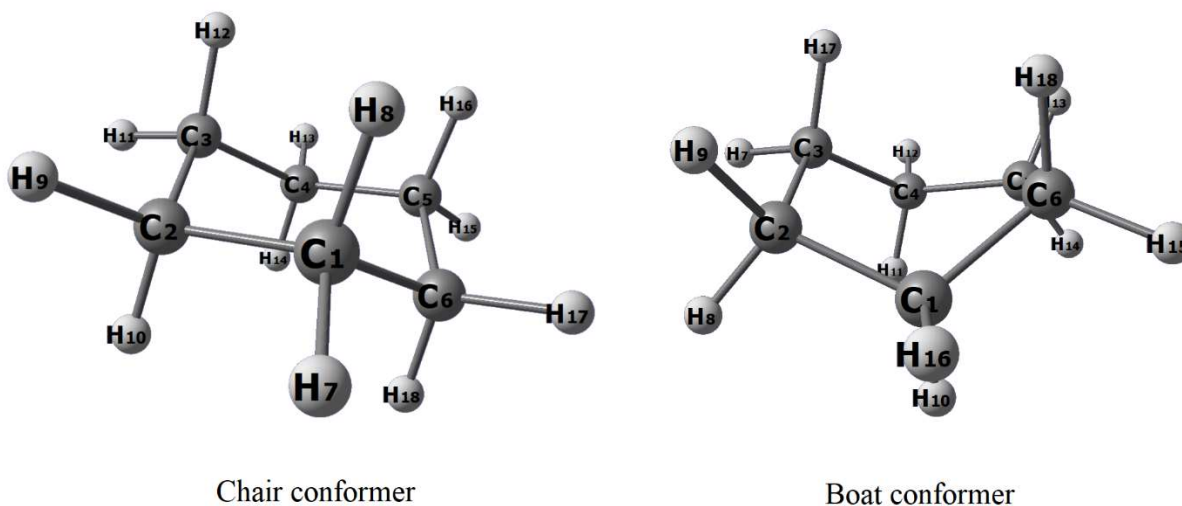Chair conformer   Boat conformer

Figure 34 - Chair and boat conformers of cyclohexane.

The chair conformer is more stable than the boat because the boat conformer has steric strain from the "flagpole" hydrogens and torsional strain from the adjacent carbon atoms. In addition to the structural conformers of cyclohexane, the carboxylic acid positions are also important when considering the stability of CHCA. The carboxylic acid functional group can be in either the equatorial or axial position of the ring.
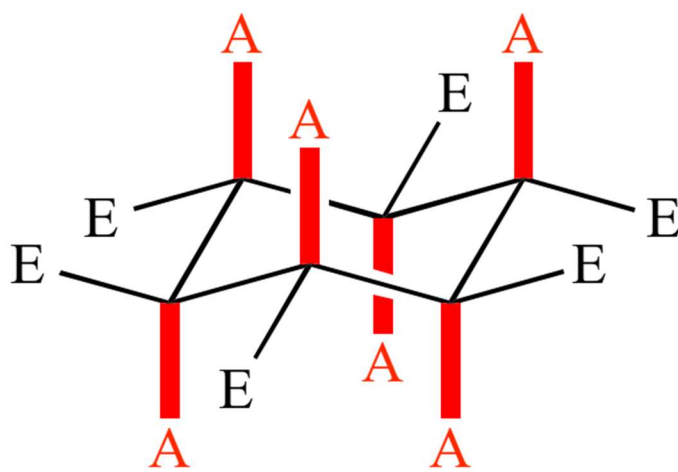

Figure 35 - Cyclohexane hydrogens labeled as axial (red) and (equatorial).

The same concept is applied to the boat conformer, which can have the carboxylic acid in the equatorial or axial position. Overall, we have four initial structures to consider in our quantum chemical calculations of CHCA: chair equatorial (CE), chair axial (CA), boat equatorial (BE), and boat axial (BA).
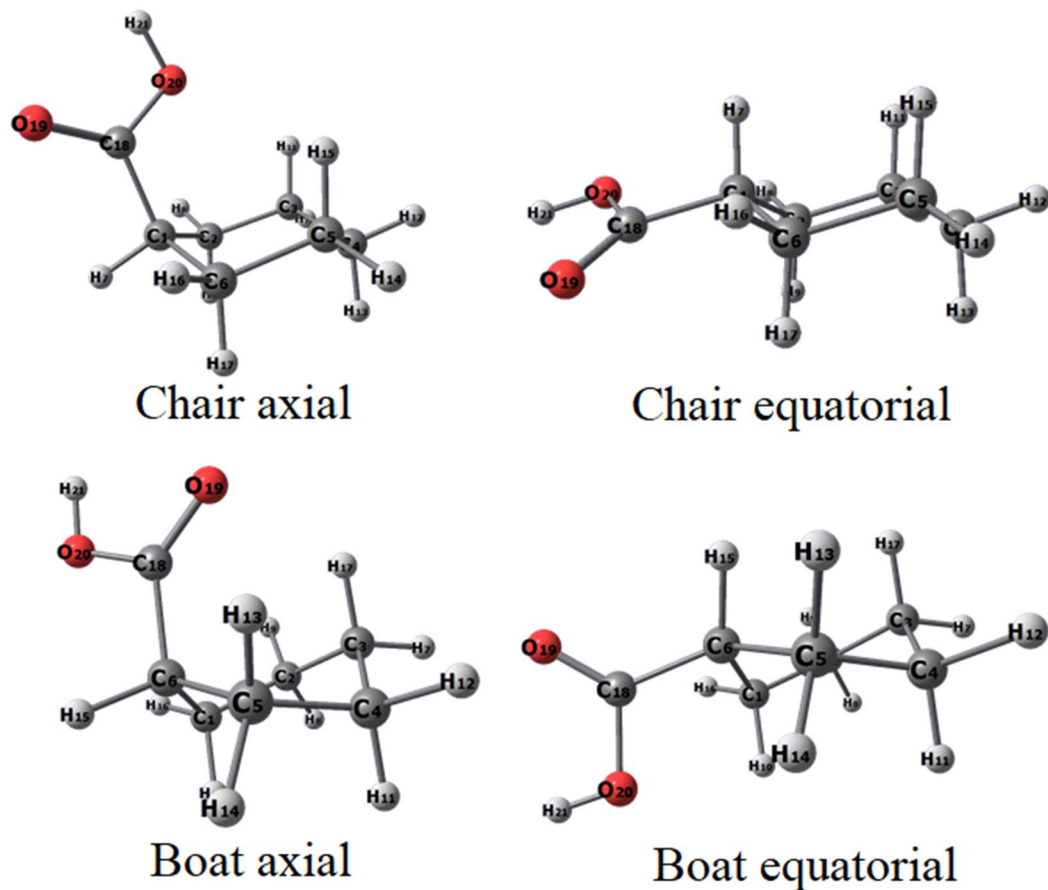
Figure 36 - The four initial structures of CHCA that will be studied.

This conformational analysis of cyclohexanecarboxylic acid is to study the relative energy of the molecule at different conformers. It is important to know this because the reactivity of the molecule is affected by the positioning of the carboxylic acid functional group and the structure of the cyclohexane.

Section 4.2 – Potential Energy Surface Scans

A potential energy surface (PES) scan performs a series of energy calculations at various structures of the molecule. In the PES scans performed using Gaussian 16, a specified dihedral angle is selected so that the molecule's energy levels at a certain structure will be approximated. The levels of theory used for PES scans are the same ones used in structure optimization, such as

DFT or MP2 methods and aug-cc-pVTZ basis set. These methods and basis sets can of course, vary. The potential energy scan is very useful for recognizing molecular structures by their relative energies with respect to local minima, global minima, and transition states. The structures shown by PES scans are not optimized but are excellent starting points for structure optimization[2].

A PES scan was done for each conformer shown in Figure 36. For all structures, the dihedral angle started at the carbon connecting the carboxylic acid and the cyclohexane, the carbon in the carboxyl functional group, the oxygen bonded to the hydrogen. The numbering of the atoms varies between the boat and chair conformers, but this only affects the labeling. With reference to Figure 36, the dihedral angle observed in the PES scan can be written as τC6, C1, C18, O19 for the chair axial and chair equatorial conformers. The dihedral angle for the boat axial and boat equatorial structures can be written as τC5, C6, C18, O19. We will begin discussing the PES scans for the boat structures. All four scans were done in 36 steps of 10 degrees (36 x 10 = 360 degrees).
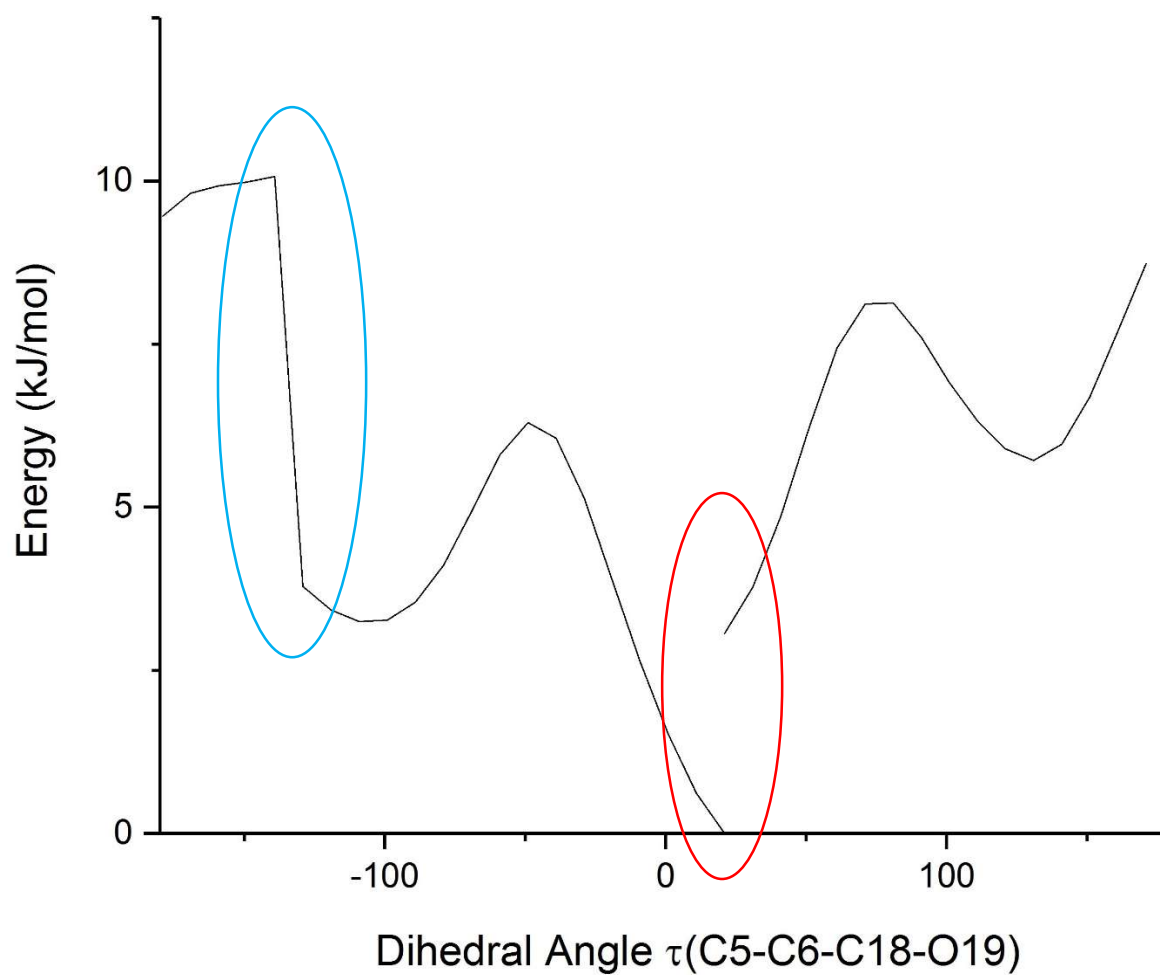
Figure 37 - PES scan for the CHCA boat axial conformer. Gap circled in blue is from structural rearrangement and gap circled in red is due to the rearranged structure ending at a lower energy than the initial structure.

Figure 37 shows the PES scan of the CHCA boat axial structure. The gaps in the graph were caused by an automatic structure rearrangement.
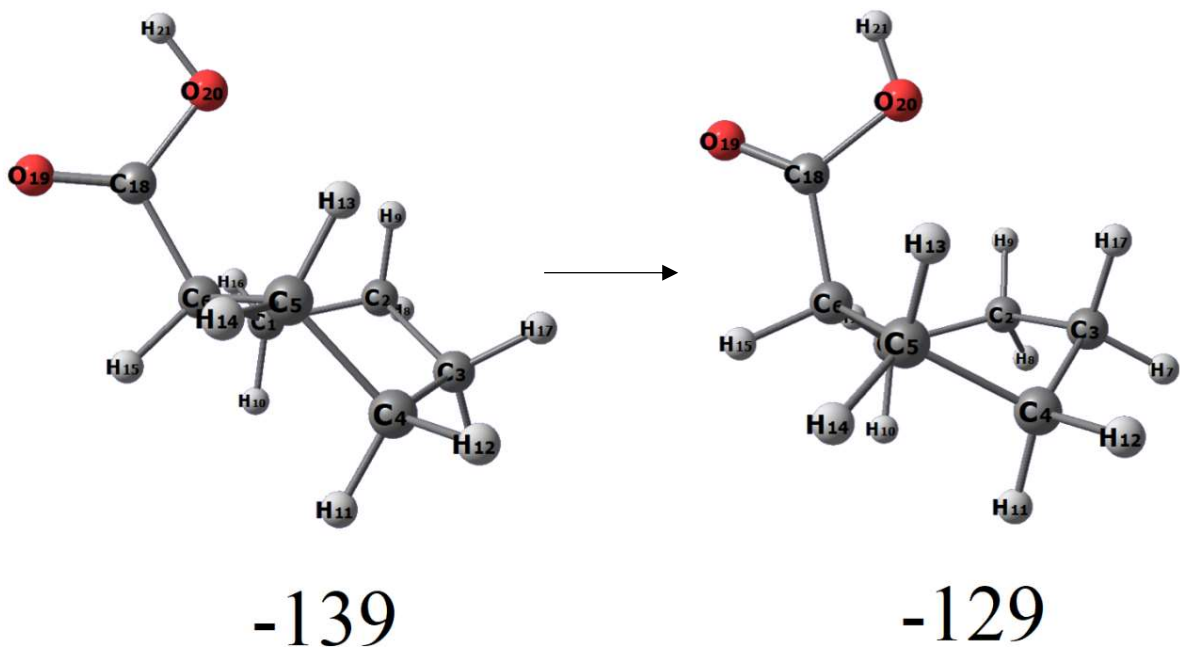
Figure 38 - CHCA boat axial structure rearrangement during the PES scan from -139° to -129°.

This rearrangement explains the gap circled in blue in Figure 37. The scan continued with the single point energy calculations with the structure shown at -129° which is a lower energy structure. The most interesting part about this rearrangement is that the CHCA boat axial structure changed to a boat-twist structure. The boat-twist structure is slightly lower in energy than the boat conformer, and it is likely that this shift occurred because the energy was too high for the CHCA boat axial conformer.
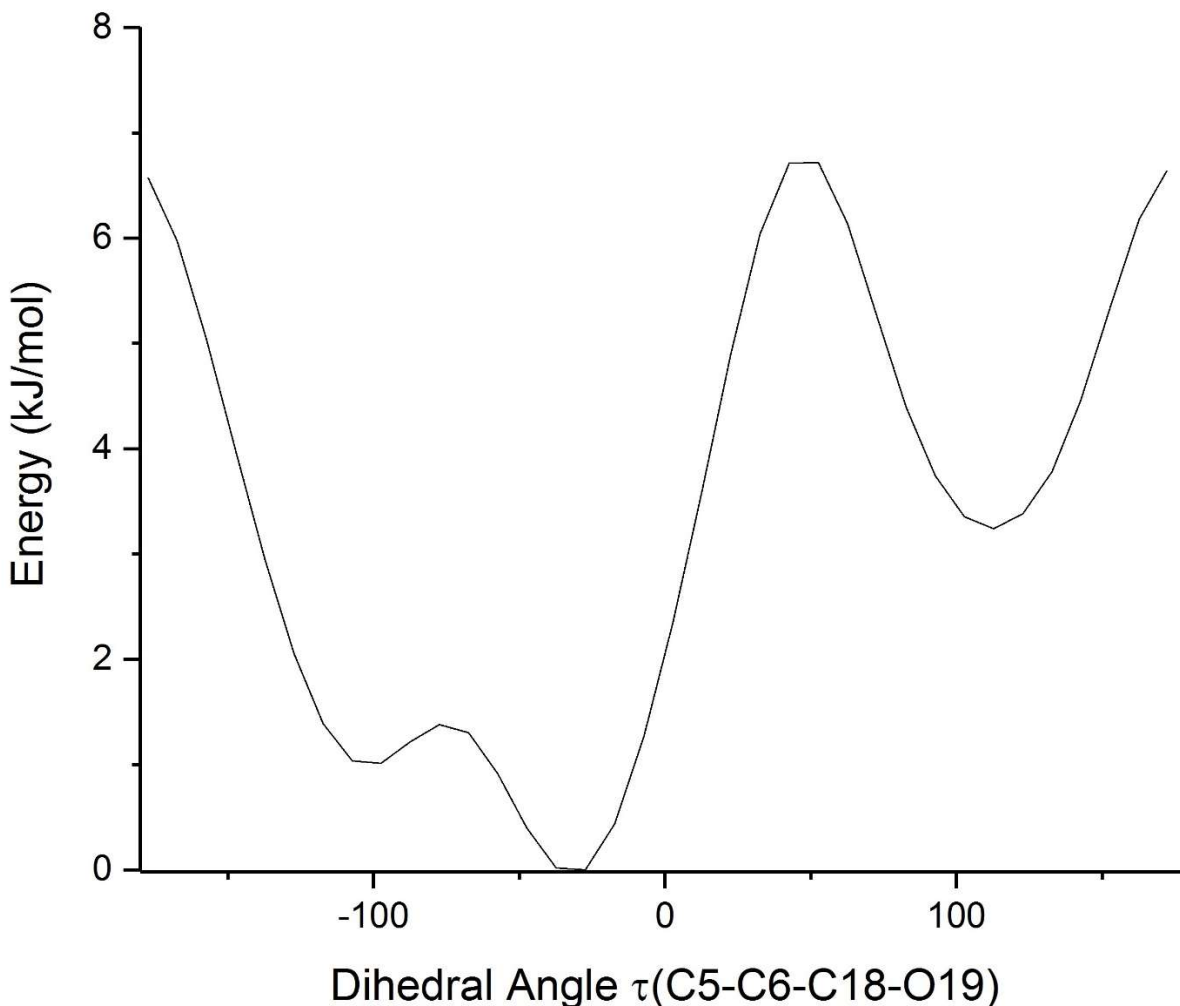
Figure 39 - PES scan for the CHCA boat equatorial conformer. The scan shows 1 local minimum at -97°, 1 global minimum at -27°, and 1 global at 112°.

The PES scan for the CHCA boat equatorial conformer gave more promising results where we were able to observe three conformational energy minima. These three structures were optimized using DFT and MP2 methods with aug-cc-pVTZ basis set. While they stable enough to have their structure optimized, we were not expecting the simulated peaks to appear experimentally under the supersonic expansion condition as the boat structure is still higher in energy than the chair structures.
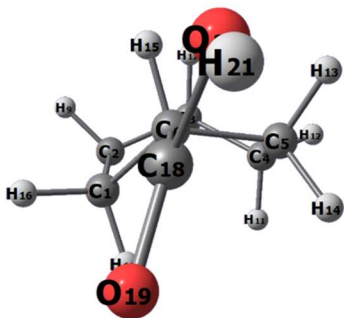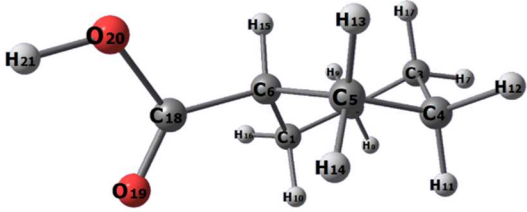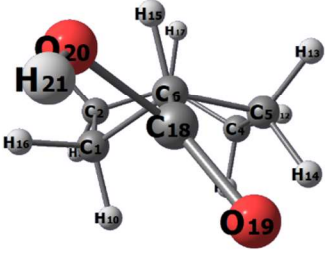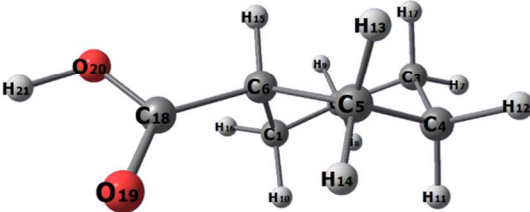
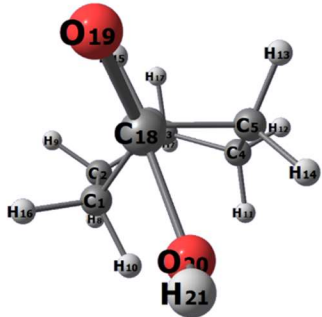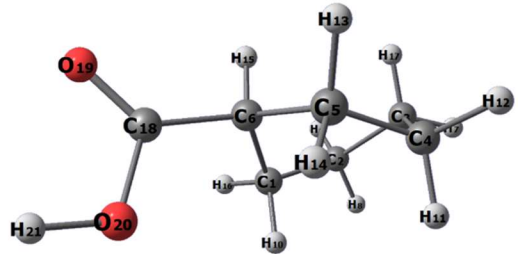| Front view	Side view	Degrees
		-97°
		-27°
		112°

Figure 40 - CHCA boat equatorial conformers shown from the front and side view at -97°, -27°, and 112°.

The boat equatorial structure is a twist-boat structure. This can be seen at the side view for -97° and -27°. The structure looks like a slanted hourglass ($\bar{\mathrm{X}}$). From the side view we can see C_6, C_5, and C_4 in a descending shape (like \) as well as C_3, C_2, and C_1 (like /). From the front view, we can see that it is still a boat-twist structure. The structure at 112° is more boat-like and it explains the increase in relative energy of that structure.
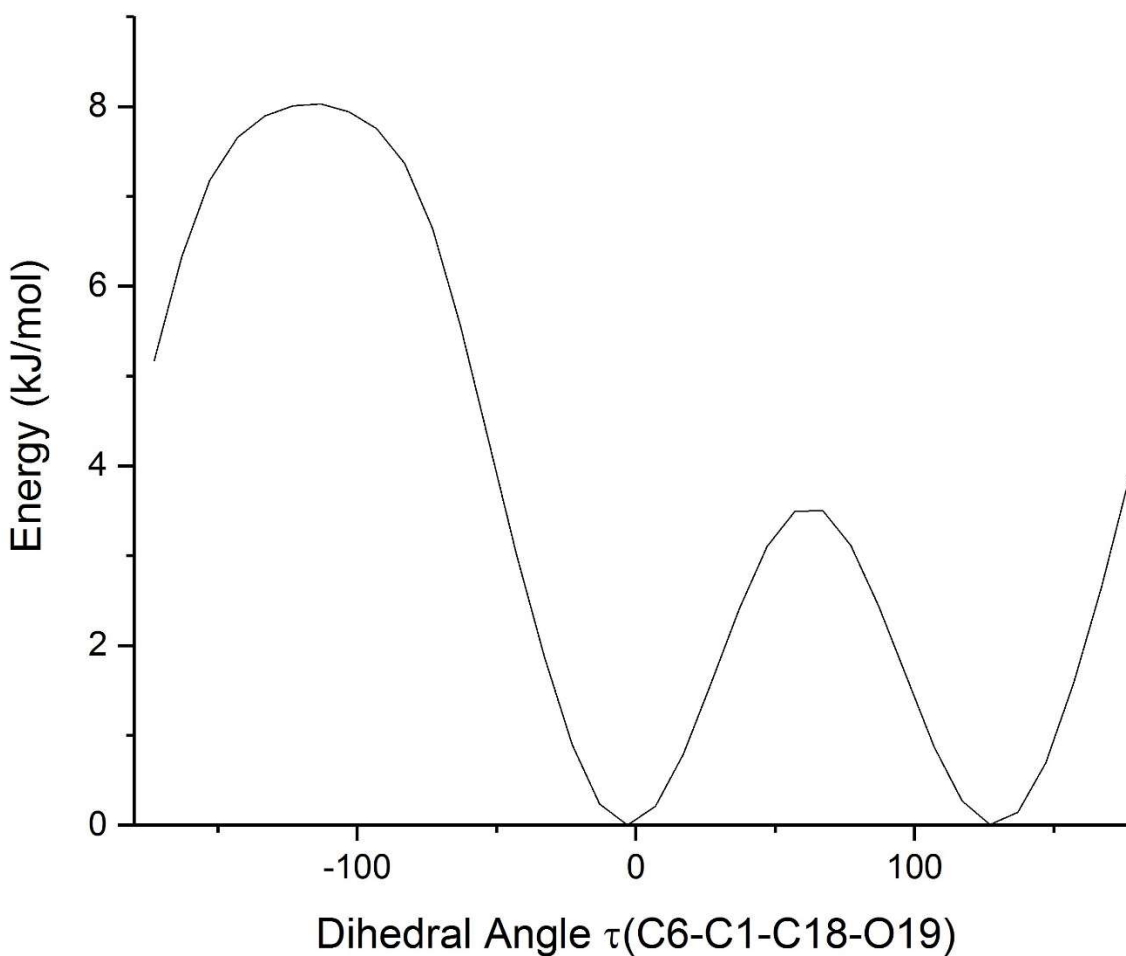
Figure 41 - PES scan for the CHCA chair axial conformer. The scan shows 2 minima at -3° and 127°.

The PES scan showed two possible conformers for the CHCA chair axial structure both

of which had nearly identical energy levels. The two structures are equivalent due to the

symmetry of the molecule. For this reason, the optimization of one of these structures will

provide the rotational values that represent both structures as they are mirror images of each

other and are nearly energetically identical. As mentioned before, the structure optimizations are

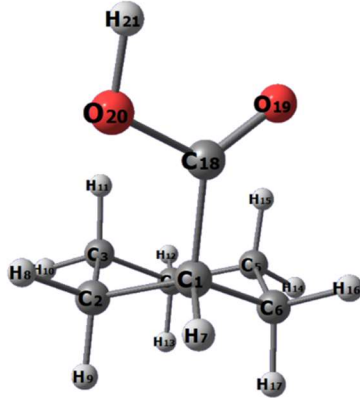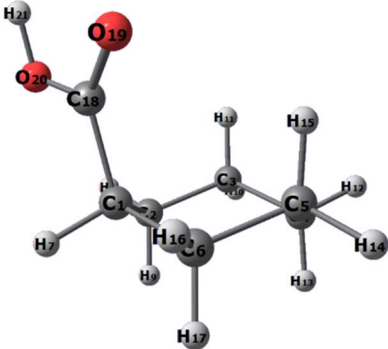done using DFT and MP2 methods with an aug-cc-pVTZ basis set.
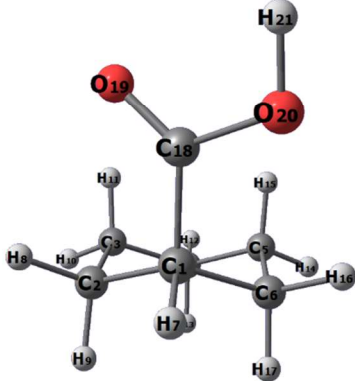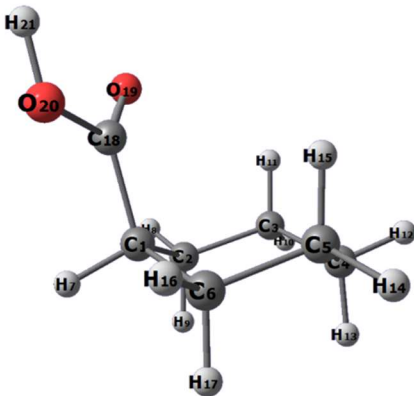
Figure 42 - CHCA chair axial conformers shown from the front and side view at -3° and 127°.
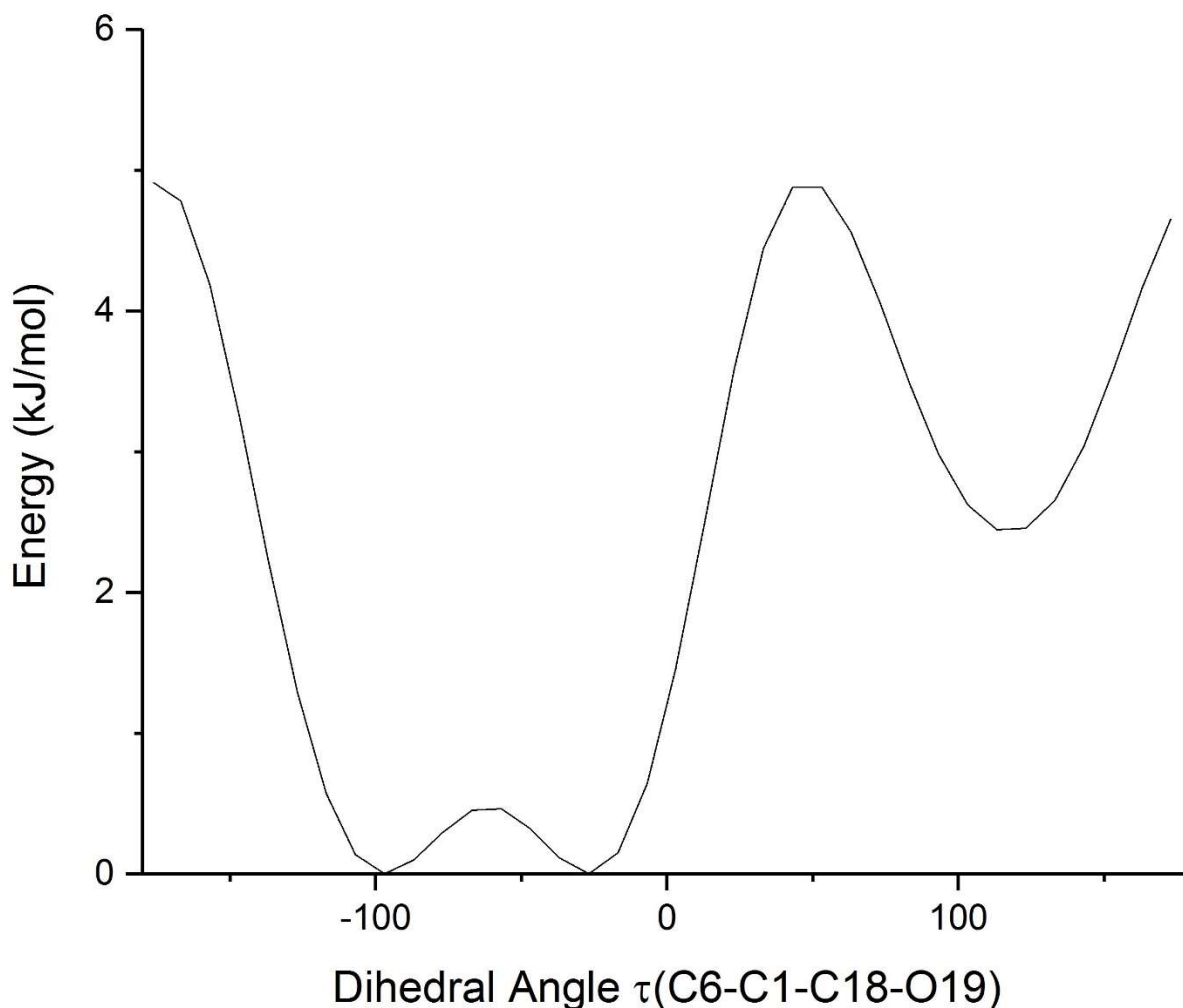
Figure 43 - PES scan for the CHCA chair equatorial conformer. The scan shows 2 minima at -97° and -27°. Additionally, there is 1 global minimum at 113°.

Like in the CHCA chair axial PES scan (Figure 41), there are two structures here in the

CHCA chair equatorial scan that are nearly identical in energy due to the symmetry of the

molecule. Thus, one structure optimization will be representative of those two minima. The local

minimum structure will also be optimized but is not expected to appear experimentally (at least

not in high population) due to being higher in energy. From the CHCA chair equatorial

conformer, we will be optimizing two structures.
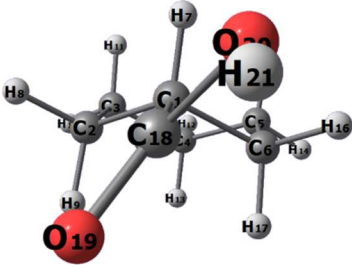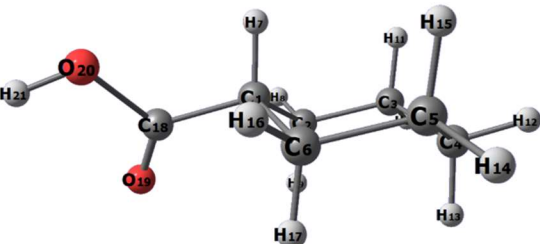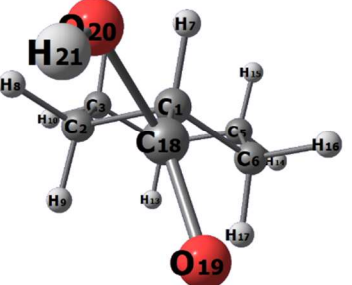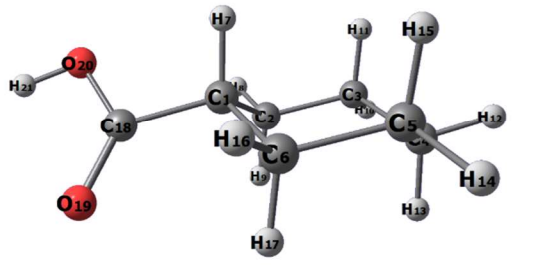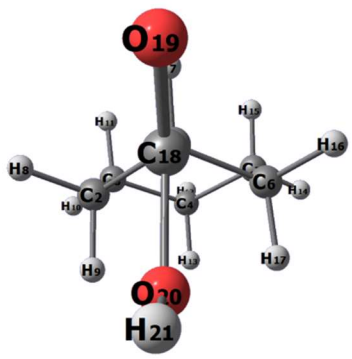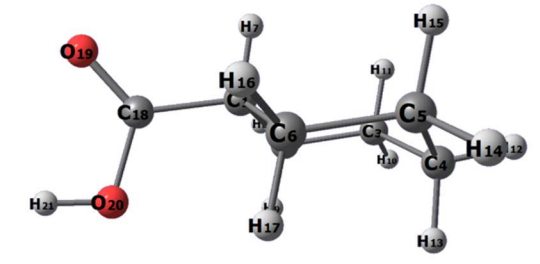
Front view	Side view	Degrees
		-97°
		-27°
		113°

Figure 44 - CHCA chair equatorial conformers shown from the front and side view at -97°, -27°, and 113°.

Section 4.3 – Geometry Optimizations

We discussed the relative energies of the chair and boat conformers of CHCA, and we know that the chair conformer is more stable than the boat conformer. For this reason, it is unlikely to obtain signals emitted by the boat conformer in the experimental spectrum under supersonic expansion condition because majority of the molecules are in the chair conformer due to stability. It is not impossible, but the signals would be very weak as there is a lower amount of

those molecules. There was a total of six conformers to be optimized according to *Section 4.2*.

Three conformers from CHCA boat equatorial, 1 conformer for CHCA chair axial, and 2

conformers for CHCA chair equatorial were optimized using Density Functional Theory

(B3LYP) and Second Order Møller–Plesset perturbation theory (MP2) with an augmented

correlation-consistent polarized valence triple-zeta (aug-cc-pVTZ) basis set.

For reference, the following abbreviations will be listed: cyclohexanecarboxylic acid

(CHCA), chair equatorial (CE), chair axial (CA), boat equatorial (BE), and boat axial (BA). *ΔD*

(kJ/mol) is the relative energy and *ΔD$_o$* (*kJ/mol*) is the relative energy with the ZeroPoint

(kJ/mol) corrected. **A**, **B** and **C** are the rotational constants. **μ$_a$**, **μ$_b$**, and **μ$_c$** are the dipole

moments.

Table 6 – Bond lengths of the chair equatorial conformer of cyclohexanecarboxylic acid.

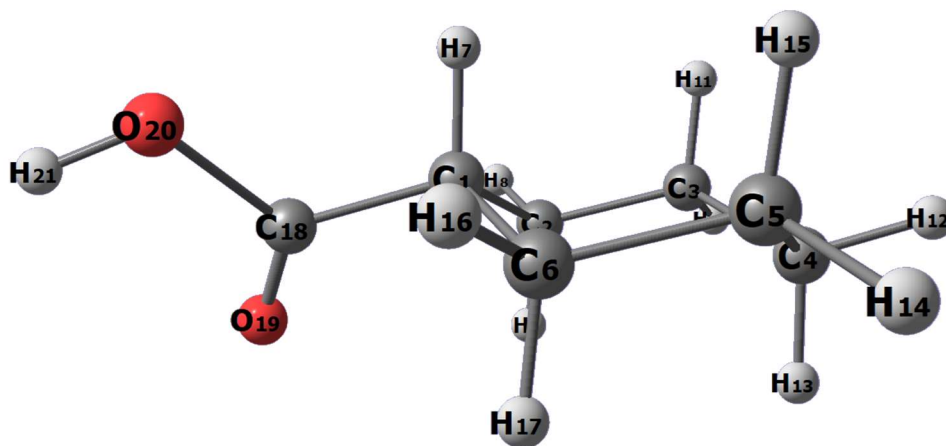| Parameter	Length	Parameter	Length
$r(C_1-H_7)$	1.094	$r(C_5-H_{14})$	1.092
$r(C_1-C_2)$	1.524	$r(C_5-H_{15})$	1.095
$r(C_2-H_8)$	1.092	$r(C_5-C_6)$	1.526
$r(C_2-H_9)$	1.093	$r(C_6-H_{16})$	1.091
$r(C_2-C_3)$	1.526	$r(C_6-H_{17})$	1.095
$r(C_3-H_{10})$	1.091	$r(C_6-C_1)$	1.538
$r(C_3-H_{11})$	1.095	$r(C_1-C_{18})$	1.502
$r(C_3-C_4)$	1.526	$r(C_{18}-O_{19})$	1.212
$r(C_4-H_{12})$	1.092	$r(C_{18}-O_{20})$	1.359
$r(C_4-H_{13})$	1.095	$r(O_{20}-H_{21})$	0.970
$r(C_4-C_5)$	1.526	-	-

Figure 45 – The chair equatorial conformer of cyclohexanecarboxylic acid.

Table 7 – Bond angles of the chair equatorial conformer of cyclohexanecarboxylic acid.

Parameter	Angle	Parameter	Angle	Parameter	Angle	Parameter	Angle
$H_7C_1C_2$	110.14	$H_{10}C_3C_4$	110.39	$H_{14}C_5H_{15}$	106.96	$C_6C_1H_7$	107.94
$C_1C_2C_3$	110.66	$H_{11}C_3C_4$	109.17	$H_{14}C_5C_6$	109.78	$C_{18}C_1C_2$	111.49
$C_1C_2H_8$	109.93	$C_3C_4C_5$	110.85	$H_{15}C_5C_6$	109.06	$C_6C_1H_7$	107.77
$C_1C_2H_9$	108.51	$C_3C_4H_{12}$	110.40	$C_5C_6C_1$	110.52	$C_1C_{18}O_{19}$	126.12
$H_8C_2H_9$	106.76	$C_3C_4H_{13}$	109.11	$C_5C_6H_{16}$	110.81	$C_1C_{18}O_{20}$	111.53
$H_8C_2C_3$	110.84	$H_{12}C_4H_{13}$	107.00	$C_5C_6H_{17}$	109.62	$O_{19}C_{18}O_{20}$	122.32
$H_9C_2C_3$	110.04	$H_{12}C_4C_5$	110.26	$H_{16}C_6C_1$	109.85	$C_{18}O_{20}H_{21}$	105.71
$C_2C_3C_4$	111.05	$H_{13}C_4C_5$	109.12	$H_{16}C_6H_{17}$	107.60	-	-
$C_2C_3H_{10}$	109.88	$C_4C_5C_6$	111.14	$H_{17}C_6C_1$	108.37	-	-
$C_2C_3H_{11}$	109.40	$C_4C_5H_{14}$	110.51	$C_6C_1C_{18}$	108.67	-	-
$H_{10}C_3H_{11}$	106.85	$C_4C_5H_{15}$	109.28	$C_6C_1C_2$	110.70	-	-

The structural parameters shown in Table 6 and 7 are of the lowest energy conformer CHCACE1 which is visualized in Figure 45. As the carboxylic acid functional group rotates in the PES scans, the atoms orientate themselves as needed.

Table 8 - Rotational values of the six CHCA conformers going from lowest to highest (left to right) energy. The values on this table were obtained using Density Functional Theory (B3LYP) with an aug-cc-pVTZ basis set. ΔD and ΔD_o are in units of kJ/mol.

Values	CHCACE1	CHCACE2	CHCACA	CHCABE1	CHCABE2	CHCABE3
ΔD	0	2.42	5.92	-	26.82	27.97
ΔD_o	0	2.69	6.21	-	26.78	28.3
A	3194.32	3200.88	2565.2	3149.08	3146.43	3158.84
B	1056.07	1027.07	1339.06	1072.48	1059.83	1034.84
C	899.42	936.23	1113.49	908.39	919.69	951.14
μ_a	1.07	1.74	0.456	1.10	1.17	1.67
μ_b	1.13	0.001	1.367	1.17	1.098	0.22
μ_c	0.94	1.31	0.76	0.82	0.95	1.38

Table 9 - Rotational values of the six CHCA conformers going from lowest to highest (left to right) energy. The values on this table were obtained using Second Order Møller–Plesset perturbation theory (MP2) with an aug-cc-pVTZ basis set. ΔD, ΔD$_o$, and the ZeroPoint energy are in units of kJ/mol.

Values	CHCACE1	CHCACE2	CHCACA	CHCABE1	CHCABE2	CHCABE3
$\varDelta D$	0	1.53	1.95	24.18	24.96	26.96
$\varDelta D_o$	0	1.89	2.09	24.17	25.27	27.25
A	3208.97	2526.91	3225.65	3160.82	3162.65	3180.78
B	1075.37	1403.27	1041.49	1081.94	1092.10	1050.66
C	911.16	1160.93	951.57	936.16	926.34	972.25
μ_a	0.99	0.42	1.65	1.10	1.05	1.57
μ_b	1.09	1.27	0.001	1.07	1.11	0.05
μ_c	0.83	0.65	1.22	0.83	0.69	1.31

Comparing Table 9 to Table 8, we can notice that CHCACA is lower in energy then CHCACE2 after the MP2 optimization. This change in order of is not surprising because the low energy conformer of CHCACA is very close in energy to the high energy conformer of CHCACE. The obtained rotational values were used to simulate a spectrum for each conformer. The observed experimental frequency for CHCA was from 5.5 GHz – 18.75 GHz.

Section 4.4 – Theoretical Spectra

The theoretical spectra are in the following order: CHCACE1, CHCACE2, CHCACA, CHCABE1, CHCABE2, and CHCABE3.
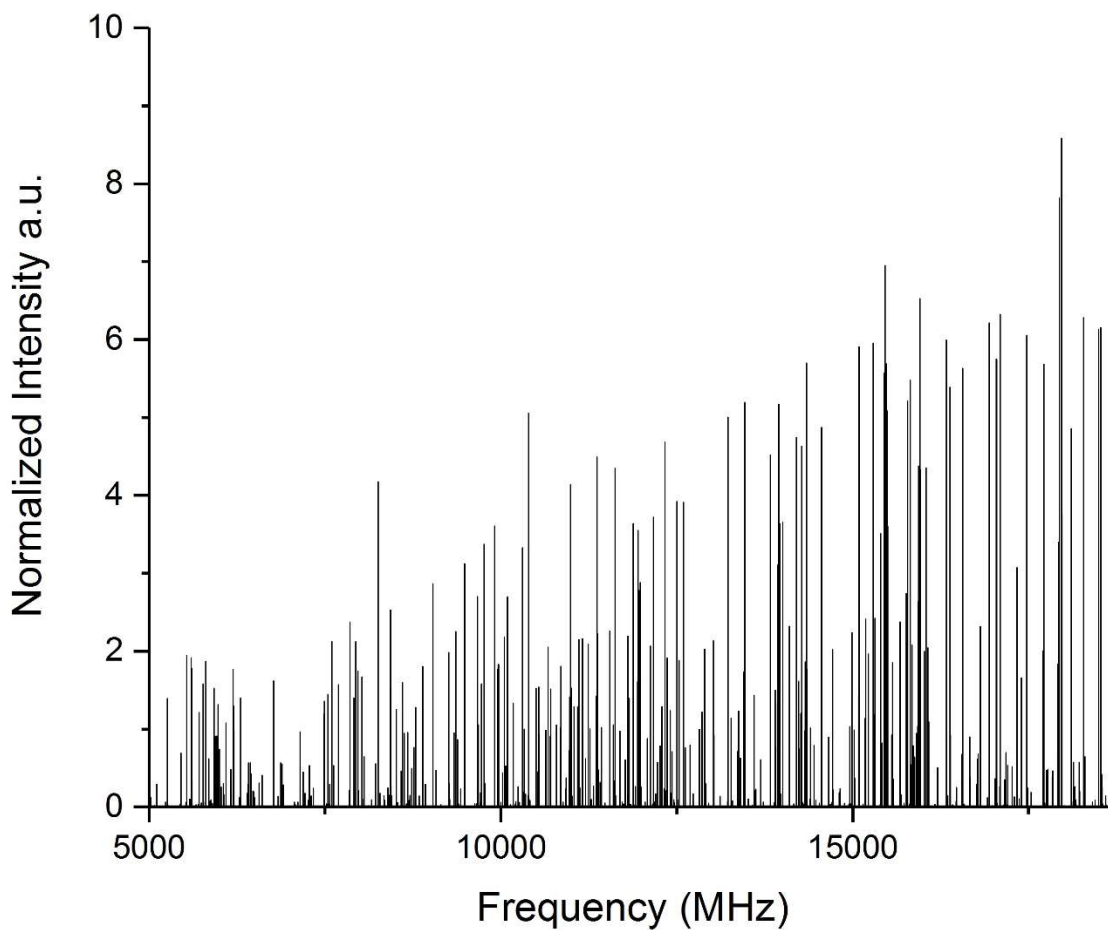
Figure 46 – Simulated spectrum of the lowest energy conformer, CHCACE1. Range is from 5 – 18.75 GHz.

The spectrum shown in Figure 46 is the one most likely to appear spectroscopically as CHCA will most likely be in this conformer as it is the lowest energy structure.
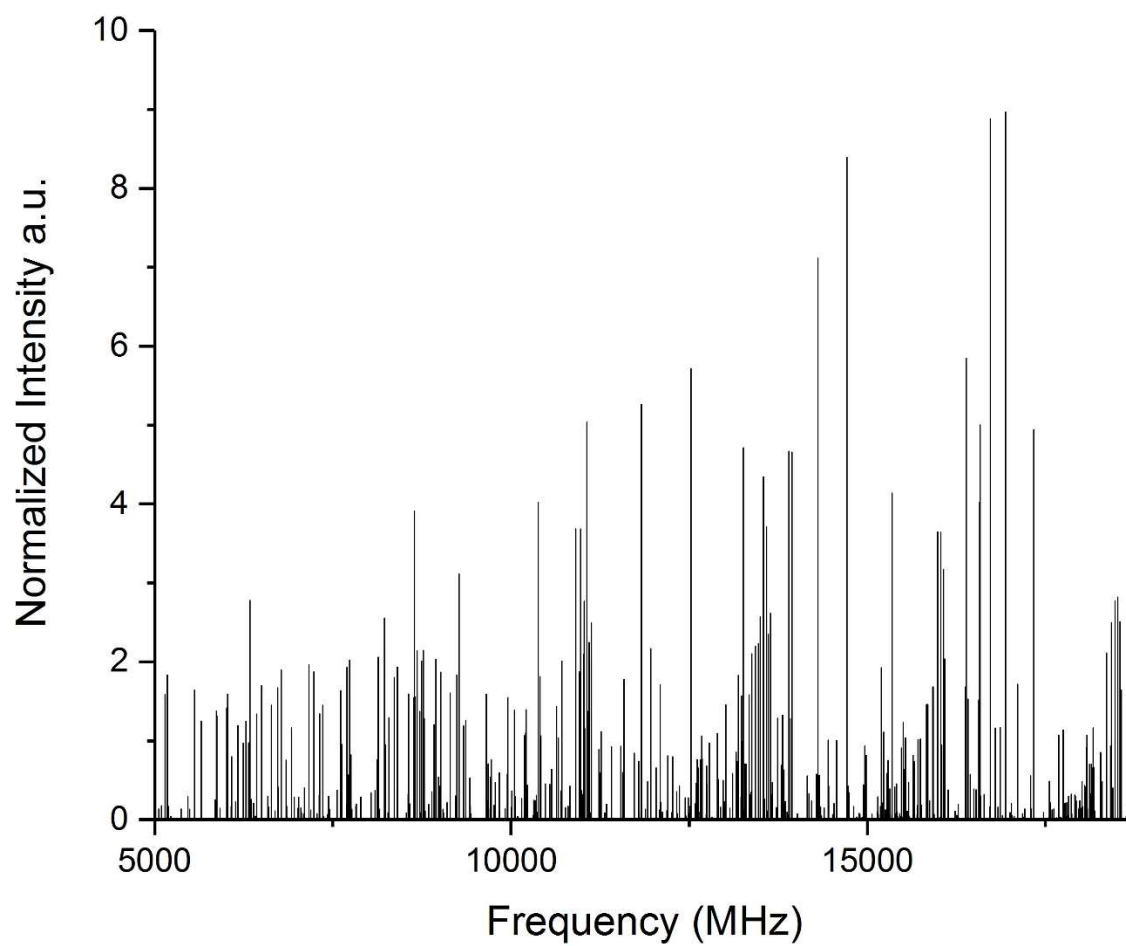
Figure 47 – Simulated spectrum of CHCACA. Range is from 5 – 18.75 GHz.
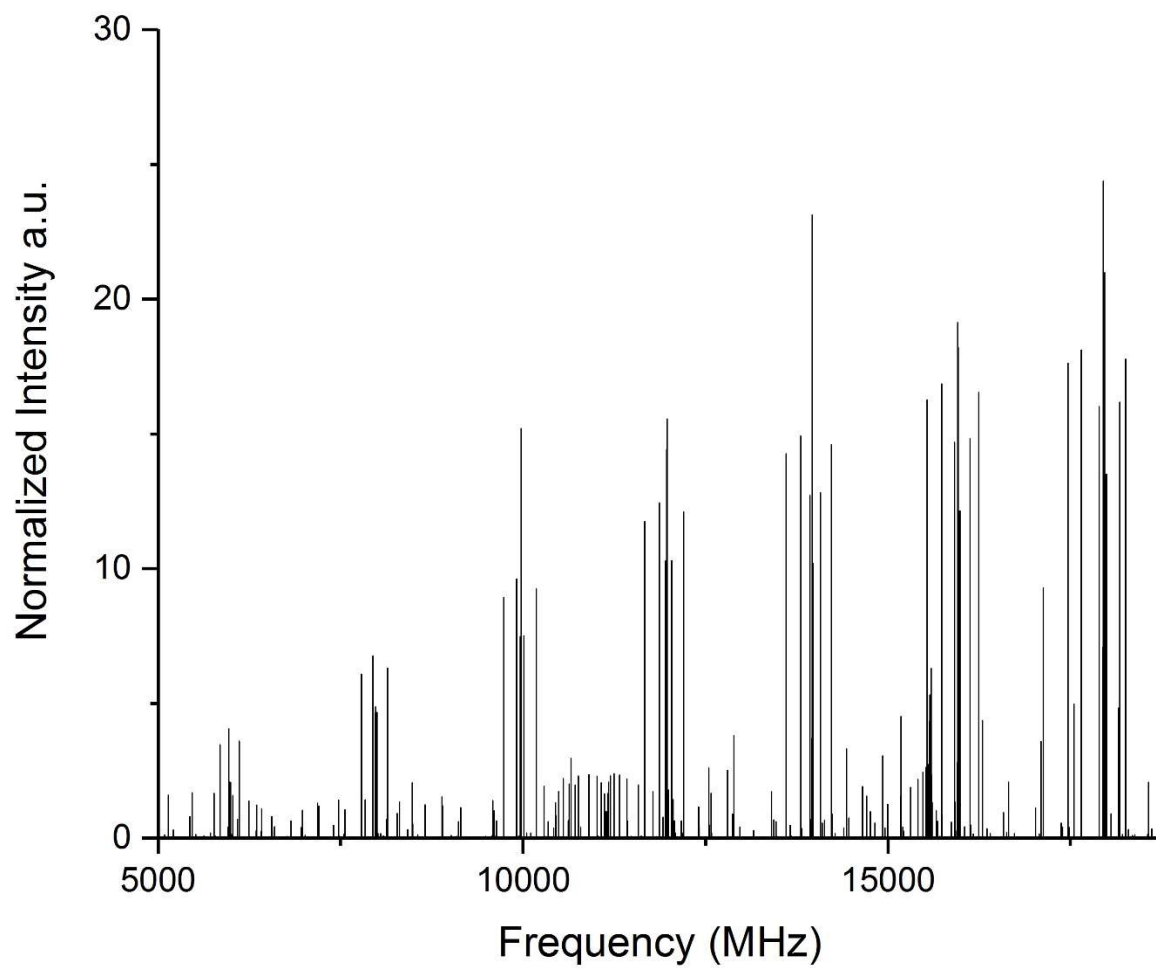
Figure 48 - Simulated spectrum of CHCACE2. Range is from 5 – 18.75 GHz.
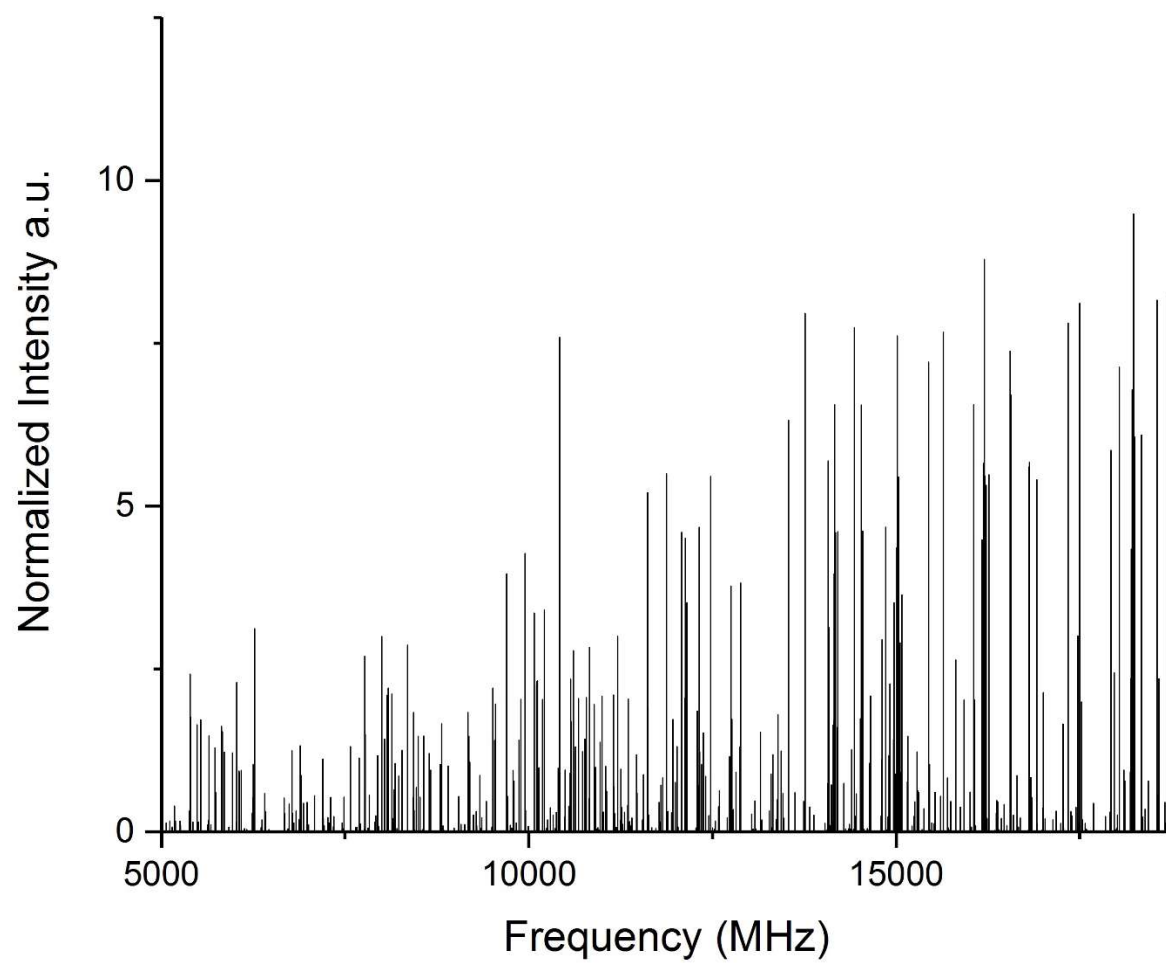
Figure 49 - Simulated spectrum of CHCABE1. Range is from 5 – 18.75 GHz.
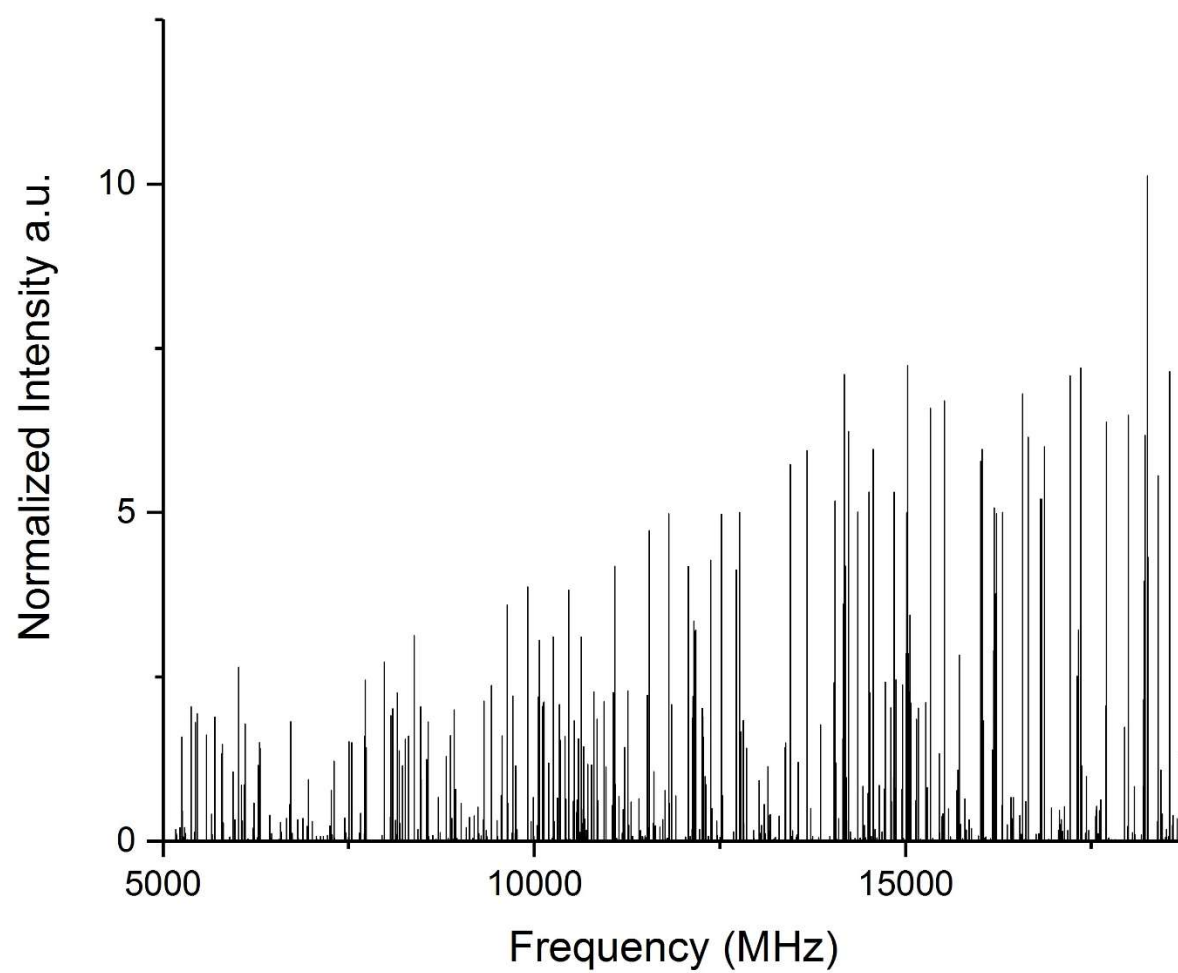
Figure 50 - Simulated spectrum of CHCABE2. Range is from 5 – 18.75 GHz.
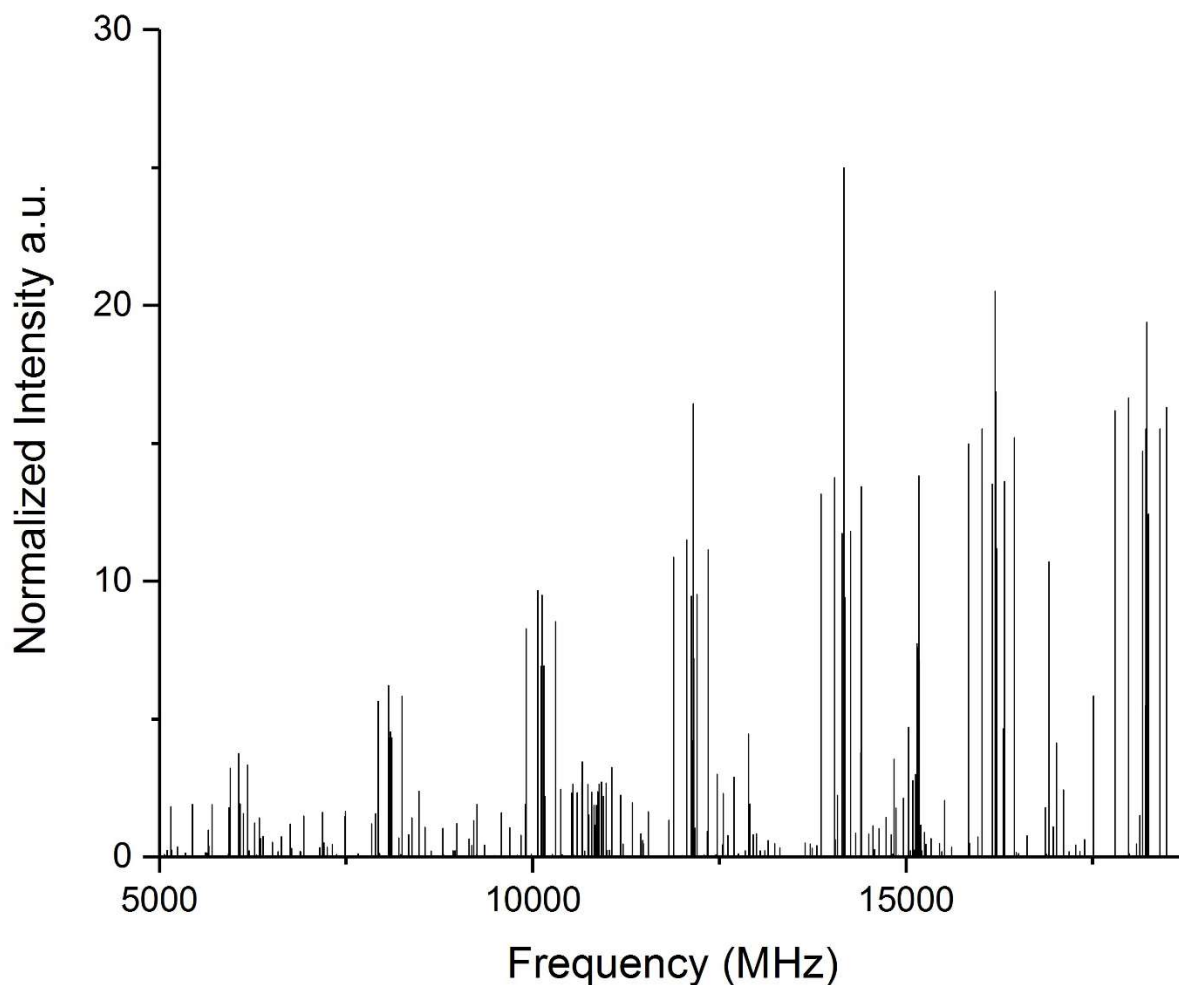
Figure 51 - Simulated spectrum of CHCABE3. Range is from 5 – 18.75 GHz.

All the simulated spectra are between the range of 5 GHz – 18.75 GHz as that is the range of the experimental spectra. The main theoretical spectrum we will focus on is that of CHCACE1 as that is the lowest energy conformer. It is likely that this conformer will be the most populated in the experimental spectrum as it is the lowest energy conformer. It is not impossible for the molecule to not be in the CHCACE2, CHCACA, CHCABE1, CHCABE2, and CHCABE3 structures, but less likely. Those figures were included for reference if ever needed.

Section 4.5 – Experimental Data

The experimental data for CHCA is in the following order: spectrum between 5 GHz –
10.25 GHz, 9.75 GHz – 14.5 GHz, and 14 GHz – 18.75 GHz.
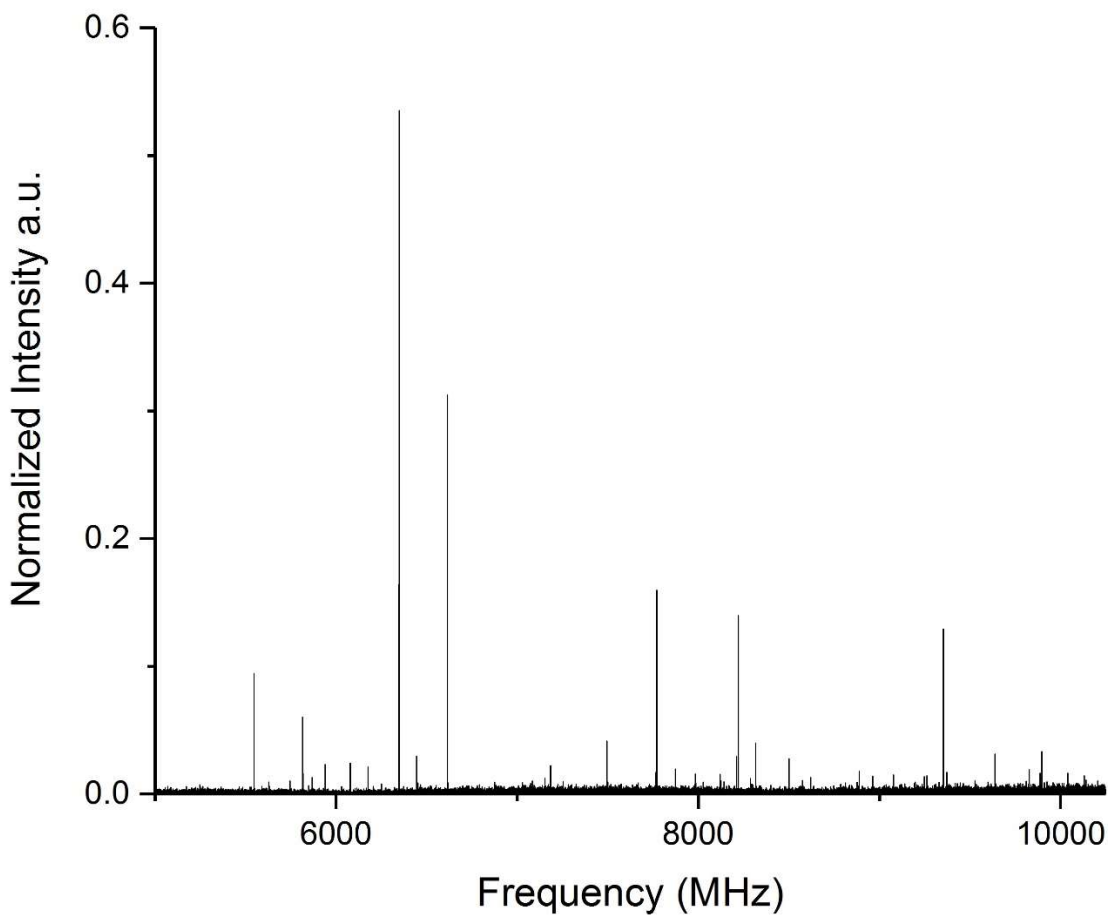
Figure 52 – Experimental data retrieved for CHCA using a CPFTMW spectrometer. The range is from 5 – 10.25
GHz.

The intensities at this range are low in comparison to the other frequency ranges. This is
because the instrument used is better optimized to obtain signals at higher frequencies.
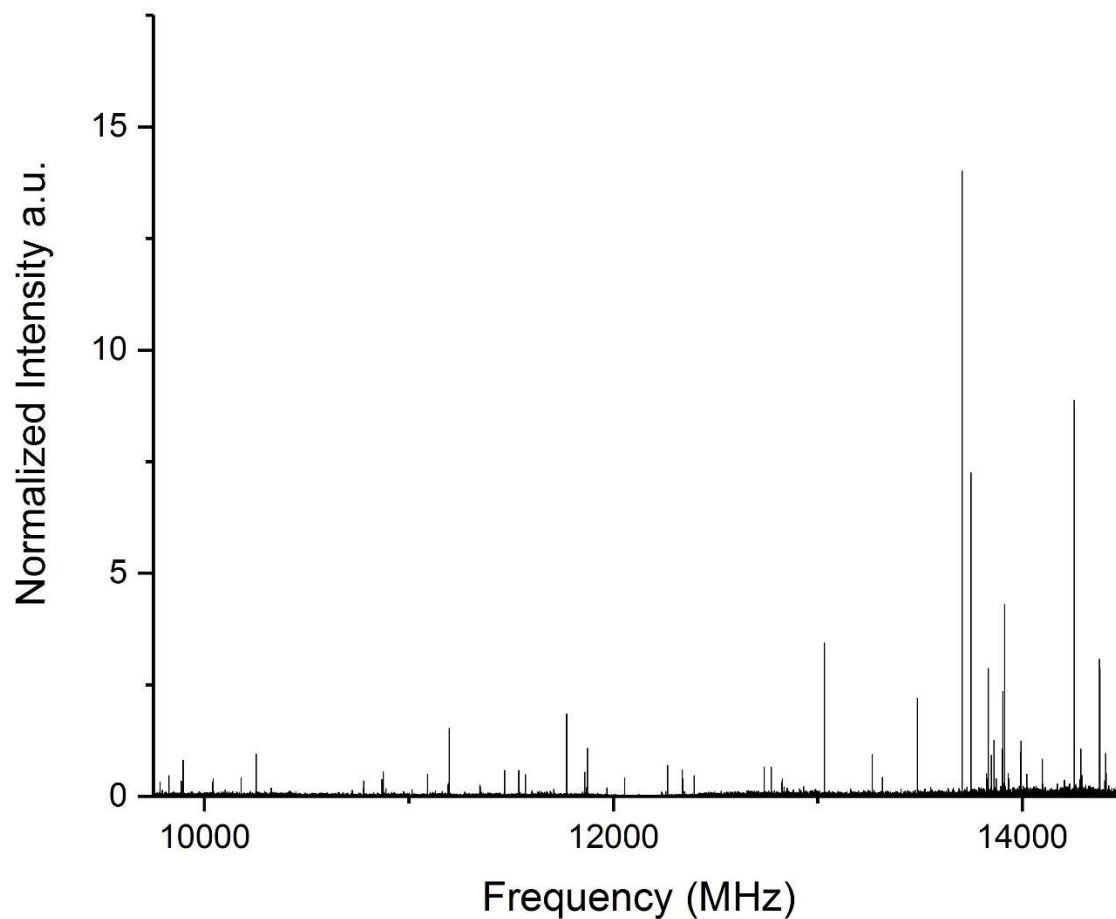
Figure 53 - Experimental data retrieved for CHCA using a CPFTMW spectrometer. The range is from 9.75 – 14.5 GHz.

As we get into the 14 GHz range, the intensities of the FID signals increase as this is entering the range in which the instrument is most sensitive.
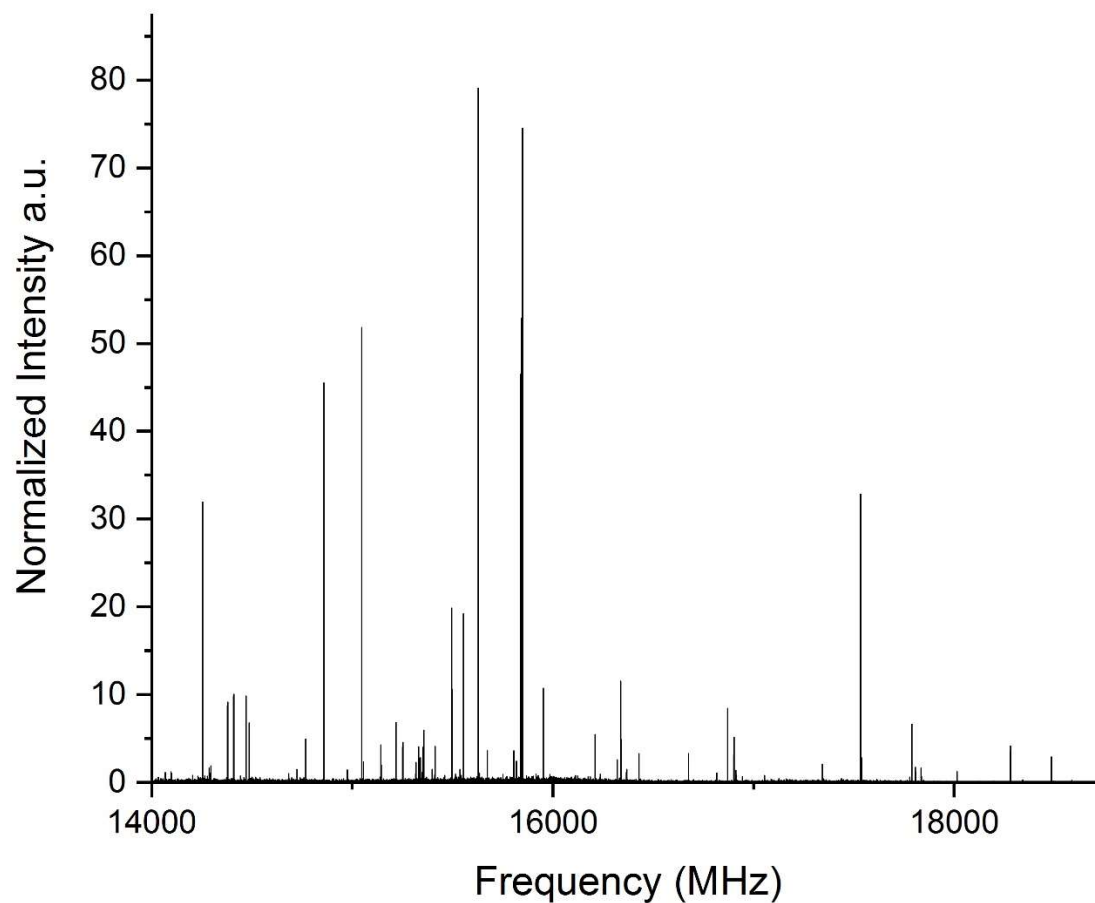
Figure 54 - Experimental data retrieved for CHCA using a CPFTMW spectrometer. The range is from 14 – 18.75 GHz.

The peaks are very intense in this region, and it is most likely the best region to look at when doing spectrum assignment as most peaks can be seen here with a relatively low signal to noise ratio.
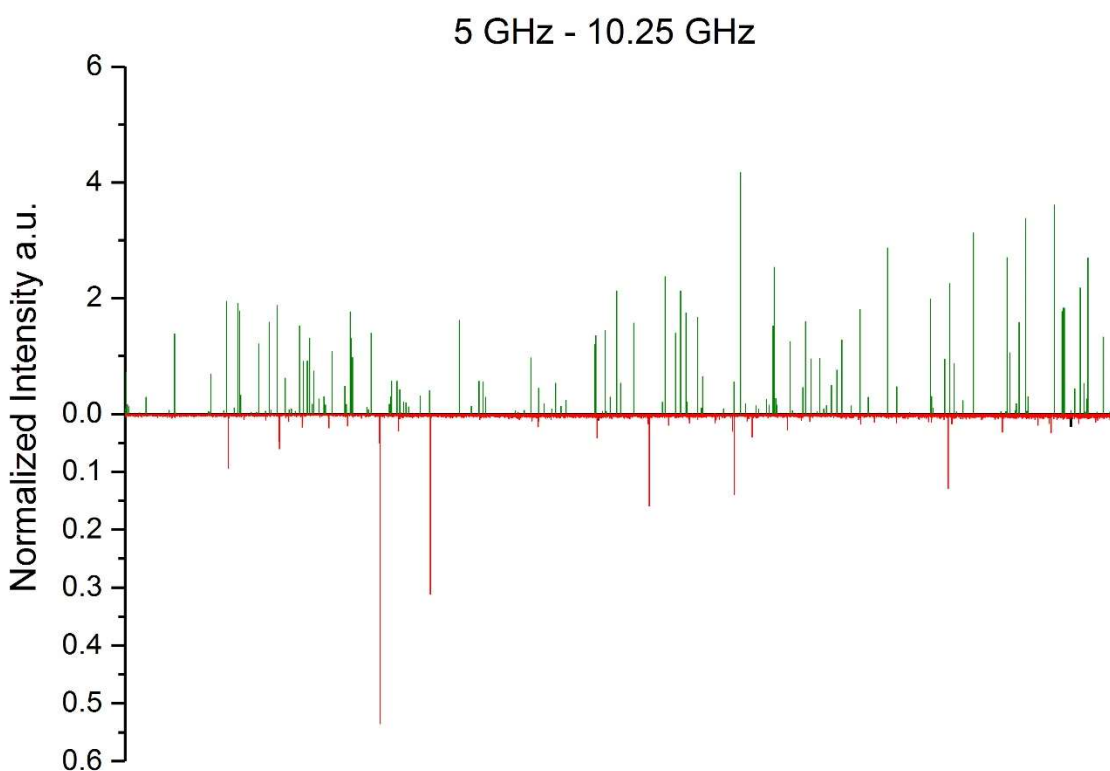
Figure 55 – Simulated (green) and experimental (red) spectra between 5-10.25 GHz.

Figure 55 compares the simulated and experimental spectra at a certain range to have a better idea what peaks can be assigned where. These spectra are not assigned yet but are in the process of being assigned. The experimental peaks are weak compared to the theoretical. The comparisons are shown better in the following figures where the experimental peaks are higher in intensity.
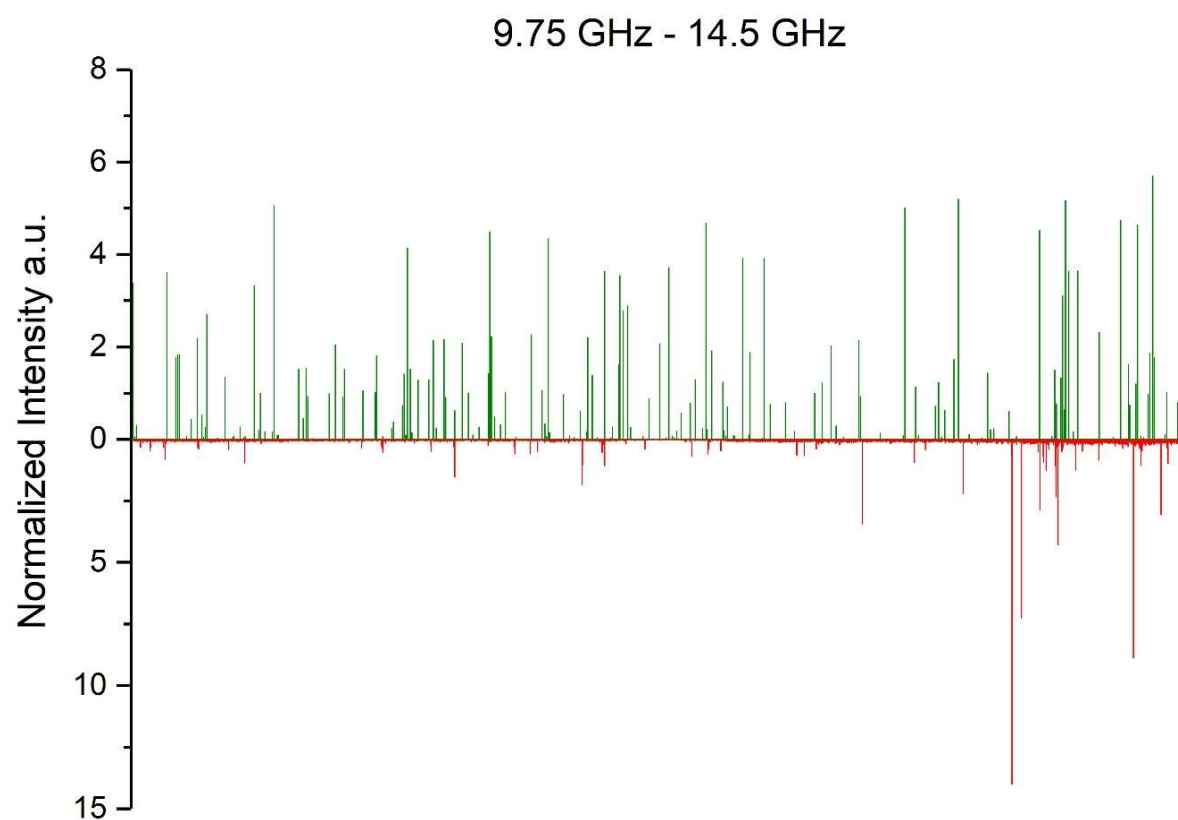
Figure 56 - Simulated (green) and experimental (red) spectra between 9.75-14.5 GHz.

The more relevant region in Figure 56 is on the right which is about 12 GHz – 14.5 GHz. This is because the intensities in that region are more easily seen and can help in assignment of the spectrum.
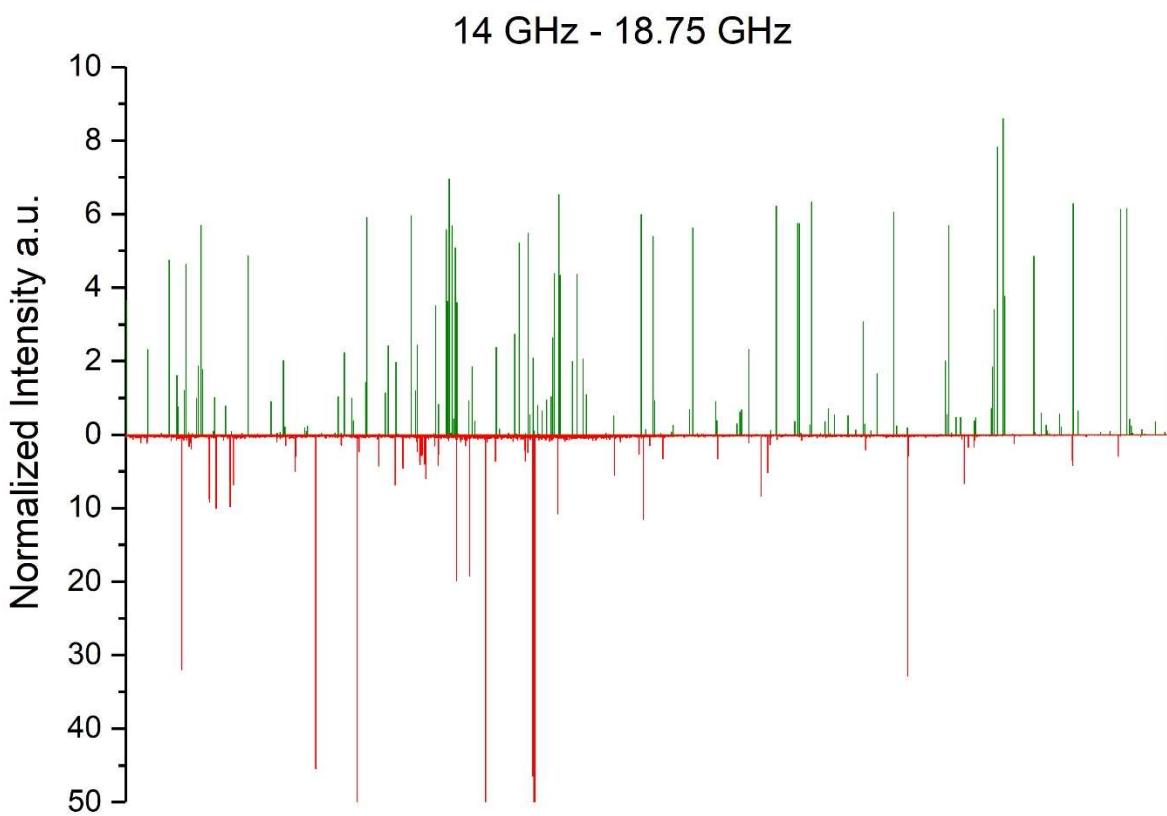
Figure 57 - Simulated (green) and experimental (red) spectra between 14-18.75 GHz.

The frequency region shown in Figure 57 will likely be the best region for assigning peaks as the signal to noise ratio is large. This allows us to see most rotational transitions at a strong intensity. As the spectrum moves into the 17 GHz – 18.75 GHz region, the signals appear to be losing intensity as the instrument loses sensitivity in that region.

Section 4.6 – Results

For the PES scans, it was predicted that the boat and axial conformers would be higher in energy than the chair and equatorial conformers as it is commonly known. This was confirmed with the PES scans of CHCA as the chair and equatorial structures were lower in energy than boat and axial structures. Looking at the CHCABE conformers, we can confirm what was mentioned in *Section 1.4*. Kao and Turner, who did a study on cyclohexanecarboxaldehyde, were able to show that the relative energies and stability of the molecules depended on the structure of the functional group. Similarly, in this case, the relative energy of cyclohexanecarboxylic acid was affected by the positioning of the functional group. The lowest energy conformer was the CHCA chair equatorial structure. The fitting of the experimental spectrum to the theoretical is still a work in-progress.

CHAPTER V

CHLOROSULFONIC ACID AND ITS HYDRATES

Section 5.1 – Potential Energy Surface Scan

This study of chlorosulfonic acid and its hydrates consist of *ab initio* calculations for the

monomer, monohydrate, dihydrate, and trihydrate. Due to the increasing complexity of the

monomer-hydrate interactions, a PES scan was only done for the monomer.
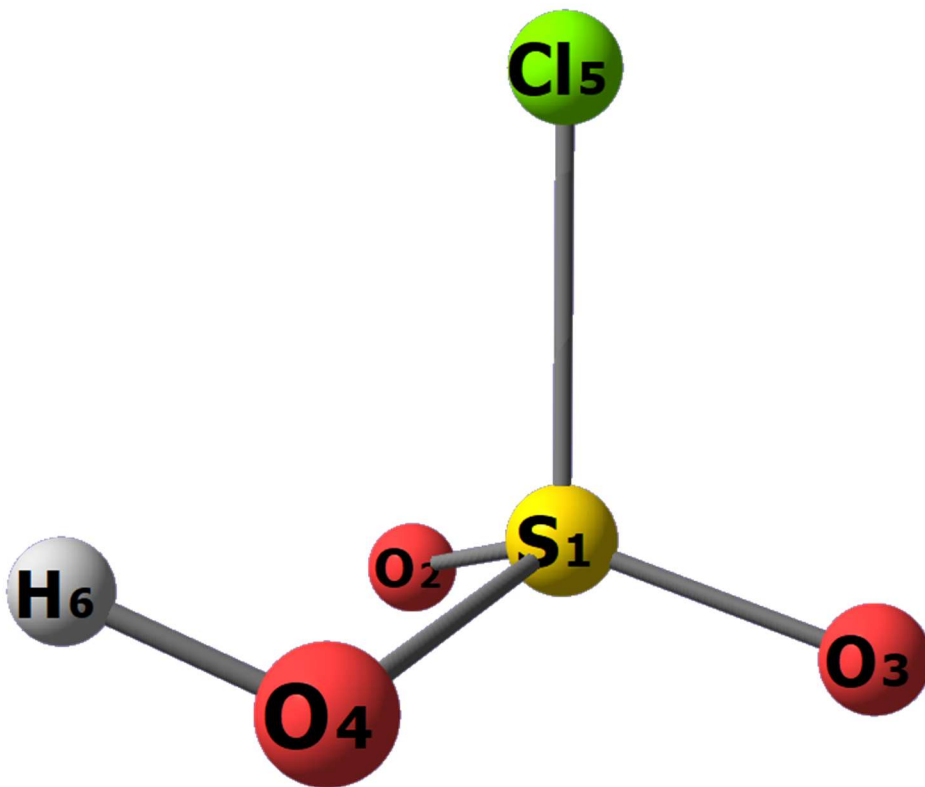
Figure 58 - Chlorosulfonic acid monomer (no water present in the complex).
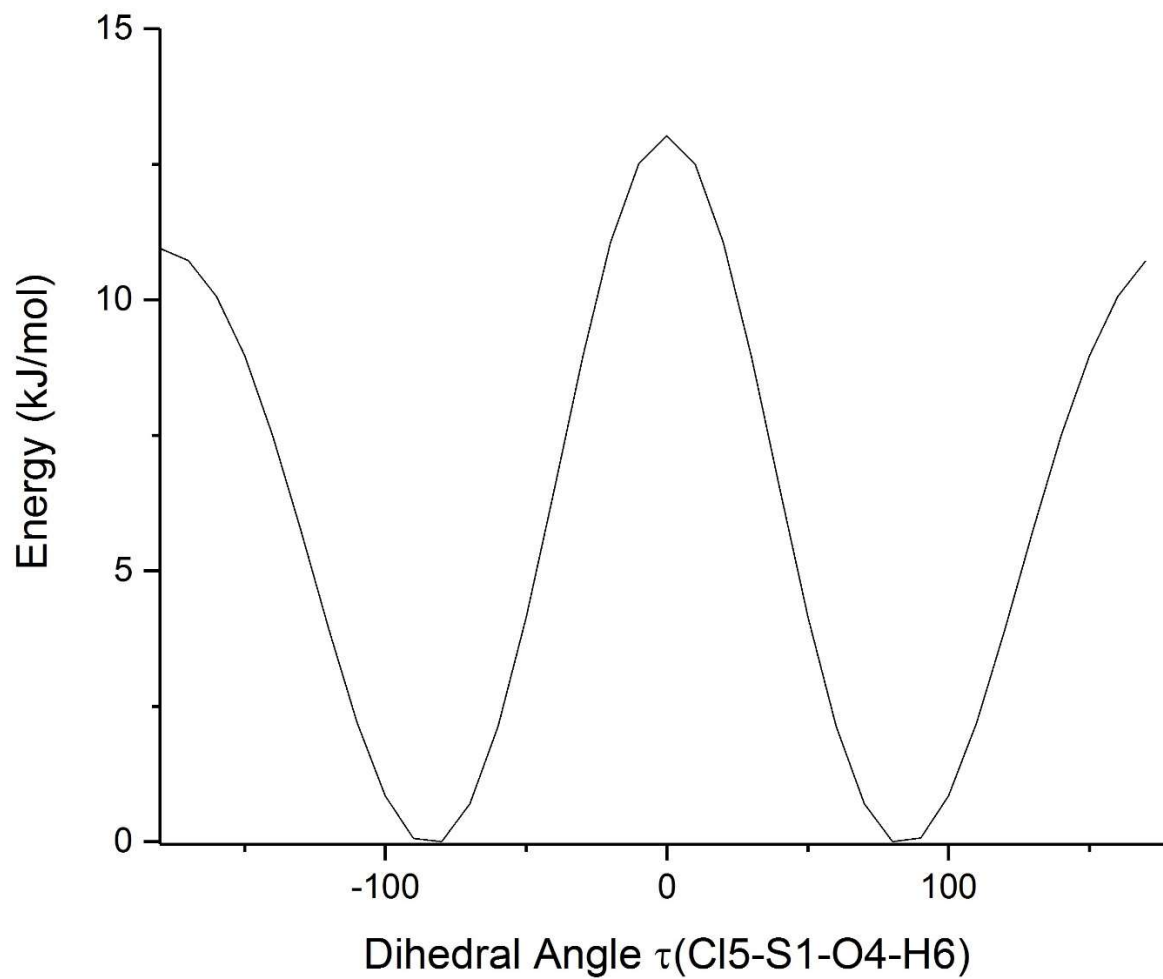
Figure 59 - PES scan for the chlorosulfonic acid monomer. The scan shows 2 minima at -80° and 80°.

The PES scan showed two possible conformers for the chlorosulfonic acid monomer. For the monomer, one structure optimization will be representative for both structures.
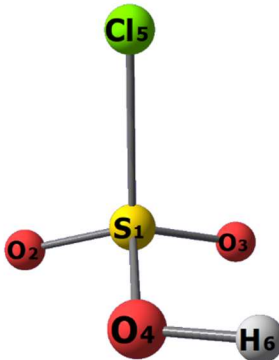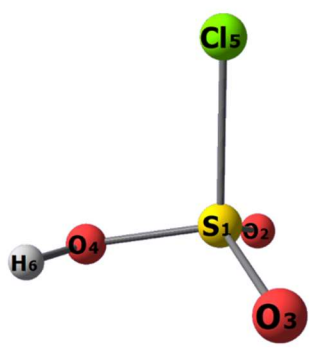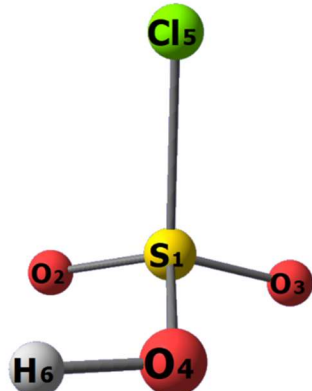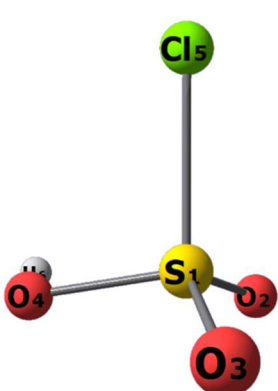
Figure 60 - Chlorosulfonic acid conformers shown from the front and side view at -80° and 80°.

This scan shows that the structure is most stable when the hydrogen is aligned with O2 or O3. One structure, optimized through DFT and MP2 methods with aug-cc-pVTZ basis set, will yield rotational values representative of both structures.

Section 5.2 – Geometry Optimization

The monomer, monohydrate, dihydrate, and trihydrate were optimized with the aforementioned methods and basis sets. The following abbreviations are listed for reference:

chlorosulfonic acid (clsa), monohydrate (mono), dihydrate (di), and trihydrate (tri) conformers. **A**, **B** and **C** are the rotational constants. μ_a, μ_b, and μ_c are the dipole moments. χ_{aa}, χ_{bb}, and χ_{cc}

are the nuclear quadrupole coupling (hyperfine) constants. *ΔD (kJ/mol)* is the relative energy and

ΔD$_o$ (kJ/mol) is the relative energy with the ZeroPoint (kJ/mol) correction added.
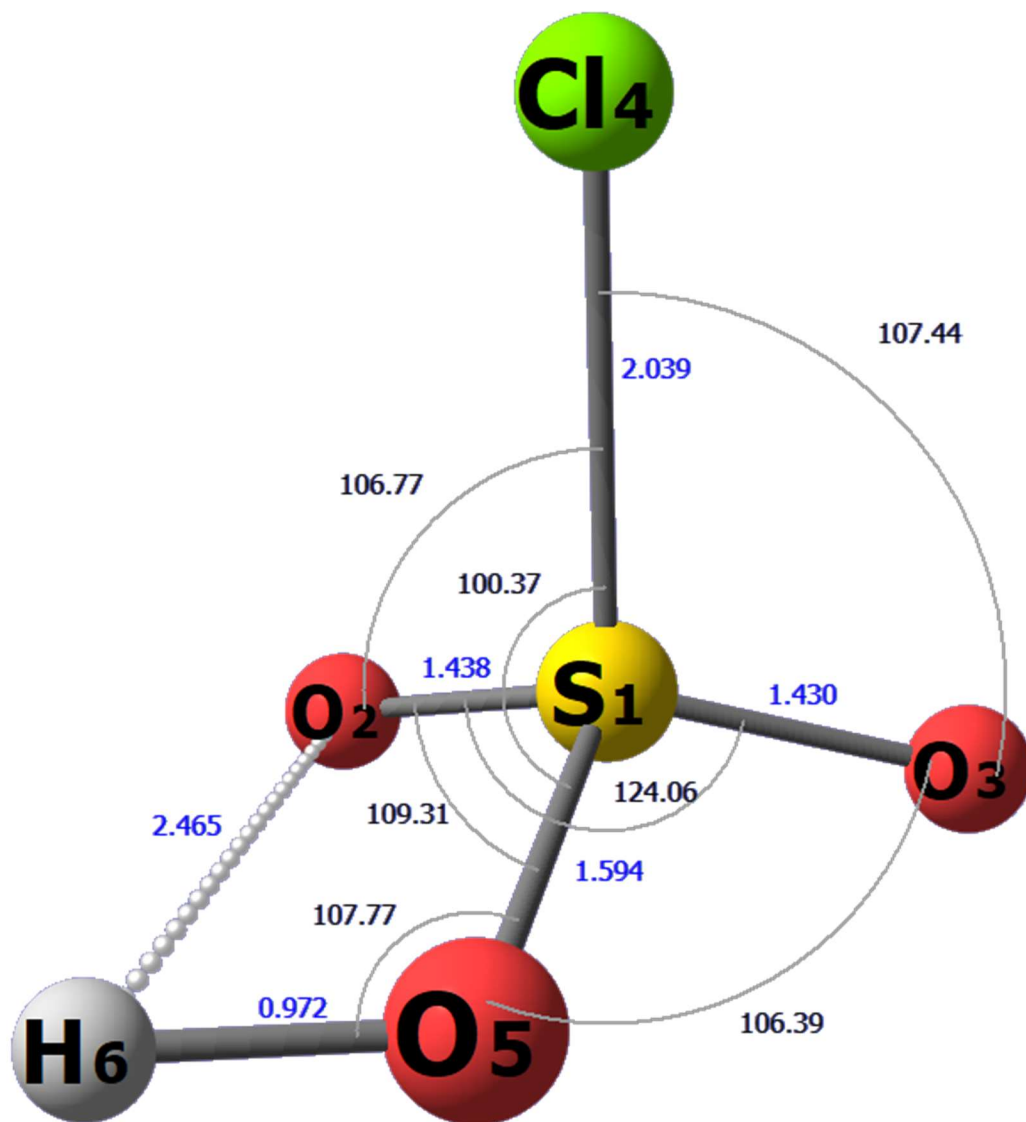
Figure 61 – The structural parameters of chlorosulfonic acid monomer.

Table 10 – Structural parameters of chlorosulfonic acid monomer. Visual is shown in Figure 61.

Parameter	Length	Parameter	Angle
$r(Cl_4\text{-}S_1)$	2.039 Å	$Cl_4S_1O_2$	106.77
$r(S_1\text{-}O_2)$	1.438 Å	$Cl_4S_1O_3$	107.44
$r(S_1\text{-}O_3)$	1.430 Å	$Cl_4S_1O_5$	100.37
$r(S_1\text{-}O_5)$	1.594 Å	$O_2S_1O_3$	124.06
$r(O_5\text{-}H_6)$	0.972 Å	$O_2S_1O_5$	109.31
$r(O_2\text{-}H_6)$	2.465 Å	$O_3S_1O_5$	106.39
-	-	$S_1O_5H_6$	107.77

In Figure 61, we can see that H6 aligns with O2. This happens similarly with O3. The distance of this interaction indicates a weak hydrogen bond which is what stabilizes the molecule and leads that structure to be the most stable. The bond length of the forementioned hydrogen bond is 2.465 Å. So not only does chlorosulfonic acid have intermolecular interactions with water, but the intramolecular hydrogen bond also adds to the stabilization of CLSA.
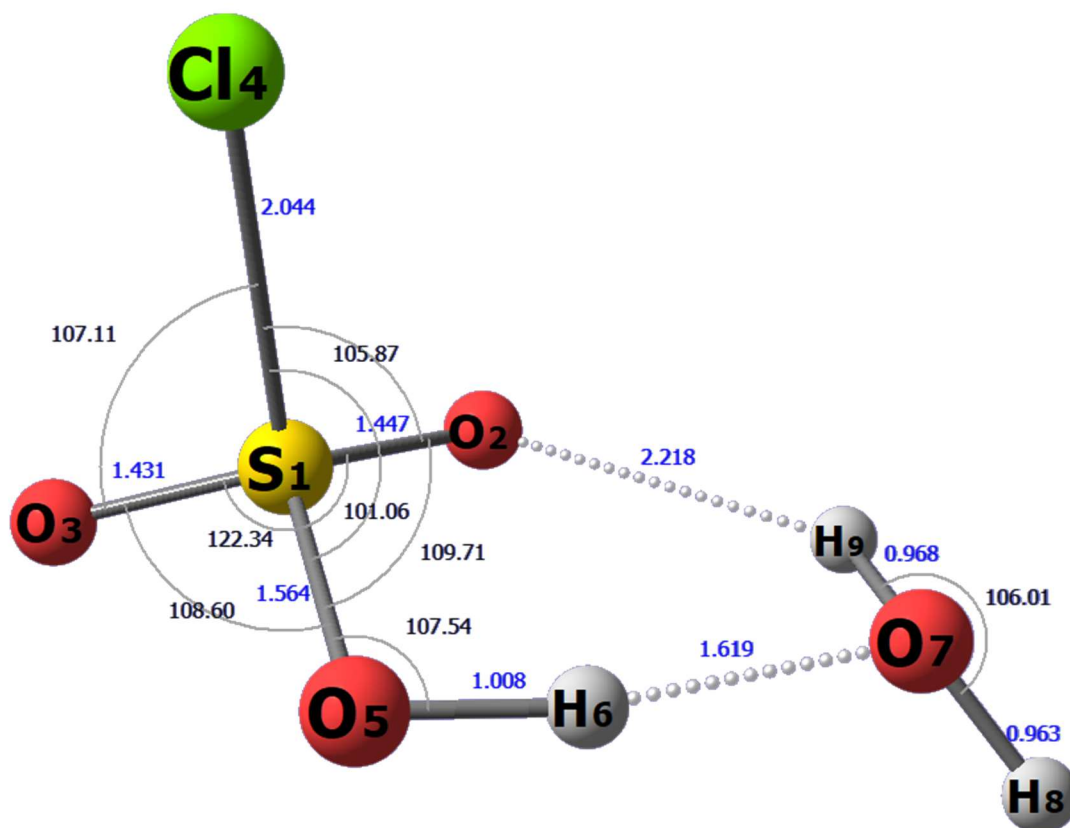
Figure 62 – Visual of chlorosulfonic acid monohydrate molecule and its structural parameters.

Table 11 - Structural parameters of chlorosulfonic acid monohydrate. Visual is shown in Figure 62.

Parameter	Length	Parameter	Angle
$r(Cl_4\text{-}S_1)$	2.044 Å	$Cl_4S_1O_2$	105.87
$r(S_1\text{-}O_2)$	1.447 Å	$Cl_4S_1O_3$	107.11
$r(S_1\text{-}O_3)$	1.431 Å	$Cl_4S_1O_5$	101.06
$r(S_1\text{-}O_5)$	1.564 Å	$O_2S_1O_3$	122.34
$r(O_5\text{-}H_6)$	1.008 Å	$O_2S_1O_5$	109.71
$r(O_2\text{-}H_9)$	2.218 Å	$O_3S_1O_5$	108.60
$r(H_6\text{-}O_7)$	1.619 Å	$S_1O_5H_6$	107.54
$r(O_7\text{-}H_8)$	0.963 Å	$H_8O_7H_9$	106.01
$r(O_7\text{-}H_9)$	0.968 Å	-	-

Upon the addition of a water molecule, chlorosulfonic acid begins to form hydrogen bonds. The water molecule arranges itself to a position where O7 can hydrogen bond with H6 and where H9 can hydrogen bond with O2. The distance of these hydrogen decrease as more water molecules are added to molecular system. The $Cl_4\text{-}S_1$ bond increases as more the molecule interacts with more water molecules. In the monohydrate, the $Cl_4\text{-}S_1$ bond is 2.044 Å whereas it was 2.039 Å before. This pattern continues throughout the hydrates. Similarly, the sulfur-oxygen bond lengths increase as more water molecules are added.

Figure 63 - Visual of chlorosulfonic acid dihydrate molecule and its structural parameters. The S_1-O_5 bond has decreased even further and the Cl_4-S_1 bond length increases.

Table 12 - Structural parameters of chlorosulfonic acid dihydrate. Visual is shown in Figure 63.

Parameter	Length	Parameter	Angle
r(Cl$_4$-S$_1$)	2.048 Å	Cl$_4$S$_1$O$_2$	105.16
r(S$_1$-O$_2$)	1.450 Å	Cl$_4$S$_1$O$_3$	107.53
r(S$_1$-O$_3$)	1.431 Å	Cl$_4$S$_1$O$_5$	101.37
r(S$_1$-O$_5$)	1.547 Å	O$_2$S$_1$O$_3$	120.95
r(O$_5$-H$_6$)	1.036 Å	O$_2$S$_1$O$_5$	110.88
r(O$_2$-H$_{12}$)	1.896 Å	O$_3$S$_1$O$_5$	109.02
r(H$_6$-O$_7$)	1.491 Å	S$_1$O$_5$H$_6$	111.31
r(O$_7$-H$_8$)	0.962 Å	H$_8$O$_7$H$_9$	106.48
r(O$_7$-H$_9$)	0.986 Å	H$_{11}$O$_{10}$H$_{12}$	106.12
r(H$_9$-O$_{10}$)	1.720 Å	-	-
r(O$_{10}$-H$_{11}$)	0.961 Å	-	-
r(O$_{10}$-H$_{12}$)	0.972 Å	-	-

In the dihydrate, we begin to see the formation of a pseudo-ring from the hydrogen bonds of the water molecules and chlorosulfonic acid. The forementioned patterns of the bond lengths continue as the hydrogen bond distances decrease and the Cl$_4$-S$_1$ and sulfur-oxygen bonds increase. Additionally, the hydrogens in the water molecules which are not hydrogen bonded, referred to as "free hydrogens," have been observed to be in an up or down orientation[1]. In Figure 63, we can see H8 and H11 in the down position. However, H8 can be up and H11 down, H8 can be up and H11 up, and H8 can be down and H11 up. In the case of chlorosulfonic acid,

trying to flip H8 to the up-position results in H8 returning to the down position during structure optimization. Further work can be done to confirm if the free hydrogens can flip freely in the monohydrate, dihydrate, and trihydrate.
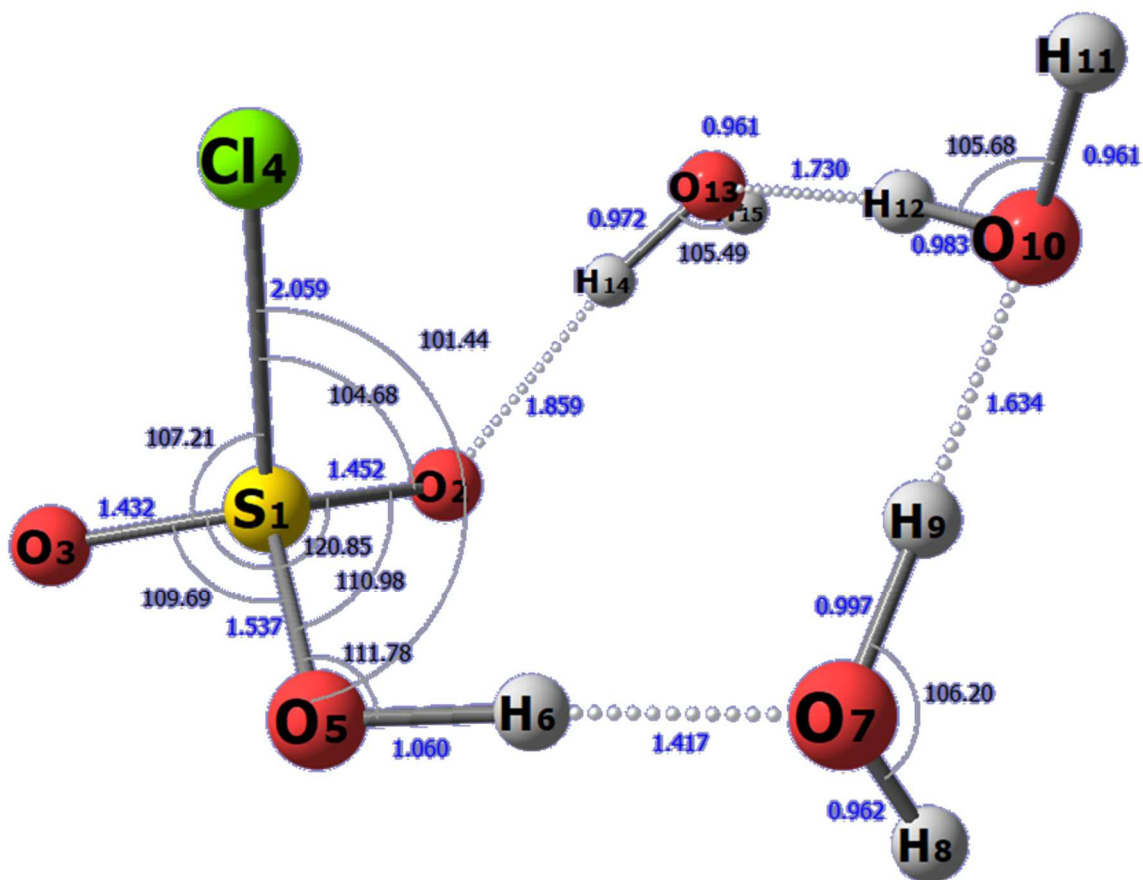
Figure 64 - Visual of chlorosulfonic acid trihydrate molecule and its structural parameters. This structure is referred to as trihydrate2.

Table 13 - Structural parameters of chlorosulfonic acid trihydrate. Visual is shown in Figure 64.

Parameter	Length	Parameter	Angle
$r(Cl_4\text{-}S_1)$	2.059 Å	$Cl_4S_1O_2$	104.68
$r(S_1\text{-}O_2)$	1.452 Å	$Cl_4S_1O_3$	107.21
$r(S_1\text{-}O_3)$	1.432 Å	$Cl_4S_1O_5$	101.44
$r(S_1\text{-}O_5)$	1.537 Å	$O_2S_1O_3$	120.85
$r(O_5\text{-}H_6)$	1.060 Å	$O_2S_1O_5$	110.98
$r(O_2\text{-}H_{14})$	1.859 Å	$O_3S_1O_5$	109.69
$r(H_6\text{-}O_7)$	1.417 Å	$S_1O_5H_6$	111.78
$r(O_7\text{-}H_8)$	0.962 Å	$H_8O_7H_9$	106.20
$r(O_7\text{-}H_9)$	0.997 Å	$H_{11}O_{10}H_{12}$	105.68
$r(H_9\text{-}O_{10})$	1.634 Å	$H_{14}O_{13}H_{15}$	105.49
$r(O_{10}\text{-}H_{11})$	0.961 Å	-	-
$r(O_{10}\text{-}H_{12})$	0.983 Å	-	-
$r(H_{12}\text{-}O_{13})$	1.730 Å	-	-
$r(O_{13}\text{-}H_{14})$	0.972 Å	-	-
$r(O_{13}\text{-}H_{15})$	0.961 Å	-	-

The trihydrate shown in Figure 64 is one of the higher energy conformers in the study mentioned in *Section 1.1* by Shujin Li. This is not the most stable trihydrate, but the same patterns of the bond lengths continue as it did with the dihydrate. The concept of free hydrogens still applies to the trihydrate but was not observed in this thesis.
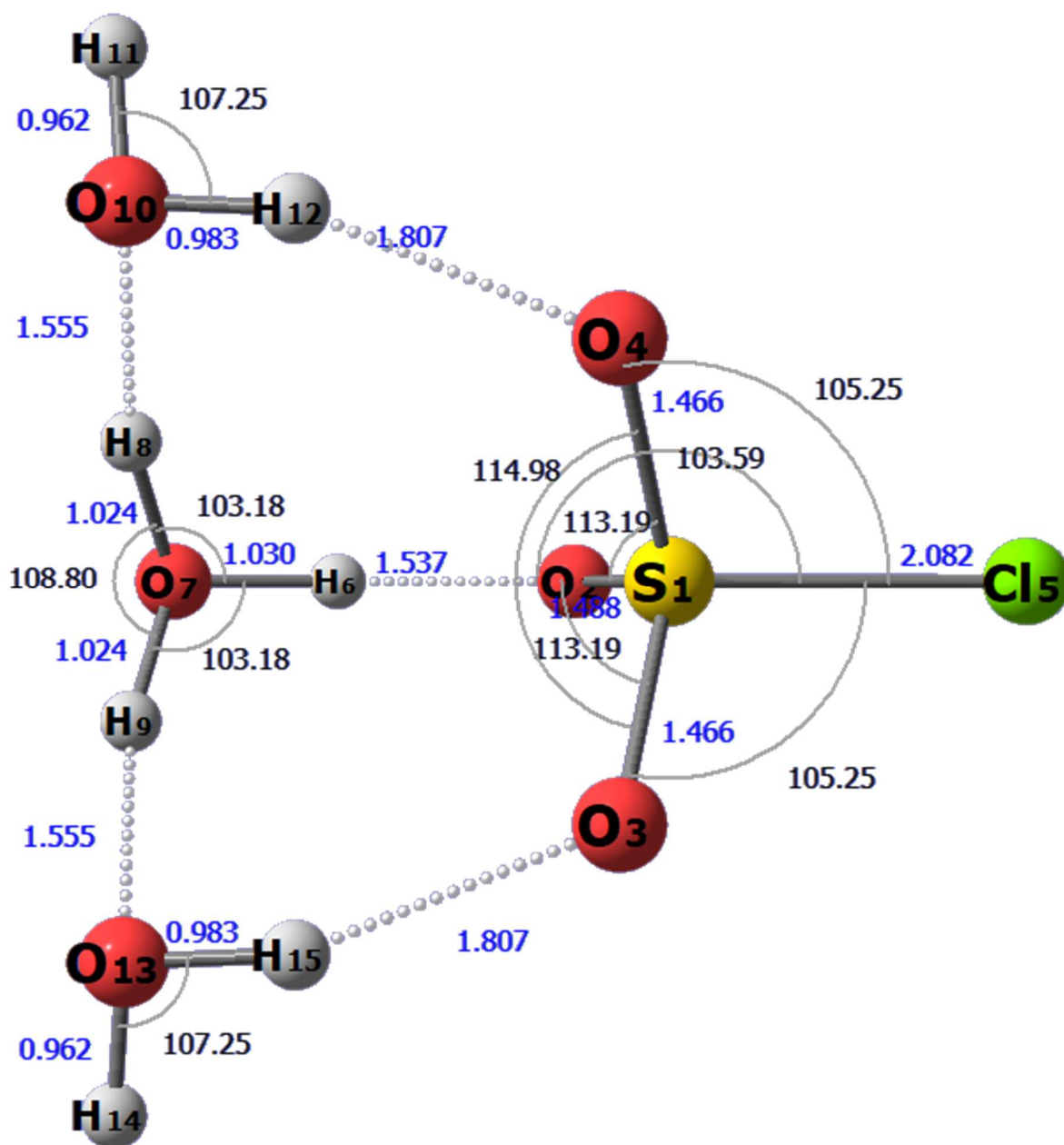
Figure 65 - The lower energy conformer of the trihydrate. This structure is referred to as trihydrate1.

Figure 65 shows the lowest energy structure like the one shown in the sulfonic acid literature review in *Section 1.1*. This structure also has the free hydrogens which are not hydrogen bonded and can be in an up or down position.

Table 14 - Rotational values of the four CLSA structures going from the monomer to the trihydrate (left to right). The values on this table were obtained using Density Functional Theory (B3LYP) with an aug-cc-pVTZ basis set.

Values	Monomer	Monohydrate	Dihydrate	Trihydrate1	Trihydrate2
ΔD	-	-	-	0	5.96
A	4,907.12	2,989.28	2,089.95	1,775.99	1,423.57
B	2,746.35	1,673.23	973.13	786.93	718.45
C	2,727.35	1,368.36	951.05	658.28	642.56
μ_a	0.58	4.29	4.79	4.4	4.6
μ_b	2.21	1.09	0.36	0	0.38
μ_c	1.6	0.046	0.65	1.24	0.07
χ_{aa}	-72.84	8.75	25.3	-69.68	35.53
$\chi_{bb} - \chi_{cc}$	0.998	-80.68	-96.4	2.17	83.26

In the trihydrate structure, two conformers were seen with a relative energy difference of 5.96 kJ/mol. The lower energy structure is shown in Figure 65 and is in agreement with the literature (Shujin Li, 2006). This is the structure that is most likely to be observed in the microwave spectrum of the trihydrate.

Table 15 - Rotational values of the four CLSA structures going from the monomer to the trihydrate (left to right). The values on this table were obtained using Second Order Møller–Plesset perturbation theory (MP2) with an aug-cc-pVTZ basis set. ΔD, ΔD_o, and the ZeroPoint energy are in units of kJ/mol.

Values	Monomer	Monohydrate	Dihydrate	Trihydrate2
A	4,928.69	2,990.95	2,065.75	1,447.99
B	2,824.43	1,770.59	1,091.68	844.12
C	2,795.87	1,431.05	1,020.1	727.56
μ_a	0.69	4.13	4.82	4.33
μ_b	1.88	1.02	0.52	0.32
μ_c	1.95	0.026	0.35	0.62
χ_{aa}	-67.22	14.31	32.46	22.93
$\chi_{bb} - \chi_{cc}$	2.15	-81.07	-51.61	50.59

The tables for CLSA rotational values are not organized in order of increasing energy, but instead are organized by increasing number of water molecules in the complex. The rotational constants for trihydrate1 were obtained using only the DFT method. For this reason, trihydrate1 is not included in Table 15. The following table, Table 16, will list the calculated nuclear quadrupole coupling constants of CLSA.

Table 16 - Hyperfine constants of CLSA monomer and its hydrates.

Structure	Methods	χ_{aa}	χ_{bb}	χ_{cc}
Monomer	DFT	-72.84	36.92	35.92
	MP2	-67.22	34.69	32.54
Monohydrate	DFT	8.75	-44.72	35.96
	MP2	14.31	-47.69	33.38
Dihydrate	DFT	25.3	-60.85	35.55
	MP2	32.46	-42.03	9.58
Trihydrate1	DFT	-69.68	35.93	33.76
	MP2	-	-	-
Trihydrate2	DFT	35.53	23.86	-59.40
	MP2	22.93	13.83	-36.76

Section 5.3 – Theoretical Spectra

The theoretical spectra of CLSA will be between the 6 GHz to 9 GHz range as that is the range that chlorosulfonic acid will be observed through CP-FTMW spectroscopy. These spectra, Figures 66 – 69, will guide the spectral assignment of chlorosulfonic acid once experimental data has been obtained. The simulated spectra are in the following order: CLSA monomer, CLSA monohydrate, CLSA dihydrate, and CLSA trihydrate2.

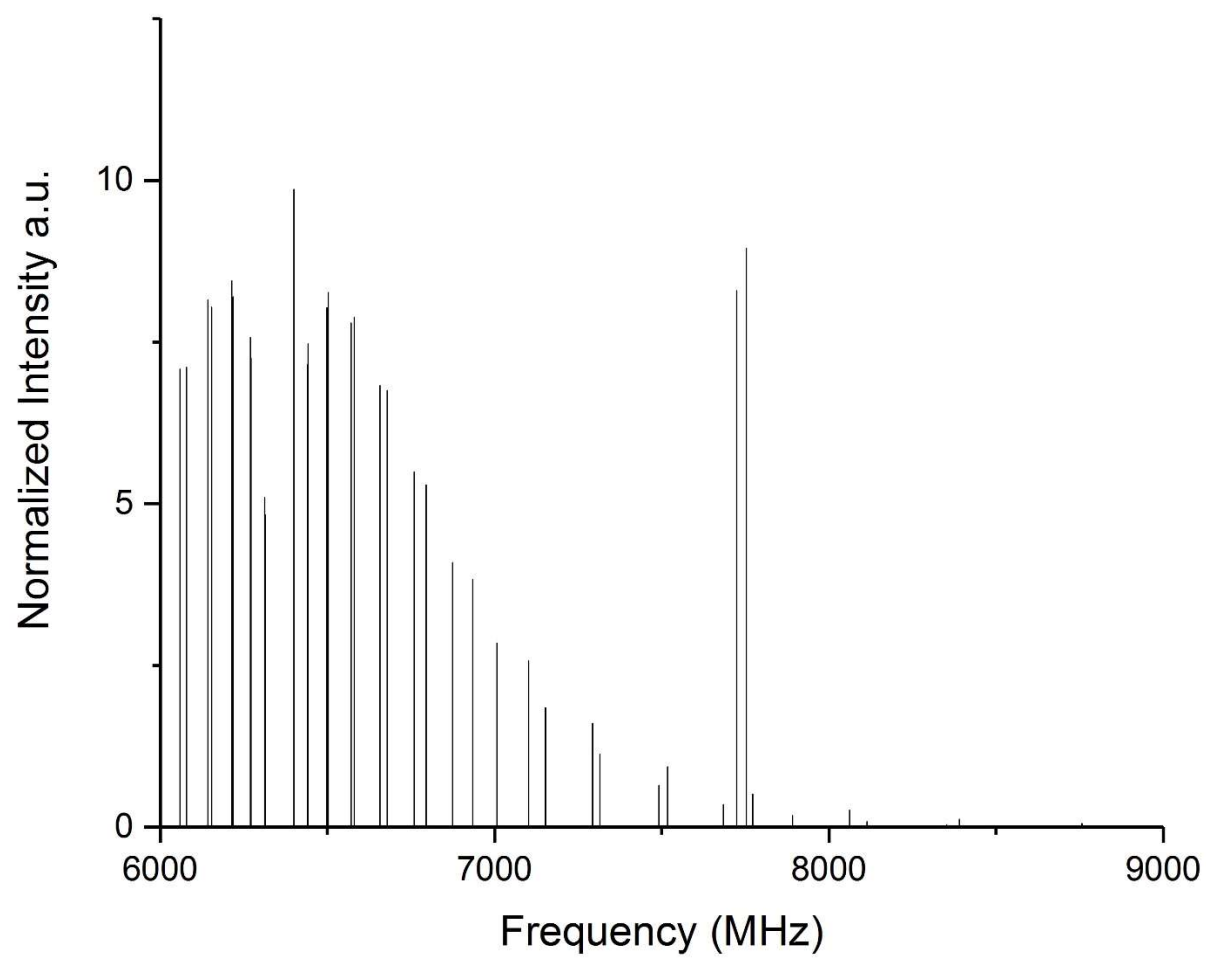Figure 66 – Simulated spectrum for chlorosulfonic acid monomer from the 6-9 GHz frequency range.
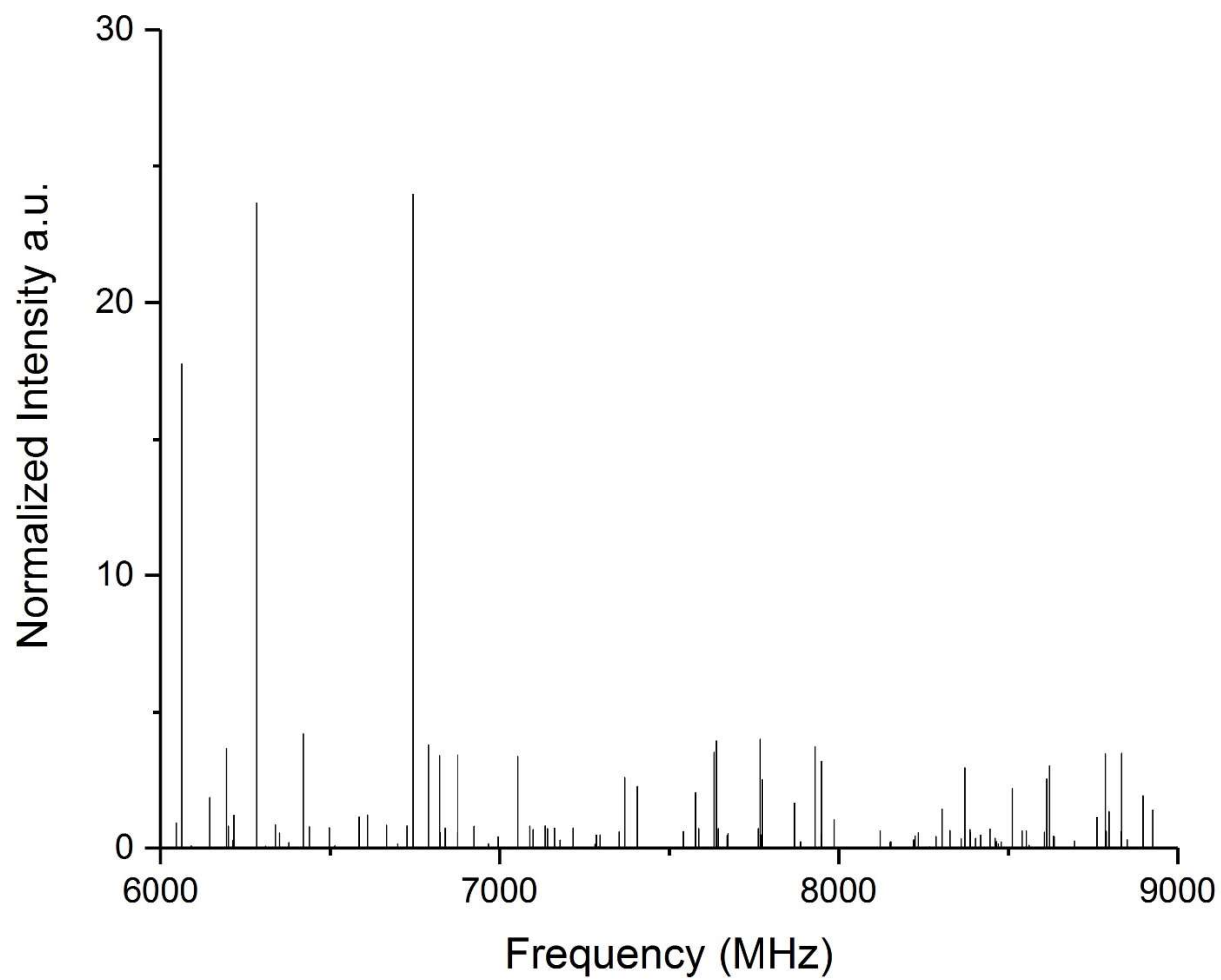
Figure 67 – Simulated spectrum for chlorosulfonic acid monohydrate from the 6-9 GHz frequency range.
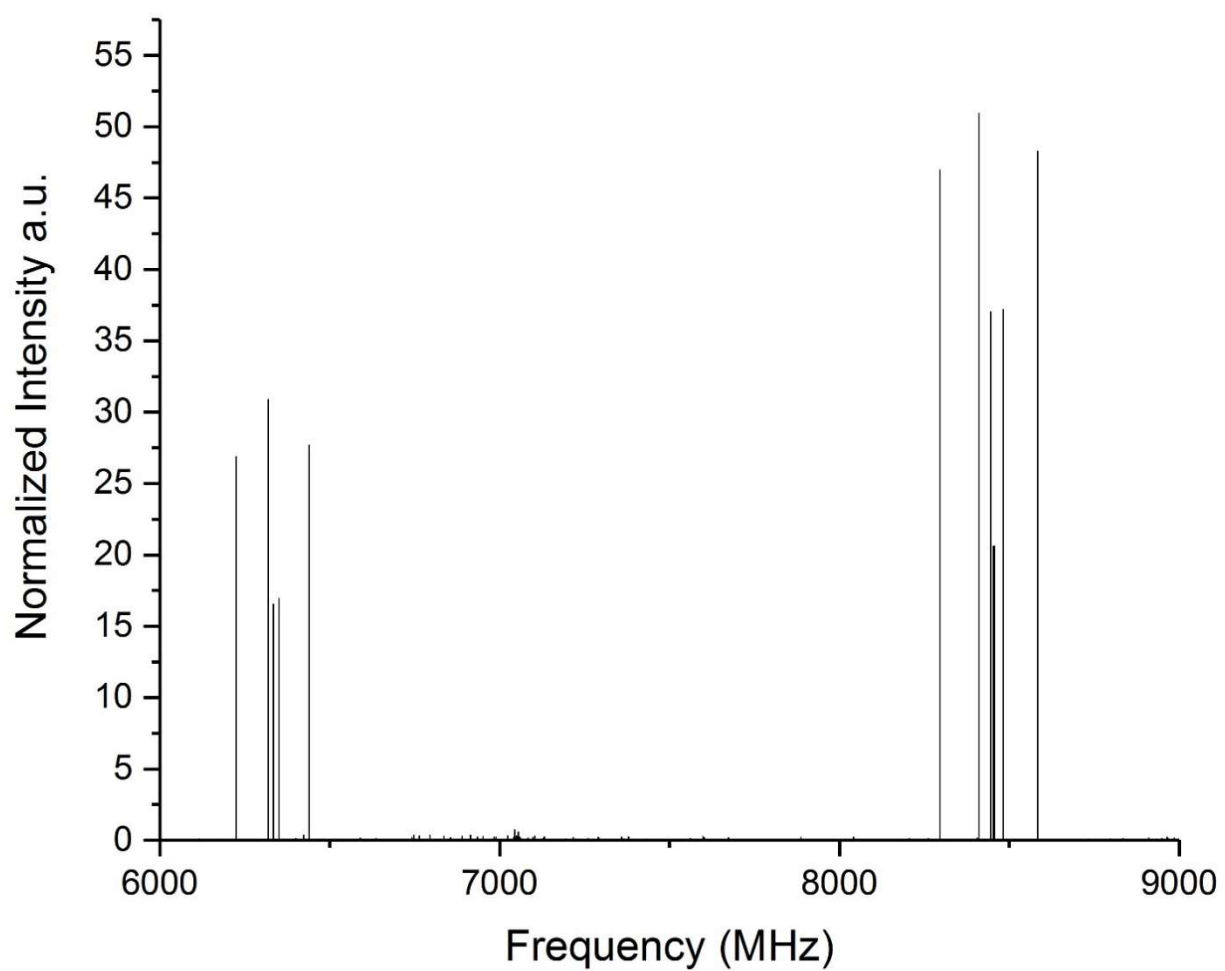
Figure 68 – Simulated spectrum for chlorosulfonic acid dihydrate from the 6-9 GHz frequency range.
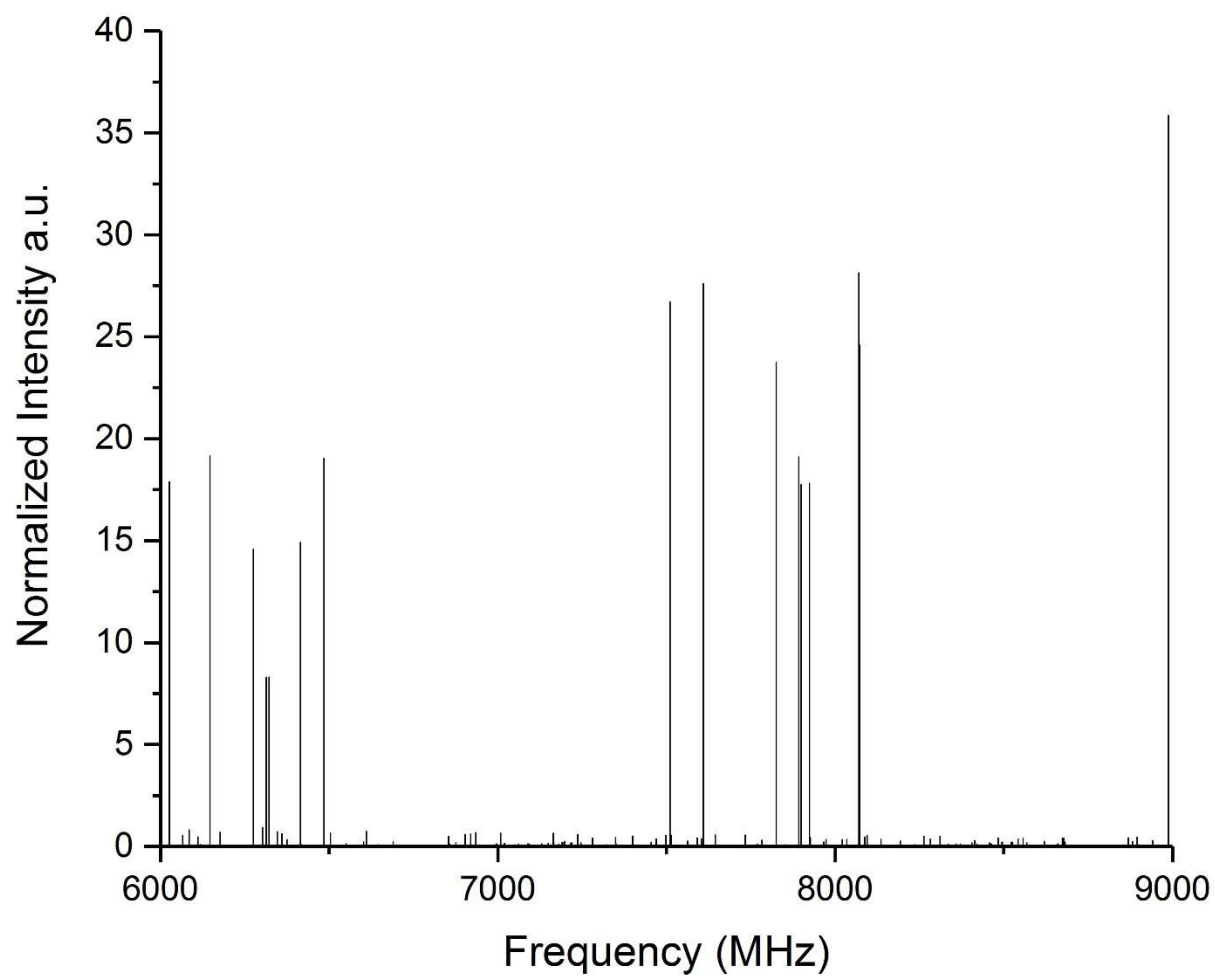
Figure 69 - Simulated spectrum for chlorosulfonic acid trihydrate2 from the 6-9 GHz frequency range.

Section 5.4 – Results

The *ab initio* study of chlorosulfonic acid involved geometry optimization of the monomer, monohydrate, dihydrate, and trihydrate using DFT and MP2 methods with aug-cc-pVTZ basis sets. From these optimizations, we obtained the rotational values including rotational constants, dipole moments, and nuclear quadrupole constants which were used to do spectral simulations between the ranges of 6 GHz – 9 GHz. From the structural parameters, we were able to observe the change in bond lengths as CLSA interacted with water. This can be related to PFAS such as PFOA or PFOS which have a polar and non-polar end. The polar end can form complexes with water that further stabilize the molecule. PFAS themselves are already very stable and have long half-lives. With the additional stabilization provided by water complexes, PFAS become more difficult to remove from the environment.

Section 5.5 – Conclusion

For CHCA, the most important molecular optimizations have been done with DFT and MP2 methods. What is left is to assign the experimental spectrum to the simulated spectrum of CHCACE1 with a low percent error and calculate its centrifugal distortion constants. The systematic study of PFOA and PFOS has been furthered with the *ab initio* study of chlorosulfonic acid as it is a precursor molecule. It was theoretically shown that chlorosulfonic acid is increasingly stabilized by water as the complexes form hydrogen bonds. The next step is to observe these complexes experimentally and assign the spectra to confirm all rotational values of CLSA. This will hopefully be done in a future collaboration with the Leopold group at the University of Minnesota.

REFERENCES

Amusia, M. Y., Msezane, A. Z., & Shaginyan, V. R. (2003). Density Functional Theory versus the Hartree–Fock Method: Comparative Assessment. *Physica Scripta*, *68*(6), C133–C140. https://doi.org/10.1238/physica.regular.068ac0133

Attila Szabo, & Ostlund, N. S. (1996). *Modern quantum chemistry : introduction to advanced electronic structure theory* (pp. 53, 54). Dover Publications.

A Perfluoroalkyl and Polyfluoroalkyl Substances (PFAS) in the U.S. Population. (n.d.). https://www.atsdr.cdc.gov/pfas/docs/PFAS_in_People.pdf

Badawi, H. M. (1996). An ab initio study of internal rotation in cyclohexanecarboxaldehyde and cyclohexanecarboxylic acid fluoride and chloride. *Journal of Molecular Structure: THEOCHEM*, *369*(1-3), 75–83. https://doi.org/10.1016/s0166-1280(96)04642-8

Balle, T. J., & Flygare, W. H. (1981). Fabry–Perot cavity pulsed Fourier transform microwave spectrometer with a pulsed nozzle particle source. *Review of Scientific Instruments*, *52*(1), 33–45. https://doi.org/10.1063/1.1136443

Basic Radio Propagation Predictions FOR SEPTEMBER 1950 Three Months in Advance. (1950). https://nvlpubs.nist.gov/nistpubs/Legacy/brpd-crpl-d/brpd-crpl-d70.pdf

Basis Sets in Computational Chemistry. (2021). In E. Perlt (Ed.), *Lecture Notes in Chemistry*. Springer International Publishing. https://doi.org/10.1007/978-3-030-67262-1

BrightSpec: Product Portfolio. (n.d.). BrightSpec. Retrieved from http://brightspec.com/products-academic/

Brown, G. G., Dian, B. C., Douglass, K. O., Geyer, S. M., & Pate, B. H. (2006). The rotational spectrum of epifluorohydrin measured by chirped-pulse Fourier transform microwave spectroscopy. *Journal of Molecular Spectroscopy*, *238*(2), 200–212. https://doi.org/10.1016/j.jms.2006.05.003

Brown, G. G., Dian, B. C., Douglass, K. O., Geyer, S. M., Shipman, S. T., & Pate, B. H. (2008). A broadband Fourier transform microwave spectrometer based on chirped pulse excitation. *Review of Scientific Instruments*, *79*(5), 053103. https://doi.org/10.1063/1.2919120

Cafe, K. B. R. (2017, January 2). *The New Field of Microwave Spectroscopy, July 1949 Radio and Television News*. https://www.rfcafe.com/references/radio-news/new-field-microwave-spectroscopy-radio-television-news-july-1949.htm

Computational Chemistry Comparison and Benchmark - Calculated electric dipole moments. (n.d.). Cccbdb.nist.gov. Retrieved from https://cccbdb.nist.gov/dipole3x.asp?method=3&basis=18

Computational Chemistry Comparison and Benchmark - Calculated Rotational Constants. (n.d.). Cccbdb.nist.gov. Retrieved from https://cccbdb.nist.gov/rotcalc2x.asp

Computational Chemistry Comparison and Benchmark – Experimental data. (n.d.). Cccbdb.nist.gov. Retrieved from https://cccbdb.nist.gov/exp2x.asp?casno=630080&charge=0

Clark, S. (2003, May 4). *The Hohenberg-Kohn Theorems*. Cmt.dur.ac.uk. http://cmt.dur.ac.uk/sjc/thesis_ppr/node12.html

Cook, R. L. (2003). Microwave molecular spectroscopy. *Encyclopedia of Physical Science and Technology*, 799–852. https://doi.org/10.1016/b0-12-227410-5/00447-6

Cyclohexane Conformational Analysis. (n.d.). Research.cm.utexas.edu. http://research.cm.utexas.edu/nbauld/teach/cyclohex.html

David, C., & Sherrill. (2000). *An Introduction to Hartree-Fock Molecular Orbital Theory*. http://vergil.chemistry.gatech.edu/courses/chem6485/pdf/hf-intro.pdf

Density Functional Theory for Beginners. (2019). Ex.ac.uk. http://newton.ex.ac.uk/research/qsystems/people/coomer/dft_intro.html

Dubrow, A. (2021, January 25). *Simulating 800,000 Years of California Earthquake History to Pinpoint Risks - Latest News - Texas Advanced Computing Center*. Www.tacc.utexas.edu. https://www.tacc.utexas.edu/-/simulating-800-000-years-of-california-earthquake-history-to-pinpoint-risks

Dunning, T. H. (1989). Gaussian basis sets for use in correlated molecular calculations. I. The atoms boron through neon and hydrogen. *The Journal of Chemical Physics*, *90*(2), 1007–1023. https://doi.org/10.1063/1.456153

ENIAC - CHM Revolution. (2019). Computerhistory.org. https://www.computerhistory.org/revolution/birth-of-the-computer/4/78

Evans, M. (n.d.). *Microwave Rotational Spectroscopy*. https://sci.tanta.edu.eg/files/microwave-rotational-spectroscopy-mce.pdf

Evolving the Early Universe in 24 Hours on Frontera - Latest News - Texas Advanced Computing Center. (n.d.). Www.tacc.utexas.edu. Retrieved from https://www.tacc.utexas.edu/-/evolving-the-early-universe-in-24-hours-on-frontera

Foresman, J. B. (1996a). *Exploring chemistry with electronic structure methods. Foresman, Æleen Frisch* (pp. 267–268). Gaussian.

Foresman, J. B. (1996b). *Exploring chemistry with electronic structure methods. Foresman, Æleen Frisch* (pp. 171–172). Gaussian.

Forman, P., & Smithsonian Institution Washington Dc. (1985). *The First Atomic Clock Program: NBS, 1947-1954.* Ft. Belvoir Defense Technical Information Center 03 Dec.

Fradette, R. (2016). *Understanding Vacuum and Vacuum Measurement.* https://solarmfg.com/wp-content/uploads/2016/02/Understanding-Vacuum-9.pdf

Garland, C. W., Nibler, J. W., & Shoemaker, D. P. (2009). *Experiments in physical chemistry.* Mcgraw-Hill Higher Education.

Garland, C., Nibler, J., & Shoemaker, D. (n.d.). *Experiments in Physical Chemistry Eighth Edition.* https://dailydialectics.com/education/TEXTBOOKS/PChemLabTXT.pdf

Ghisi, R., Vamerali, T., & Manzetti, S. (2019). Accumulation of perfluorinated alkyl substances (PFAS) in agricultural plants: A review. *Environmental Research*, *169*, 326–341. https://doi.org/10.1016/j.envres.2018.10.023

Gordy, W. (1983). Early events and some later developments in microwave spectroscopy. *Journal of Molecular Structure*, *97*, 17–32. https://doi.org/10.1016/0022-2860(83)90172-2

Hanson, D., Harvey, E., Sweeney, R., & Zielinski, T. (2020, March 18). *11.2: Gaussian Basis Sets.* Chemistry LibreTexts. https://chem.libretexts.org/Courses/Pacific_Union_College/Quantum_Chemistry/11:_Computational_Quantum_Chemistry/11.02:_Gaussian_Basis_Sets

Hanson, D., Harvey, E., Sweeny, R., & Zielinski, T. (2013, October 3). *9.7: The Self-Consistent Field Approximation (Hartree-Fock Method).* Chemistry LibreTexts. https://chem.libretexts.org/Bookshelves/Physical_and_Theoretical_Chemistry_Textbook_Maps/Book%3A_Quantum_States_of_Atoms_and_Molecules_(Zielinksi_et_al)/09%3A_The_Electronic_States_of_the_Multielectron_Atoms/9.07%3A_The_Self-Consistent_Field_Approximation_(Hartree-Fock_Method)

Hauptschein, M., & Braid, M. (1961). Fluorocarbon Halosulfates and a New Route to Fluorocarbon Acids and Derivatives. I. Polyfluoroalkyl Chlorosulfates1. *Journal of the American Chemical Society*, *83*(11), 2500–2505. https://doi.org/10.1021/ja01472a019

Houghton, N. (2013a, October 2). *Microwave Rotational Spectroscopy*. Chemistry LibreTexts. https://chem.libretexts.org/Bookshelves/Physical_and_Theoretical_Chemistry_Textbook _Maps/Supplemental_Modules_(Physical_and_Theoretical_Chemistry)/Spectroscopy/Ro tational_Spectroscopy/Microwave_Rotational_Spectroscopy#_ENREF_4

Houghton, N. (2013b, October 2). *Microwave Rotational Spectroscopy*. Chemistry LibreTexts. https://chem.libretexts.org/Bookshelves/Physical_and_Theoretical_Chemistry_Textbook _Maps/Supplemental_Modules_(Physical_and_Theoretical_Chemistry)/Spectroscopy/Ro tational_Spectroscopy/Microwave_Rotational_Spectroscopy#_ENREF_4

Huff, A. K., Love, N., & Leopold, K. R. (2021). Microwave Study of Triflic Acid Hydrates: Evidence for the Transition from Hydrogen-Bonded Clusters to a Microsolvated Ion Pair. *The Journal of Physical Chemistry A*, *125*(36), 8033–8046. https://doi.org/10.1021/acs.jpca.1c06815

Jian, J.-M., Chen, D., Han, F.-J., Guo, Y., Zeng, L., Lu, X., & Wang, F. (2018). A short review on human exposure to and tissue distribution of per- and polyfluoroalkyl substances (PFASs). *Science of the Total Environment*, *636*, 1058–1069. https://doi.org/10.1016/j.scitotenv.2018.04.380

John Michael Hollas, & Wiley, J. (2010). *Modern spectroscopy*. John Wiley & Sons Ltd.

Kao, P. N., & Turner, P. H. (1979). Conformational study of cyclohexanecarboxaldehyde by microwave spectroscopy. *Journal of the American Chemical Society*, *101*(16), 4497–4499. https://doi.org/10.1021/ja00510a011

Koch, C. P., Lemeshko, M., & Sugny, D. (2019). Quantum control of molecular rotation. *Reviews of Modern Physics*, *91*(3). https://doi.org/10.1103/revmodphys.91.035005

Lecture 4 Angular Momentum and Rigid-Rotor Models and. (n.d.). Retrieved from https://web2.aabu.edu.jo/tool/course_file/lec_notes/403741_Lecture%203%20Angular% 20Momentum.pdf

Lecture 11 Quantum rigid rotor Study Goal of This Lecture. (n.d.). https://quantum.ch.ntu.edu.tw/online_courses/PCIIQC2009/PDF/Lecture11.pdf

Lehmler, H.-J. (2005). Synthesis of environmentally relevant fluorinated surfactants—a review. *Chemosphere*, *58*(11), 1471–1496. https://doi.org/10.1016/j.chemosphere.2004.11.078

Li, S., Tao, F.-M., & Gu, R. (2006). Theoretical study on the ionic dissociation of halosulfonic acids in small water clusters. *Chemical Physics Letters*, *426*(1-3), 1–7. https://doi.org/10.1016/j.cplett.2006.04.117

Lin, H., Taniyasu, S., Yamazaki, E., Wei, S., Wang, X., Gai, N., Kim, J. H., Eun, H., Lam, P. K. S., & Yamashita, N. (2020). Per- and Polyfluoroalkyl Substances in the Air Particles of Asia: Levels, Seasonality, and Size-Dependent Distribution. *Environmental Science & Technology*, *54*(22), 14182–14191. https://doi.org/10.1021/acs.est.0c03387

Lovas, F. J., Lide, D. R., Suenram, R. D., & Johnson, D. R. (2012). Evolution of Microwave Spectroscopy at the National Bureau of Standards (NBS) and the National Institute of Standards and Technology (NIST). *Journal of Research of the National Institute of Standards and Technology*, *117*(0), 268. https://doi.org/10.6028/jres.117.016

Lv, Q.-Y., Wan, B., Guo, L.-H., Yang, Y., Ren, X.-M., & Zhang, H. (2015). In vivo immunotoxicity of perfluorooctane sulfonate in BALB/c mice: Identification of T-cell receptor and calcium-mediated signaling pathway disruption through gene expression profiling of the spleen. *Chemico-Biological Interactions*, *240*, 84–93. https://doi.org/10.1016/j.cbi.2015.07.015

McQuarrie, D. A. (n.d.). *Quantum Chemistry*. University Science Books. Retrieved from https://www.chemeurope.com/en/encyclopedia/Rigid_rotor.html#_note-Podolsky/

Mcquarrie, D. A. (2008). *Quantum chemistry*. University Science Books.

Mcquarrie, D. A., & Simon, J. D. (1997). *Physical chemistry : a molecular approach*. University Science Books, Cop.

Møller-Plesset_perturbation_theory. (n.d.). Www.chemeurope.com. Retrieved from https://www.chemeurope.com/en/encyclopedia/M%C3%B8ller-Plesset_perturbation_theory.html

Our People | Gaussian.com. (n.d.). Gaussian.com. Retrieved from https://gaussian.com/people/

PFAS Contamination Lawsuit | Douglas and London. (n.d.). Douglas & London. Retrieved from https://www.douglasandlondon.com/toxic-exposure-attorney/pfoa-and-pfos-water-contamination

Rigid Rotations. (n.d.). Retrieved from https://ocw.mit.edu/courses/chemistry/5-61-physical-chemistry-fall-2007/lecture-notes/lecture17.pdf

Schrodinger equation. (2019). Gsu.edu. http://hyperphysics.phy-astr.gsu.edu/hbase/quantum/schr.html

Schrodinger equation in three dimensions. (n.d.). Hyperphysics.phy-Astr.gsu.edu. Retrieved from http://hyperphysics.phy-astr.gsu.edu/hbase/quantum/sch3D.html

Sherrill, C. (n.d.). *Introduction to Density Functional Theory*. Retrieved December 30, 2019, from http://vergil.chemistry.gatech.edu/notes/DFT-intro.pdf

Sherrill, D. (2006, August 15). *The Rigid Rotor*. Vergil.chemistry.gatech.edu.
http://vergil.chemistry.gatech.edu/notes/quantrev/node24.html

Snyder, L. E., Buhl, D., Zuckerman, B., & Palmer, P. (1969). Microwave Detection of
Interstellar Formaldehyde. *Physical Review Letters*, *22*(13), 679–681.
https://doi.org/10.1103/physrevlett.22.679

Spherical and Spheroidal Harmonics. (n.d.). Dlmf.nist.gov. Retrieved from
https://dlmf.nist.gov/14.30

Stone, N. J. (2005). Table of nuclear magnetic dipole and electric quadrupole moments. *Atomic
Data and Nuclear Data Tables*, *90*(1), 75–176. https://doi.org/10.1016/j.adt.2005.04.001

Strong, B. (2013, October 2). *Rotational Spectroscopy of Diatomic Molecules*. Chemistry
LibreTexts.
https://chem.libretexts.org/Bookshelves/Physical_and_Theoretical_Chemistry_Textbook
_Maps/Supplemental_Modules_(Physical_and_Theoretical_Chemistry)/Spectroscopy/Ro
tational_Spectroscopy/Rotational_Spectroscopy_of_Diatomic_Molecules

Suja, F., Pramanik, B. K., & Zain, S. Md. (2009). Contamination, bioaccumulation, and toxic
effects of perfluorinated chemicals (PFCs) in the water environment: a review paper.
Water Science and Technology, *60*(6), 1533–1544. https://doi.org/10.2166/wst.2009.504

Supersonic Expansion | Ken Leopold Research Group. (n.d.). Kleopold.chem.umn.edu.
Retrieved from http://kleopold.chem.umn.edu/instrumentation/supersonic-expansion

TANG, S.-Y., XIA, Z.-N., FU, Y.-J., & GOU, Q. (2008). Advances and Applications of
Microwave Spectroscopy. *Chinese Journal of Analytical Chemistry*, *36*(8), 1145–1151.
https://doi.org/10.1016/s1872-2040(08)60061-4

The Mossbauer Effect Theory. (2021). Knox.edu.
http://faculty.knox.edu/cschulz/M%F6ssbauer/theory.htm

The POPs. (n.d.). Www.pops.int.
http://www.pops.int/TheConvention/ThePOPs/tabid/673/Default.aspx

*THE SCIENCE OF ORGANIC FLUOROCHEMISTRY 3M The Science of Organic
Fluorochemistry*. (1999).
https://www.ag.state.mn.us/Office/Cases/3M/docs/PTX/PTX1558.pdf

Watson, J. K. G. (2004). Rotational Spectroscopy of Diatomic Molecules Rotational
Spectroscopy of Diatomic Molecules , John M. Brown and Alan Carrington Cambridge
U. Press, New York, 2003. (1013 pp.). ISBN 0-521-81009-4, ISBN 0-521-53078-4 paper.
Physics Today, *57*(12), 68–69. https://doi.org/10.1063/1.1878342

Western, C. M. (2017). PGOPHER: A program for simulating rotational, vibrational, and electronic spectra. *Journal of Quantitative Spectroscopy and Radiative Transfer*, *186*, 221–242. https://doi.org/10.1016/j.jqsrt.2016.04.010

Wikipedia Contributors. (2019, April 7). *ENIAC*. Wikipedia; Wikimedia Foundation. https://en.wikipedia.org/wiki/ENIAC

Wong, B. M. (2008). Nuclear quadrupole hyperfine structure in HC14N/H14NC and DC15N/D15NC isomerization: a diagnostic tool for characterizing vibrational localization. *Physical Chemistry Chemical Physics*, *10*(36), 5599. https://doi.org/10.1039/b807672c

Zeng, Z., Song, B., Xiao, R., Zeng, G., Gong, J., Chen, M., Xu, P., Zhang, P., Shen, M., & Yi, H. (2019). Assessing the human health risks of perfluorooctane sulfonate by in vivo and in vitro studies. *Environment International*, *126*, 598–610. https://doi.org/10.1016/j.envint.2019.03.002

Zhao, Y. G., Wong, C. K. C., & Wong, M. H. (2012). Environmental contamination, human exposure, and body loadings of perfluorooctane sulfonate (PFOS), focusing on Asian countries. *Chemosphere*, *89*(4), 355–368. https://doi.org/10.1016/j.chemosphere.2012.05.043

Zhou, Z., Shi, Y., Li, W., Xu, L., & Cai, Y. (2012). Perfluorinated Compounds in Surface Water and Organisms from Baiyangdian Lake in North China: Source Profiles, Bioaccumulation and Potential Risk. *Bulletin of Environmental Contamination and Toxicology*, *89*(3), 519–524. https://doi.org/10.1007/s00128-012-0745-1

APPENDIX

APPENDIX

REFERENCES IN THE ORDER THEY WERE USED

Chapter 1: References

1. Lin, H., Taniyasu, S., Yamazaki, E., Wei, S., Wang, X., Gai, N., Kim, J. H., Eun, H., Lam, P. K. S., & Yamashita, N. (2020). Per- and Polyfluoroalkyl Substances in the Air Particles of Asia: Levels, Seasonality, and Size-Dependent Distribution. *Environmental Science & Technology*, *54*(22), 14182–14191. https://doi.org/10.1021/acs.est.0c03387

2. *PFAS Contamination Lawsuit | Douglas and London*. (n.d.). Douglas & London. Retrieved from https://www.douglasandlondon.com/toxic-exposure-attorney/pfoa-and-pfos-water-contamination

3. Suja, F., Pramanik, B. K., & Zain, S. Md. (2009). Contamination, bioaccumulation, and toxic effects of perfluorinated chemicals (PFCs) in the water environment: a review paper. *Water Science and Technology*, *60*(6), 1533–1544. https://doi.org/10.2166/wst.2009.504

4. Lv, Q.-Y., Wan, B., Guo, L.-H., Yang, Y., Ren, X.-M., & Zhang, H. (2015). In vivo immunotoxicity of perfluorooctane sulfonate in BALB/c mice: Identification of T-cell receptor and calcium-mediated signaling pathway disruption through gene expression profiling of the spleen. *Chemico-Biological Interactions*, *240*, 84–93. https://doi.org/10.1016/j.cbi.2015.07.015

5. Zhao, Y. G., Wong, C. K. C., & Wong, M. H. (2012). Environmental contamination, human exposure, and body loadings of perfluorooctane sulfonate (PFOS), focusing on Asian countries. *Chemosphere*, *89*(4), 355–368. https://doi.org/10.1016/j.chemosphere.2012.05.043

6. *THE SCIENCE OF ORGANIC FLUOROCHEMISTRY. 3M. The Science of Organic Fluorochemistry*. (1999). https://www.ag.state.mn.us/Office/Cases/3M/docs/PTX/PTX1558.pdf

7. *A Perfluoroalkyl and Polyfluoroalkyl Substances (PFAS) in the U.S. Population*. (n.d.). https://www.atsdr.cdc.gov/pfas/docs/PFAS_in_People.pdf

8. *The POPs*. (n.d.). Www.pops.int. http://www.pops.int/TheConvention/ThePOPs/tabid/673/Default.aspx

9. Lehmler, H.-J. (2005). Synthesis of environmentally relevant fluorinated surfactants—a review. *Chemosphere*, *58*(11), 1471–1496. https://doi.org/10.1016/j.chemosphere.2004.11.078

10. Hauptschein, M., & Braid, M. (1961). Fluorocarbon Halosulfates and a New Route to Fluorocarbon Acids and Derivatives. I. Polyfluoroalkyl Chlorosulfates1. *Journal of the American Chemical Society*, *83*(11), 2500–2505. https://doi.org/10.1021/ja01472a01

11. Jian, J.-M., Chen, D., Han, F.-J., Guo, Y., Zeng, L., Lu, X., & Wang, F. (2018). A short review on human exposure to and tissue distribution of per- and polyfluoroalkyl substances (PFASs). *Science of the Total Environment*, *636*, 1058–1069. https://doi.org/10.1016/j.scitotenv.2018.04.380

12. Ghisi, R., Vamerali, T., & Manzetti, S. (2019). Accumulation of perfluorinated alkyl substances (PFAS) in agricultural plants: A review. *Environmental Research*, *169*, 326–341. https://doi.org/10.1016/j.envres.2018.10.023

13. Zhou, Z., Shi, Y., Li, W., Xu, L., & Cai, Y. (2012). Perfluorinated Compounds in Surface Water and Organisms from Baiyangdian Lake in North China: Source Profiles, Bioaccumulation and Potential Risk. *Bulletin of Environmental Contamination and Toxicology*, *89*(3), 519–524. https://doi.org/10.1007/s00128-012-0745-1

14. Zeng, Z., Song, B., Xiao, R., Zeng, G., Gong, J., Chen, M., Xu, P., Zhang, P., Shen, M., & Yi, H. (2019). Assessing the human health risks of perfluorooctane sulfonate by in vivo and in vitro studies. *Environment International*, *126*, 598–610. https://doi.org/10.1016/j.envint.2019.03.002

15. Li, S., Tao, F.-M., & Gu, R. (2006). Theoretical study on the ionic dissociation of halosulfonic acids in small water clusters. *Chemical Physics Letters*, *426*(1-3), 1–7. https://doi.org/10.1016/j.cplett.2006.04.117

16. Kao, P. N., & Turner, P. H. (1979). Conformational study of cyclohexanecarboxaldehyde by microwave spectroscopy. *Journal of the American Chemical Society*, *101*(16), 4497–4499. https://doi.org/10.1021/ja00510a011

17. Badawi, H. M. (1996). An ab initio study of internal rotation in cyclohexanecarboxaldehyde and cyclohexanecarboxylic acid fluoride and chloride. *Journal of Molecular Structure: THEOCHEM*, *369*(1-3), 75–83. https://doi.org/10.1016/s0166-1280(96)04642-8

Chapter 2 References:

1. *ENIAC - CHM Revolution*. (2019). Computerhistory.org. https://www.computerhistory.org/revolution/birth-of-the-computer/4/78

2. *Evolving the Early Universe in 24 Hours on Frontera - Latest News - Texas Advanced Computing Center*. (n.d.). Www.tacc.utexas.edu. Retrieved November 11, 2021, from https://www.tacc.utexas.edu/-/evolving-the-early-universe-in-24-hours-on-frontera

3. Dubrow, A. (2021, January 25). *Simulating 800,000 Years of California Earthquake History to Pinpoint Risks - Latest News - Texas Advanced Computing Center*. Www.tacc.utexas.edu. https://www.tacc.utexas.edu/-/simulating-800-000-years-of-california-earthquake-history-to-pinpoint-risks

4. *Our People | Gaussian.com*. (n.d.). Gaussian.com. Retrieved November 11, 2021, from https://gaussian.com/people/

5. PGOPHER, A Program for Simulating Rotational, Vibrational and Electronic Spectra, C. M. Western, *Journal of Quantitative Spectroscopy and Radiative Transfer*, 186 221-242 (2017) doi:10.1016/j.jqsrt.2016.04.010. The accepted manuscript is also available.

6. *Schrodinger equation*. (2019). Gsu.edu. http://hyperphysics.phy-astr.gsu.edu/hbase/quantum/schr.html

7. David, C., & Sherrill. (2000). *An Introduction to Hartree-Fock Molecular Orbital Theory*. http://vergil.chemistry.gatech.edu/courses/chem6485/pdf/hf-intro.pdf

8. Hanson, D., Harvey, E., Sweeny, R., & Zielinski, T. (2013, October 3). *9.7: The Self-Consistent Field Approximation (Hartree-Fock Method)*. Chemistry LibreTexts. https://chem.libretexts.org/Bookshelves/Physical_and_Theoretical_Chemistry_Textbook_Maps/Book%3A_Quantum_States_of_Atoms_and_Molecules_(Zielinksi_et_al)/09%3A_The_Electronic_States_of_the_Multielectron_Atoms/9.07%3A_The_Self-Consistent_Field_Approximation_(Hartree-Fock_Method)

9. Attila Szabo, & Ostlund, N. S. (1996). *Modern quantum chemistry : introduction to advanced electronic structure theory* (pp. 53, 54). Dover Publications.

10. Amusia, M. Y., Msezane, A. Z., & Shaginyan, V. R. (2003). Density Functional Theory versus the Hartree–Fock Method: Comparative Assessment. *Physica Scripta*, *68*(6), C133–C140. https://doi.org/10.1238/physica.regular.068ac0133

11. Sherrill, C. (n.d.). *Introduction to Density Functional Theory*. Retrieved December 30, 2019, from http://vergil.chemistry.gatech.edu/notes/DFT-intro.pdf

12. Clark, S. (2003, May 4). *The Hohenberg-Kohn Theorems*. Cmt.dur.ac.uk. http://cmt.dur.ac.uk/sjc/thesis_ppr/node12.html

13. *Density Functional Theory for Beginners*. (2019). Ex.ac.uk. http://newton.ex.ac.uk/research/qsystems/people/coomer/dft_intro.html

14. *Møller-Plesset perturbation theory*. (n.d.). Www.chemeurope.com. Retrieved from https://www.chemeurope.com/en/encyclopedia/M%C3%B8ller-Plesset_perturbation_theory.html

15. Foresman, J. B. (1996). *Exploring chemistry with electronic structure methods. Foresman, Æleen Frisch* (pp. 267–268). Gaussian.

16. Foresman, J. B. (1996). *Exploring chemistry with electronic structure methods. Foresman, Æleen Frisch* (pp. 261–262). Gaussian.

17. Hanson, D., Harvey, E., Sweeney, R., & Zielinski, T. (2020, March 18). *11.2: Gaussian Basis Sets*. Chemistry LibreTexts. https://chem.libretexts.org/Courses/Pacific_Union_College/Quantum_Chemistry/11:_Computational_Quantum_Chemistry/11.02:_Gaussian_Basis_Sets

18. Dunning, T. H. (1989). Gaussian basis sets for use in correlated molecular calculations. I. The atoms boron through neon and hydrogen. *The Journal of Chemical Physics*, *90*(2), 1007–1023. https://doi.org/10.1063/1.456153

19. Basis Sets in Computational Chemistry. (2021). In E. Perlt (Ed.), *Lecture Notes in Chemistry*. Springer International Publishing. https://doi.org/10.1007/978-3-030-67262-1

Chapter 3: References

1. Gordy, W. (1983). Early events and some later developments in microwave spectroscopy. *Journal of Molecular Structure*, *97*, 17–32. https://doi.org/10.1016/0022-2860(83)90172-2

2. Forman, P., & Smithsonian Institution Washington Dc. (1985). *The First Atomic Clock Program: NBS, 1947-1954.* Ft. Belvoir Defense Technical Information Center 03 Dec.

3. *Basic Radio Propagation Predictions FOR SEPTEMBER 1950 Three Months in Advance*. (1950). https://nvlpubs.nist.gov/nistpubs/Legacy/brpd-crpl-d/brpd-crpl-d70.pdf

4. Cafe, K. B. R. (2017, January 2). *The New Field of Microwave Spectroscopy, July 1949 Radio and Television News*. https://www.rfcafe.com/references/radio-news/new-field-microwave-spectroscopy-radio-television-news-july-1949.htm

5. Lovas, F. J., Lide, D. R., Suenram, R. D., & Johnson, D. R. (2012). Evolution of Microwave Spectroscopy at the National Bureau of Standards (NBS) and the National Institute of Standards and Technology (NIST). *Journal of Research of the National Institute of Standards and Technology*, *117*(0), 268. https://doi.org/10.6028/jres.117.016

6. Snyder, L. E., Buhl, D., Zuckerman, B., & Palmer, P. (1969). Microwave Detection of Interstellar Formaldehyde. *Physical Review Letters*, *22*(13), 679–681. https://doi.org/10.1103/physrevlett.22.679

7. Balle, T. J., & Flygare, W. H. (1981). Fabry–Perot cavity pulsed Fourier transform microwave spectrometer with a pulsed nozzle particle source. *Review of Scientific Instruments*, *52*(1), 33–45. https://doi.org/10.1063/1.1136443

8. Brown, G. G., Dian, B. C., Douglass, K. O., Geyer, S. M., & Pate, B. H. (2006). The rotational spectrum of epifluorohydrin measured by chirped-pulse Fourier transform microwave spectroscopy. *Journal of Molecular Spectroscopy*, *238*(2), 200–212. https://doi.org/10.1016/j.jms.2006.05.003

9. *BrightSpec: Product Portfolio*. (n.d.). BrightSpec. Retrieved November 11, 2021, from http://brightspec.com/products-academic/

10. TANG, S.-Y., XIA, Z.-N., FU, Y.-J., & GOU, Q. (2008). Advances and Applications of Microwave Spectroscopy. *Chinese Journal of Analytical Chemistry*, *36*(8), 1145–1151. https://doi.org/10.1016/s1872-2040(08)60061-4

11. 6416, C., & Evans, M. (n.d.). *Microwave Rotational Spectroscopy*. https://sci.tanta.edu.eg/files/microwave-rotational-spectroscopy-mce.pdf

12. Brown, G. G., Dian, B. C., Douglass, K. O., Geyer, S. M., Shipman, S. T., & Pate, B. H. (2008). A broadband Fourier transform microwave spectrometer based on chirped pulse excitation. *Review of Scientific Instruments*, *79*(5), 053103. https://doi.org/10.1063/1.2919120

13. Fradette, R. (2016). *Understanding Vacuum and Vacuum Measurement*. https://solarmfg.com/wp-content/uploads/2016/02/Understanding-Vacuum-9.pdf

14. *Supersonic Expansion | Ken Leopold Research Group*. (n.d.). Kleopold.chem.umn.edu. Retrieved November 11, 2021, from http://kleopold.chem.umn.edu/instrumentation/supersonic-expansion

15. Houghton, N. (2013, October 2). *Microwave Rotational Spectroscopy*. Chemistry LibreTexts. https://chem.libretexts.org/Bookshelves/Physical_and_Theoretical_Chemistry_Textbook _Maps/Supplemental_Modules_(Physical_and_Theoretical_Chemistry)/Spectroscopy/Ro tational_Spectroscopy/Microwave_Rotational_Spectroscopy#_ENREF_4

16. Koch, C. P., Lemeshko, M., & Sugny, D. (2019). Quantum control of molecular rotation. *Reviews of Modern Physics*, *91*(3). https://doi.org/10.1103/revmodphys.91.035005

17. Mcquarrie, D. A. (2008). *Quantum chemistry*. University Science Books.

18. Merzbacher, E. (1970) Quantum Mechanics. 2nd Edition, J. Wiley & Sons, New York.

19. Houghton, N. (2013b, October 2). *Microwave Rotational Spectroscopy*. Chemistry LibreTexts. https://chem.libretexts.org/Bookshelves/Physical_and_Theoretical_Chemistry_Textbook _Maps/Supplemental_Modules_(Physical_and_Theoretical_Chemistry)/Spectroscopy/Ro tational_Spectroscopy/Microwave_Rotational_Spectroscopy#_ENREF_4

20. John Michael Hollas, & Wiley, J. (2010). *Modern spectroscopy*. John Wiley & Sons Ltd.

21. Strong, B. (2013, October 2). *Rotational Spectroscopy of Diatomic Molecules*. Chemistry LibreTexts.
https://chem.libretexts.org/Bookshelves/Physical_and_Theoretical_Chemistry_Textbook_Maps/Supplemental_Modules_(Physical_and_Theoretical_Chemistry)/Spectroscopy/Rotational_Spectroscopy/Rotational_Spectroscopy_of_Diatomic_Molecules

22. *Computational Chemistry Comparison and Benchmark*. (n.d.). Cccbdb.nist.gov.
https://cccbdb.nist.gov/exp2x.asp?casno=630080&charge=0

23. Garland, C., Nibler, J., & Shoemaker, D. (n.d.). *Experiments in Physical Chemistry Eighth Edition*. https://dailydialectics.com/education/TEXTBOOKS/PChemLabTXT.pdf

24. *Computational Chemistry Comparison and Benchmark - Calculated Rotational Constants*. (n.d.). Cccbdb.nist.gov. Retrieved from https://cccbdb.nist.gov/rotcalc2x.asp

25. *Computational Chemistry Comparison and Benchmark - Calculated electric dipole page 3*. (n.d.). Cccbdb.nist.gov. Retrieved from
https://cccbdb.nist.gov/dipole3x.asp?method=3&basis=18

26. Watson, J. K. G. (2004). Rotational Spectroscopy of Diatomic Molecules Rotational Spectroscopy of Diatomic Molecules, John M. Brown and Alan Carrington Cambridge U. Press, New York, 2003. ISBN 0-521-81009-4, ISBN 0-521-53078-4 paper. *Physics Today*, *57*(12), 68–69. https://doi.org/10.1063/1.1878342

27. Stone, N. J. (2005). Table of nuclear magnetic dipole and electric quadrupole moments. *Atomic Data and Nuclear Data Tables*, *90*(1), 75–176.
https://doi.org/10.1016/j.adt.2005.04.001

28. Mcquarrie, D. A., & Simon, J. D. (1997). *Physical chemistry : a molecular approach*. University Science Books, Cop.

29. Garland, C. W., Nibler, J. W., & Shoemaker, D. P. (2009). *Experiments in physical chemistry*. Mcgraw-Hill Higher Education.

30. Cook, R. L. (2003). Microwave molecular spectroscopy. *Encyclopedia of Physical Science and Technology*, 799–852. https://doi.org/10.1016/b0-12-227410-5/00447-6

31. Drago, R. S. (1992). "*Quadrupole Moments Physical Methods for Chemists*". Ft. Worth: Saunders College Pub.

32. Wong, B. M. (2008). Nuclear quadrupole hyperfine structure in HC14N/H14NC and DC15N/D15NC isomerization: a diagnostic tool for characterizing vibrational localization. *Physical Chemistry Chemical Physics*, *10*(36), 5599.
https://doi.org/10.1039/b807672c

33. *The Mossbauer Effect Theory*. (2021). Knox.edu.
http://faculty.knox.edu/cschulz/M%F6ssbauer/theory.htm

34. McQuarrie, D. A. (n.d.). *Quantum Chemistry*. University Science Books. Retrieved from https://www.chemeurope.com/en/encyclopedia/Rigid_rotor.html#_note-Podolsky/

35. *Angular Momentum and Rigid-Rotor Models and*. (n.d.). Retrieved from
https://web2.aabu.edu.jo/tool/course_file/lec_notes/403741_Lecture%203%20Angular%20Momentum.pdf

36. *Schrodinger equation in three dimensions*. (n.d.). Hyperphysics.phy-Astr.gsu.edu. Retrieved from http://hyperphysics.phy-astr.gsu.edu/hbase/quantum/sch3D.html

37. Sherrill, D. (2006, August 15). *The Rigid Rotor*. Vergil.chemistry.gatech.edu.
http://vergil.chemistry.gatech.edu/notes/quantrev/node24.html

38. *Quantum rigid rotor Study Goal of This Lecture*. (n.d.).
https://quantum.ch.ntu.edu.tw/online_courses/PCIIQC2009/PDF/Lecture11.pdf

39. *Rigid Rotations*. (n.d.). Retrieved from https://ocw.mit.edu/courses/chemistry/5-61-physical-chemistry-fall-2007/lecture-notes/lecture17.pdf
40. *Spherical and Spheroidal Harmonics*. (n.d.). Dlmf.nist.gov. Retrieved November 11, 2021, from https://dlmf.nist.gov/14.30

Chapter 4: References

1. *Cyclohexane Conformational Analysis*. Research.cm.utexas.edu. http://research.cm.utexas.edu/nbauld/teach/cyclohex.html
2. Foresman, J. B. (1996b). *Exploring chemistry with electronic structure methods. Foresman, Æleen Frisch* (pp. 171–172). Gaussian.

Chapter 5: References

1. Huff, A. K., Love, N., & Leopold, K. R. (2021). Microwave Study of Triflic Acid Hydrates: Evidence for the Transition from Hydrogen-Bonded Clusters to a Microsolvated Ion Pair. *The Journal of Physical Chemistry A*, *125*(36), 8033–8046. https://doi.org/10.1021/acs.jpca.1c06815

BIOGRAPHICAL SKETCH

Diego Erik Rodriguez, born Brownsville, Texas, obtained his high school diploma from Veterans Memorial Early College High School in June 2016. He went on to obtain an American Chemical Society (ACS) certified Bachelor of Science degree in chemistry at Texas A&M – University of Kingsville (TAMUK) in December 2019. During his time as an undergraduate, Diego worked in Research Compliance and in the sustainability office at TAMUK. He also presented in two ACS symposiums in 2019 before graduating.

At 23 years old, Diego obtained his Master of Science in Chemistry in December 2021 at the University of Texas – Rio Grande Valley (UTRGV) thanks to the guidance of his graduate research advisor, Dr. Wei Lin. During his time as a master's student, Diego participated in several virtual symposium presenting the results of his research, collaborated with peers at the Missouri University of Science and Technology, and worked as a graduate teaching assistant teaching organic and general chemistry labs at UTRGV. To contact him personally, e-mail diegorodz35@yahoo.com.